Walther-Meissner-Institut

Physik Department
TU München

Bayerische Akademie
der Wissenschaften

Gradiometric flux quantum bits with tunable tunnel coupling

Diploma Thesis

Jan Goetz

November 2011

Supervisor: Prof. Dr. Rudolf Gross

Technische Universität München

Contents

Chapter 1
Introduction

Superconducting flux quantum bits (qubits) [1–6] are Josephson junction based circuits acting as quantum mechanical two-level systems [7] for potential solid state based quantum information processing (QIP) architectures [8]. From a conceptual point of view, the two levels of the flux qubit correspond to two minima of a double-well potential which are coupled via tunnelling processes [9]. The magnitude of the associated tunneling matrix element is, although essential with respect to quantum coherence [10–14], usually fixed by design and fabrication procedure. Following recent experimental effort [15–25], flux qubits with controllable tunnel coupling are expected to provide significant additional freedom in the design of QIP systems based on flux qubits, in particular with resepct to the important aspect of scalability.

Utilizing quantum mechanical systems allows to perform different types of quantum algorithms [26–30] to solve certain complex NP-complete problems in times scaling polynomial to the problem size [31, 36]. Together with quantum cryptography [32, 33] and quantum error correction [34, 35] QIP systems form a very active and promising field of research.
The experimental realization of qubit based systems requires certain criteria [37], most importantly sufficiently long coherence times and scalability. First experiences with qubits have been made in the early 1990's in atomic physics [38–41] and quantum optics [42, 43]. A different approach to use nuclear spin resonance had great success in 2001 when Shor's quantum algorithm was experimentally realized by factorizing the number fifteen [44, 45]. Other approaches use electron spin resonance [46], quantum dots [47] or cavity-QED [48, 49]. Moreover, there are three types of superconducting qubits depending on the well characterized quantum variable and the dominating energy of the system [50, 51]. Besides the phase qubit [52, 53] and the charge qubit, which is also known as Cooper pair box [54, 55], there is the flux qubit which was first realized in 2000 [56] and is the basis of this work.
Superconducting systems have potential to provide enormous advantage in terms of scalability and have a good ratio of feasible coupling strengths to quantum coherence [57–61]. A promising approach is to combine these advantages with systems that provide longer coherence times in terms of hybrid systems [25, 62–64].
Due to their discrete level structure, qubits can also be considered as artificial atoms [65,

66]. Using superconducting resonators as cavities for microwave photons and superconducting qubits as artificial atoms, opened the fascinating new field of circuit quantum electrodynamics (circuit-QED) [67, 68]. Following this approach, various experiments comparable to optical systems leading even beyond the well known physics in optics have been performed to study the interaction of a single confined or propagating photon and a two or three-level atom [24, 25, 57, 58, 63, 64, 69]. The fact that superconducting qubits could either play a major role in QIP systems or can be used as artificial atoms in circuit-QED, makes them a very interesting system to study in modern physics.

All these efforts based on qubits, in particular on flux qubits, could profit from tunable tunnel coupling providing further flexibility when designing circuit-QED architectures. To have control over the tunnel coupling in individual qubits is important to control qubit-qubit coupling on the one hand [76, 77, 80–84] and on the other hand to control coupling strengths in circuit QED [20, 22, 23, 85]. Moreover, controlling the tunnel coupling allows to exploit a new coupling scheme [84, 86], which can be used to demonstrate squeezed cooling [87] as well as simulation of Dirac equations as in trapped ions [88].

In this work a gradiometric qubit with tunable tunnel coupling is designed, fabricated and characterized. The tuning of the tunnel coupling Δ is achieved by replacing one of the three Josephson junctions by a dc-SQUID as suggested in the very first proposal on flux qubits [1]. In this thesis the tunable qubit is integrated into a gradiometric design, which has advantages concerning decoherence [89, 90] and controlability [91]. The qubit is fabricated using a commonly used single layer technology [92] to realize the sub-micron Josephson junctions. In this thesis tunability is successfully demonstrated and all relevant design parameters are characterized. As a side result, it is demonstrated that the production process at the WMI has reached a reasonable degree of reproducibility.

The rest of this thesis is organized as follows: Chapter 2 gives a short introduction to basic concepts of flux quantum systems. Chapter 3 contains all relevant experimental techniques used during this thesis as well as certain preliminary measurements.
In chapter 4 main experimental results obtained during this thesis are presented, which are microwave spectroscopy measurements on flux qubits. The characterization of standard three Josephson junction qubits in Sec. 4.1 was used to find adequate fabrication parameters. In Sec. 4.2 the successful implementation of two gradiometric qubits without tunable tunnel coupling is presented and crucial physical properties of these qubits are discussed. Section 4.3 shows the final result of this thesis which is the characterization of a successfully fabricated gradiometric qubit with tunable tunnel coupling. During these measurements the minimal transition frequency of the qubit was tuned from a negligible value into the GHz regime. Thus, the motivation of this thesis was successfully realized and a state of the art flux qubit has been provided at the WMI, which can be exploited in a variety of circuit-QED experiments.

2 Chapter
Superconducting flux quantum circuits

In this chapter a theoretical overview of superconducting flux quantum systems and their basic elements is given. The physics of a superconducting loop, which will be used as a *trap-loop*, is explained in Sec. 2.1 followed by the theory of Josephson junctions in Sec. 2.2, which are the main elements of superconducting flux quantum circuits. Integrating Josephson junctions into a superconducting loop can be used to build a SQUID used for readout, as well as a qubit (cf. Sec. 2.3 & 2.4).

2.1 Superconducting loops

To observe quantum mechanical behavior in electrical circuits, the thermal energy $E_{\mathrm{th}} = k_{\mathrm{B}}T$ must be sufficiently below the smallest energy difference of the system. This requires the temperature to be in the mK-regime to operate flux qubits with a minimal transition frequency of several GHz. This temperature is below the transition temperature of aluminum [93], which is used for all electrical circuits in this work. Therfore the circuits become superconducting, i.e. dissipationless, which is a second precondition to obeserve quantum mechanical phenomena [5].
Superconductivity can be described by a superconducting condensate, which is according to BCS-theory consisting of Cooper-pairs [94]. Cooper-pairs are formed by two electrons, which are bound in most cases by attractive electron-phonon interaction [95] causing bosonic properties of the condensate. This allows the description of the whole condensate by a single wavefunction [96]

$$\Psi(\mathbf{r},t) = \Psi_0(\mathbf{r},t) \cdot e^{i\theta(\mathbf{r},t)} = \sqrt{n_{\mathrm{s}}(\mathbf{r},t)} \cdot e^{i\theta(\mathbf{r},t)}. \tag{2.1.1}$$

Here $\theta(\mathbf{r},t)$ and $n_{\mathrm{s}}(\mathbf{r},t)$ are the space- and time-dependent macroscopic phase and the density of Cooper-pairs defining the superconducting condensate, respectively. A superconducting current can be described by the quantum mechanical current density $\mathbf{j}_{\mathrm{s}}$, which is expressed by [97]

$$\mathbf{j}_\mathrm{s}(\mathbf{r},t) = 2q_\mathrm{e}\cdot\Re\left\{\Psi^*(\mathbf{r},t)\left(-\frac{i\hbar}{2m_\mathrm{e}}\nabla - \frac{q_\mathrm{e}}{m_\mathrm{e}}\mathbf{A}(\mathbf{r},t)\right)\Psi(\mathbf{r},t)\right\}, \tag{2.1.2}$$

where m_e is the electron mass and $\mathbf{A}$ is the vector potential of a magnetic inductance $\mathbf{B} = \nabla\times\mathbf{A}$. Using the wavefunction of (2.1.1), the current density can be written as

$$\mathbf{j}_\mathrm{s}(\mathbf{r},t) = \frac{q_\mathrm{e}n_\mathrm{s}\hbar}{m_\mathrm{e}}\underbrace{\left\{\nabla\theta(\mathbf{r},t) - \frac{2q_\mathrm{e}}{\hbar}\mathbf{A}(\mathbf{r},t)\right\}}_{\gamma}, \tag{2.1.3}$$

where γ is the so called *gauge invariant phase difference.*

Fluxoid quantization in a closed superconducting loop

Fluxoid quantization is one of the most fundamental physical concepts in this work, which mainly determines the behavior of superconducting loops as well as SQUIDs and qubits under the influence of an external magnetic field [98]. The quantization of magnetic flux Φ in a closed superconducting ring was already proposed in 1950 by F. London [99] and experimentally proven in 1961 concurrently by Doll and Näbauer at the Walther-Meissner-Institut in Herrsching and Deaver and Fairbank at Stanford University [100, 101].
In a closed superconducting loop as shown in Fig. 2.1a the phase $\theta(\mathbf{r},t)$ needs to be continuous and single-valued around a certain integration path Γ, constraining it to integer multiples n of 2π [102]:

$$\oint_\Gamma \nabla\theta(\mathbf{r},t)\cdot\mathrm{d}s = 2\pi\cdot n, \quad n\in\mathbb{Z}\,. \tag{2.1.4}$$

Solving (2.1.3) for $\nabla\theta$ and using Stoke‘s theorem, (2.1.4) can be rewritten to express fluxoid quantization as

$$\boxed{\underbrace{\oint_\Gamma(\Lambda_\mathrm{L}\mathbf{j}_\mathrm{s}(\mathbf{r},t))\cdot\mathrm{d}s + \Phi}_{\text{fluxoid}} = n\cdot\Phi_0\,.} \tag{2.1.5}$$

Here $\Lambda_\mathrm{L} = (m_\mathrm{e}/n_\mathrm{s}q_\mathrm{e}^2) = \mu_0\lambda_\mathrm{L}^2$ is the London coefficient with the London penetration depth λ_L and $\Phi_0 = (h/2q_\mathrm{e}) \approx 2\cdot 10^{-15}\,\mathrm{Vs}$ is the fundamental flux quantum.
Equation (2.1.5) means that there always resides an integer amount of n flux quanta in a closed superconducting loop, which is guaranteed by a persistent supercurrent $I_\mathrm{circ} = \iint_{A_\mathrm{w}}\mathbf{j}_\mathrm{s}(\mathbf{r},t)\cdot\mathrm{d}A$ circulating around the loop. If the dimensions of the cross section A_w of the superconductor are larger than the London penetration depth, one can always find an integration path in (2.1.5) deep inside the superconductor where the current density is zero [103]. In this case the whole fluxoid will be generated by magnetic flux, which results in the limit of pure flux quantization.
For aluminum layers used in this work, the London penetration depth is of the order of some hundred nanometers [104], so that the dimensions of the nm-sized aluminum layers can be considered small compared to λ_L. In this case the quantized value is the so called *fluxoid*, which is composed of two parts: On the one hand there is magnetic flux $\Phi_\mathrm{ind} =$

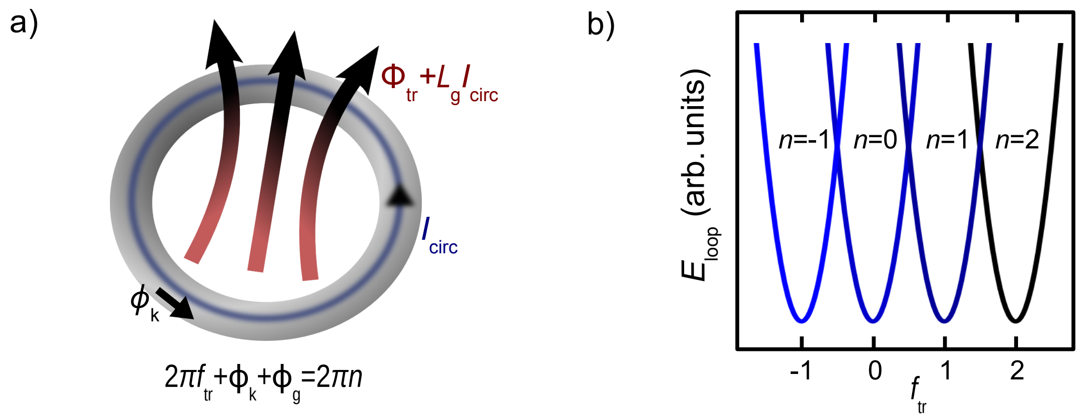

Figure 2.1 – **a)** Concept of a superconducting loop: The phase θ around the loop must be single-valued constraining it to integer multiples of 2π. The phase is composed of three parts: an external magnetic frustration $f_{\mathrm{tr}} = \Phi_{\mathrm{tr}}/\Phi_0$, a phase ϕ_{g} corresponding to the self induced field $\Phi_{\mathrm{ind}} = L_{\mathrm{g}} I_{\mathrm{circ}}$ of the circulating current and a phase ϕ_{k} due to the kinetic energy of the superconducting condensate in the loop; **b)** Parabolic energy dependence of a superconducting loop for different values n, belonging to the number of trapped fluxoid quanta.

$L_{\mathrm{g}} I_{\mathrm{circ}}$ corresponding to a phase difference $\phi_{\mathrm{g}} = 2\pi\Phi_{\mathrm{ind}}/\Phi_0$ around the loop with geometric inductance L_{g}. The second contribution to the fluxoid is a phase difference $\phi_{\mathrm{k}} = \oint_\Gamma \Lambda_{\mathrm{L}} I_{\mathrm{circ}} \cdot \mathrm{d}s$, arising from a kinetic inductance [105]

$$L_{\mathrm{k}} = \Lambda_{\mathrm{L}} \frac{s_{\mathrm{l}}}{A_{\mathrm{w}}}, \tag{2.1.6}$$

corresponding to the kinetic energy of the condensate. Here s_{l} is the total loop length. For arbitrary external magnetic fields, generating a loop frustration $f_{\mathrm{tr}} = \Phi_{\mathrm{tr}}/\Phi_0$, fluxoid quantization can be expressed by

$$\boxed{2\pi \overbrace{\frac{\Phi_{\mathrm{tr}}}{\Phi_0}}^{f_{\mathrm{tr}}} + \overbrace{2\pi \frac{L_{\mathrm{k}} I_{\mathrm{circ}}}{\Phi_0}}^{\phi_{\mathrm{k}}} + \overbrace{2\pi \frac{L_{\mathrm{g}} I_{\mathrm{circ}}}{\Phi_0}}^{\phi_{\mathrm{g}}} = 2\pi \cdot n\,.} \tag{2.1.7}$$

The reliable operation of gradiometric flux qubits with tunable tunnel coupling requires the knowledge on how much of the fluxoids are generated by the kinetic part ϕ_{k} and how much by the geometric part ϕ_{g}, described in detail in Sec. 3.3.

Energy of a superconducting loop

The energy of a superconducting loop has a parabolic flux dependence expressed by [106]

$$E_{\mathrm{loop}} = \frac{1}{2}(L_{\mathrm{g}} + L_{\mathrm{k}}) I_{\mathrm{circ}}^2 = \frac{\Phi_0^2}{2(L_{\mathrm{k}} + L_{\mathrm{g}})} (f_{\mathrm{tr}} - n)^2, \tag{2.1.8}$$

which is shown in Fig. 2.1b. Applying an integer amount of j flux quanta to the ring ($f_{\mathrm{tr}} = j$) in the normal state and cooling it down to the superconducting state, the ring

will prefer to stay in the lowest energy state ($n = j$). When the external flux is removed in the superconducting state, the ground state ($n = 0$) cannot be reached and the ring remains frozen in the $n = j$ state. During the transition into the superconducting state it is sufficient if the frustration is only approximately j ($|n - j| < 0.5$), since the circulating current compensates the flux to the next integer amount.
The number of trapped flux quanta can only change due to phase slip processes, requiring the order parameter $\theta(\mathbf{r},t)$ to go to zero in a region of the order of the coherence length [106]. Phase slips can for example happen via tunneling, noise or by thermal activation. The energy required for a phase slip is approximately given by [107–109]

$$E_{\Delta\mathrm{n}} \approx \sqrt{6} I_{\mathrm{c,wire}} \frac{\Phi_0}{2\pi}, \tag{2.1.9}$$

where $I_{\mathrm{c,wire}}$ is the critical current of the wire. Assuming the critical current to be of the order of 1 mA, the energy required for a phase slip corresponds to a temperature $T_{\mathrm{slip}} > 10\,000\,\mathrm{K}$ which means that phase slipping processes are very unlikely.

2.2 The Josephson junction

The Josephson effect, which describes the coherent tunneling of Cooper-pairs through an insulating barrier, has been predicted by Brian D. Josephson in 1962 and was honored with the Nobel Prize in 1973 [110–112]. Generally, a Josephson junction is a weak link between two superconducting electrodes, which can for example be realized by a layer of several Å thick aluminum oxide between two aluminum thin films [113, 114], as it is realized in this work (cf. Fig. 2.2a,b).
If the oxide layer is thin enough, the wavefunctions Ψ_1 and Ψ_2 of the two superconducting electrodes will overlap and Cooper-pairs can tunnel through the barrier [115]. A junction with area A_{J} can carry a tunnel current $I = jA_{\mathrm{J}}$, which is limited by a critical current density j_{c}. This critical current density depends exponentially on the barrier height and thickness [116] and defines the critical current I_{c} of a Josephson junction.
Starting to increase I while the junction is in the zero-voltage state, i.e. there is no voltage drop over the junction, and reaching the critical current I_{c}, the junction switches to the voltage

$$V_{\mathrm{g}} = \frac{2\Delta_0}{q_{\mathrm{e}}}, \tag{2.2.1}$$

which is approximately 365 μV for aluminum [117] (cf. Fig 2.2c). Here $2\Delta_0$ is the energy gap given by BCS theory [102]. For $I > I_{\mathrm{c}}$ the junction is in the voltage state, which means it has a fintie resistance R_{n}. Starting in this voltage state and decreasing the current, underdamped junction as used in this work show a hysteretic behavior so that the voltage drops back to zero at a current value $I_{\mathrm{re}} < I_{\mathrm{c}}$ [118, 119]. That makes the Josephson junction a highly non-linear element with a current-voltage characteristics shown in Fig. 2.2c.
A theory by Ambegaokar and Baratoff gives the maximum supercurrent through the junction as [120]

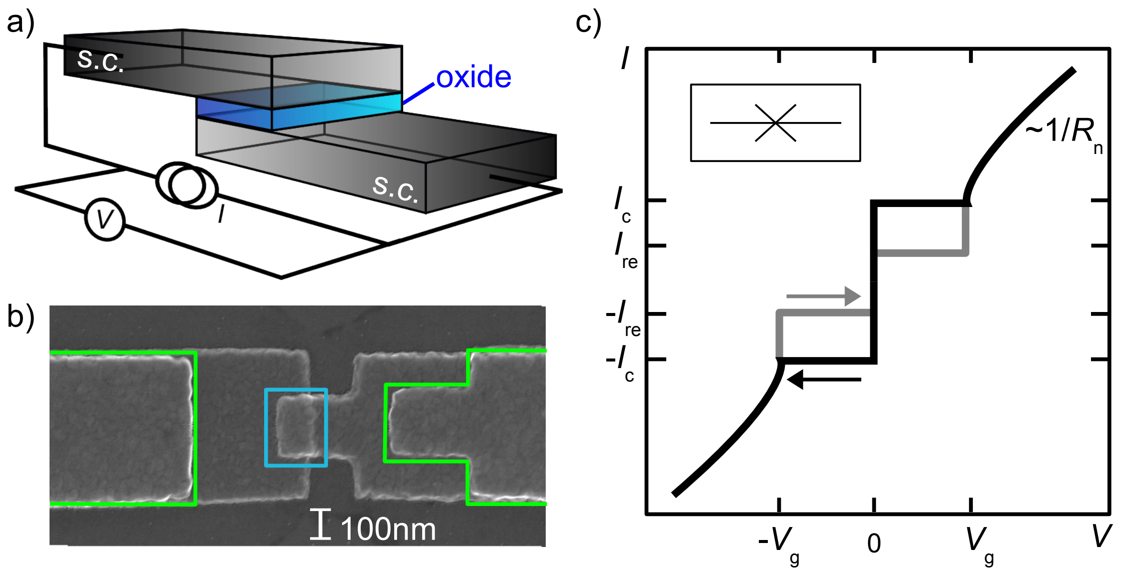

Figure 2.2 – **a)** Schematics of a Josephson junction which is in this work realized as two superconducting aluminum layers (gray) separated by a sub-nm thick oxide layer (blue). The junction can be biased at a current I to detect the voltage drop V across the junction; **b)** **S**canning **E**lectron **M**icroscope (SEM) image of a typical Josephson junction used in this work. The actual junction area is marked in blue, the green marked structures are due to the two angled shadow evaporation; **c)** Current-voltage characteristics of a Josephson junction. Up to a critical current I_c Cooper-pairs can tunnel through the junction. Reaching I_c the voltage switches to the value V_g. Underdamped junctions as used in this work typically show hysteretic behavior, i.e. the retrapping current I_{re} is smaller than the critical current I_c. Inset: In electrical circuits a Josephson junction can be represented as a cross.

$$I_c^{AB} = \frac{\pi\Delta_0}{2q_e R_n}. \tag{2.2.2}$$

Typical Josephson junctions used in this work have critical currents of approximately $1\,\mu$A which corresponds to a current density of about $2\,\mathrm{kA/cm^2}$.

The Josephson equations

Non-linearity is a major prerequisite for qubits and is given by the non-linear phase dependency of the critical current through a Josephson junction. The first Josephson equation describes the relation between the phase difference ϕ_J across the junction and the supercurrent

$$\boxed{j_s = j_c \sin(\phi_J)\,.} \tag{2.2.3}$$

In the second Josephson equation the time dependent phase evolution is expressed as

$$\boxed{\frac{\partial\phi_J}{\partial t} = \frac{2\pi}{\Phi_0}\cdot V.} \tag{2.2.4}$$

Taking the time derivative of the first Josephson equation shows that the junction can also be described as a highly non-linear inductance

$$L_{\mathrm{J}} = \frac{\Phi_0}{2\pi I_{\mathrm{c}} \cos\phi_{\mathrm{J}}} = L_{\mathrm{c}} \frac{1}{\cos\phi_{\mathrm{J}}}, \tag{2.2.5}$$

which is of the order of several nH for typical junctions in this work. The cosine term in the denominator allows the inductance to take negative values, which results in non-linear effects such as Eck-peaks or Fiske- and Shapiro steps [121–123].

The Josephson coupling energy E_{J} and the charging energy E_{c}

The Josephson coupling energy E_{J} and the charging energy E_{c} are characteristic energies for Josephson junctions and their ratio $E_{\mathrm{J}}/E_{\mathrm{c}}$ has to be in the range 10-100 for flux qubits to work properly.
Even though in the superconducting state there is no voltage drop and therefore no energy dissipation, a finite energy is stored in the junction which is the so called coupling energy E_{J}. This energy is analog to the binding energy in molecules where the wavefunction of different electrons overlap. In Josephson junctions the wavefunctions of the superconducting condensates overlap, so that coupling energy

$$E_{\mathrm{J}} = \int_t VI \cdot \mathrm{d}t = \int_t \frac{\Phi_0}{2\pi} \frac{\mathrm{d}\phi_{\mathrm{J}}}{\mathrm{d}t} I_{\mathrm{c}} \sin\phi_{\mathrm{J}} \cdot \mathrm{d}t = \frac{\Phi_0 I_c}{2\pi} \int_0^{\phi_{\mathrm{J}}(t)} \sin\varphi \cdot \mathrm{d}\varphi. \tag{2.2.6}$$

can be calculated by integrating the power $P = VI$ over time. This gives the energy stored in the junction

$$\boxed{E_{\mathrm{J}} = \frac{\Phi_0 I_{\mathrm{c}}}{2\pi}(1 - \cos\phi_{\mathrm{J}}) = E_{\mathrm{J0}}(1 - \cos\phi_{\mathrm{J}}).} \tag{2.2.7}$$

The fact that E_{J0} is proportional to I_{c} is utilized in this thesis to adjust the Josephson energy by changing the junction area. Typical junctions in this work have an area of approximately $0.03\,\mu\mathrm{m}^2$, which corresponds to an E_{J0} of approximately $350\,\mathrm{GHz} \cdot h$.
If a voltage is applied to the junction, the electric-field energy E_{field} is given by

$$E_{\mathrm{field}} = \frac{1}{2}CV^2 = \frac{Q^2}{2C} = \frac{(2Nq_{\mathrm{e}})^2}{2C} = 4E_{\mathrm{c}}N^2 \quad N \in \mathbb{N}, \tag{2.2.8}$$

where

$$\boxed{E_{\mathrm{c}} = \frac{q_{\mathrm{e}}^2}{2C}} \tag{2.2.9}$$

is the charging energy. Here C is the junction capacity and N is the number of Cooper-pairs stored on the junction.

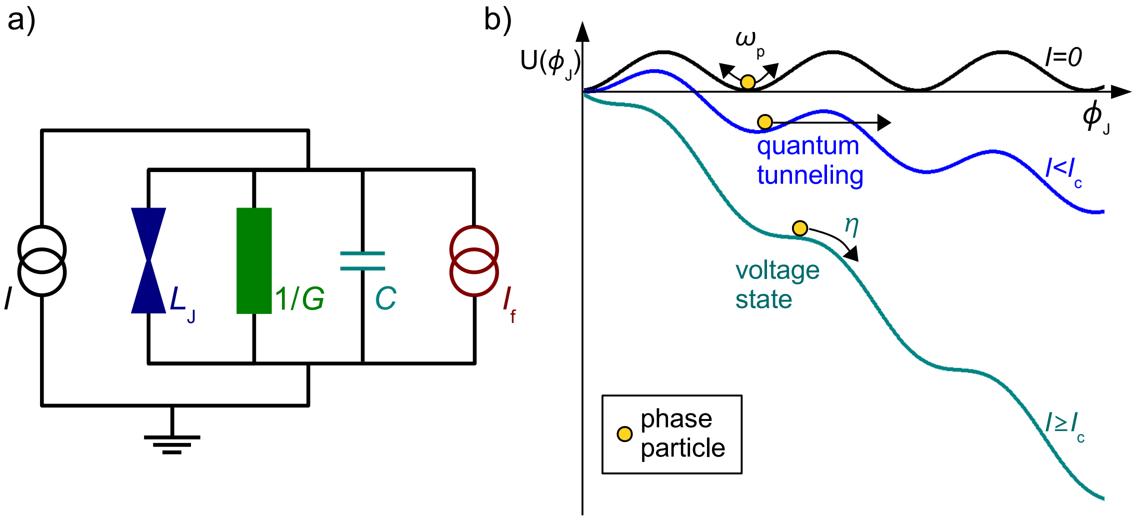

Figure 2.3 – **a)** Equivalent circuit for the RCSJ-model. A Josephson junction can be characterized by the inductance $L_\mathrm{J} = L_\mathrm{c}/\cos\phi_\mathrm{J}$, a voltage independent resistive channel ($1/G$), the junction capacitance C and a noise source I_f; **b)** Tilted washboard potential $U(\phi_\mathrm{J})$ for $I = 0$, $I < I_\mathrm{c}$ and $I \geq I_\mathrm{c}$. For $I = 0$ (black curve) the phase particle oscillates with the plasma frequency $\omega_\mathrm{p} = \frac{2\pi I_\mathrm{c}}{\Phi_0 C}$ in a local minimum. For $I < I_\mathrm{c}$ (blue curve) the particle can tunnel through the lowered potential barrier and for $I > I_\mathrm{c}$ (green curve) the phase particle moves continuously down the potential only damped by $\eta \propto 1/R$. In this case the junction is according to the second Josephson junction in the voltage state.

The RCSJ-model

The ***R**esistively and **C**apacitively **S**hunted **J**unction*-model (RCSJ-model), which was initially proposed by Stewart and McCumber in 1968 [124, 125], is a possibility to represent the junction by an electrotechnical equivalent circuit. The Josephson junction, which is biased by a current I, is modeled as a parallel circuit of a non-linear inductance L_J, a normal resistance $R_\mathrm{n} = 1/G$, a junction capacity C, and a noise source I_f as shown in Fig. 2.3a. Such a system can be described by a differential equation

$$\left(\frac{\hbar}{2q_\mathrm{e}}\right) C \frac{\mathrm{d}^2\phi_\mathrm{J}}{\mathrm{d}t^2} + \left(\frac{\hbar}{2q_\mathrm{e}}\right) G \frac{\mathrm{d}\phi_\mathrm{J}}{\mathrm{d}t} + I_\mathrm{c}\left[\sin\phi_\mathrm{J} - \frac{I}{I_\mathrm{c}} + \frac{I_\mathrm{f}(t)}{I_\mathrm{c}}\right] = 0, \tag{2.2.10}$$

which is analog to the description of a *phase particle* moving in a so called *tilted washboard potential* with damping $\eta = (\hbar/2q_\mathrm{e})^2\, G$. This particle with mass $m = (\hbar/2q_\mathrm{e})^2\, C$ represents the dynamics of the junction's phase ϕ_J, which is defined in the potential

$$U_\mathrm{pot}(\phi_\mathrm{J}) = \frac{\Phi_0 I_\mathrm{c}}{2\pi}\left(1 - \cos\phi_\mathrm{J} - \frac{I}{I_\mathrm{c}}\phi_\mathrm{J}\right). \tag{2.2.11}$$

In Fig. 2.3b the phase evolution is depicted for the three cases: $I = 0$, $I < I_\mathrm{c}$ and $I \geq I_\mathrm{c}$. The phase can either be changed by a current I tilting the potential, by a tunnel process through a lowered barrier or by a noise source I_f, which can be interpreted as someone "shaking" the washboard.

2.3 The dc-SQUID

A **S**uperconducting **QU**antum **I**nterference **D**evice (SQUID) is a very sensitive magnetometer [126] that can detect flux changes of up to $5\cdot 10^{-18}$ T [127, 128] and can therefore be used to read out superconducting flux qubits [129] as described in Sec. 3.2. In this thesis a SQUID is also used to tune the Josephson energy E_{J0} of a qubit junction, which allows to tune the minimal transition frequency of the qubit as described in Sec. 3.3.2.

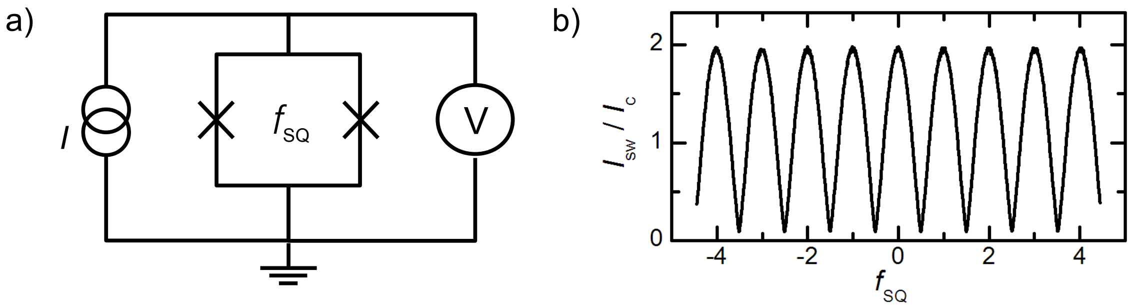

Figure 2.4 – **a)** Equivalent circuit of a dc-SQUID: Two Josephson junctions integrated in a superconducting loop which are biased by an external current I to detect the switching current I_{sw} as a function of magnetic frustration f_{SQ}; **b)** Magnetic field dependence of a SQUID's switching current. The SQUID frustration f_{SQ} is induced by a superconducting coil placed closely above the sample. In Sec. 3.3.2 this switching current dependence is used to tune the Josephson energy E_{J0} of a qubit junction.

The basic scheme of a dc-SQUID is depicted in Fig. 2.4a. The SQUID consists of a superconducting loop which is interrupted by two Josephson junctions with phase difference ϕ_1 and ϕ_2, respectively [130]. The junctions are assumed to be ideal and identical, which most notably means they have the same critical current I_{c}. As a SQUID is a parallel circuit of two Josephson junctions, its phase dynamics can also be described by a particle with mass $2m$ moving in the tilted washboard potential of (2.2.11).
For zero external flux applied, the junctions will switch to the voltage state at a certain current value $I_{\mathrm{sw}} = 2I_{\mathrm{c}}$ as shown in Fig. 2.4b. For non-zero frustration and a negligible loop inductance L, the switching current dependence

$$\boxed{I_{\mathrm{sw}}(f_{\mathrm{SQ}}) = 2I_{\mathrm{c}}\left|\cos\left(\pi\frac{\Phi_{\mathrm{SQ}}}{\Phi_0}\right)\right| = 2I_{\mathrm{c}}\left|\cos\left(\pi f_{\mathrm{SQ}}\right)\right|.} \tag{2.3.1}$$

can be derived from equations (2.2.3) and (2.1.7). This behavior can be understood as the superconducting analog to the well known double slit experiment in optics. In the double slit experiment two light beams interfere whereas in a SQUID the wavefunctions of two superconductors interfere.
Ideally, the $I_{\mathrm{sw}}(f_{\mathrm{SQ}})$-curve modulates down to zero when the SQUID frustration f_{SQ} equals $f_{\mathrm{SQ}} = 0.5 \mod \mathbb{Z}$. For these frustration values the circulating current I_{circ} has to compensate the maximum flux and reaches the critical current of the junctions. However, if the loop inductance is not negligible so that already small circulating currents $I_{\mathrm{circ}} \ll I_{\mathrm{sw}}$ compensate half a flux quantum, or if $I_{\mathrm{c}} > \Phi_0/2L$, the $I_{\mathrm{sw}}(\Phi_{\mathrm{SQ}})$-curve does not modulate down to zero anymore. This behavior is characterized by the so called *screening parameter*

$$\beta_{\mathrm{L}} = \frac{2LI_{\mathrm{c}}}{\Phi_0}, \tag{2.3.2}$$

which represents the ratio of magnetic flux that can be created by a I_{c} compared to half a flux quantum and should be less than one to avoid hysteretic behavior.
To detect small frustration changes δf_{SQ} as a change of I_{sw}, which are for example generated by a flux qubit, the SQUID can be chosen as a very sensitive detection tool.

2.4 The Josephson persistent-current qubit

In contrast to a classical bit which works either in the state 0 or I, a qubit can be in a superposition state

$$|\psi\rangle = a(t)\,|0\rangle + b(t)\,|\mathrm{I}\rangle\,, \qquad a,b \in \quad \mathbb{C} \tag{2.4.1}$$

with $|a(t)|^2 + |b(t)|^2 = 1$. For flux qubits the states $|0\rangle$ and $|\mathrm{I}\rangle$ correspond to a circulating current flowing clockwise and counterclockwise around a superconducting loop intersected by three Josephson junctions, respectively [2]. Two of the junctions have equal Josephson energies E_{J0} and the third junction has αE_{J0} with $0.5 < \alpha \leq 1$, which can be achieved by changing the junction size (cf. Fig. 2.5c). In the vicinity of $f_{\mathrm{q}} = 0.5$ the qubit is at its degeneracy point where the two lowest energy levels can be considered as a two-level system. This is analog to an spin ½-system and emphasizes the similarity between qubit and artificial atom.

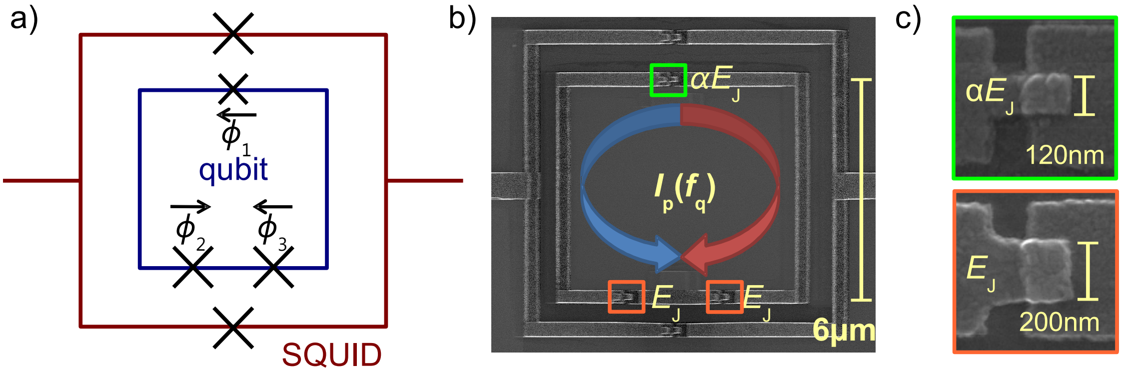

Figure 2.5 – **a)** Equivalent circuit of a qubit (blue) which is read out by a dc-SQUID (red): The qubit consists of a superconducting loop intersected by three Josephson junctions with phase difference ϕ_i; **b)** SEM image of a qubit and readout SQUID used in this work: The upper qubit Junction is smaller by a factor α. For a frustration $f_{\mathrm{q}} \neq 0$ persistent currents $\pm I_{\mathrm{p}}$ circulate around the qubit loop. These currents can be in a superposition state, which enables the quantum mechanical behavior of a qubit; **(c)** Two of the junctions have equal E_{J} and one has $\alpha \cdot E_{\mathrm{J}}$, which can be achieved by varying the junction size.

The qubit potential

For a negligible loop inductance the qubit potential can be written as the sum of the energies of three single Josephson junctions [131]:

$$U_{\mathrm{q}}(\phi_1,\phi_2,\phi_3) = E_{\mathrm{J0}}[(1-\cos\phi_1)+(1-\cos\phi_2)+\alpha(1-\cos\phi_3)], \qquad (2.4.2)$$

which can under the consideration of fluxoid quantization be reduced to

$$U_{\mathrm{q}}(\phi_1,\phi_2,f_{\mathrm{q}}) = E_{\mathrm{J0}}\left[2+\alpha-\cos\phi_1-\cos\phi_2-\alpha\cos\left(2\pi f_{\mathrm{q}}+\phi_1-\phi_2\right)\right]. \qquad (2.4.3)$$

For $\alpha > 0.5$ a cut in the potential of (2.4.3) along the line $\phi_2 = -\phi_1$ has the form of a double well which is symmetric for $f_{\mathrm{q}} = n+½$ (cf. Fig. 2.6a). The minima can be identified with the two stable states $|0\rangle$ and $|\mathrm{I}\rangle$ of the persistent current

$$I_{\mathrm{p}} = \pm I_{\mathrm{c}} \cdot \sqrt{1-\left(\frac{1}{2\alpha}\right)^2} \qquad (2.4.4)$$

flowing in opposite directions around the qubit loop. The barrier height between the two minima varies with α, being high for α close to one and vanishes for $\alpha = 0.5$.

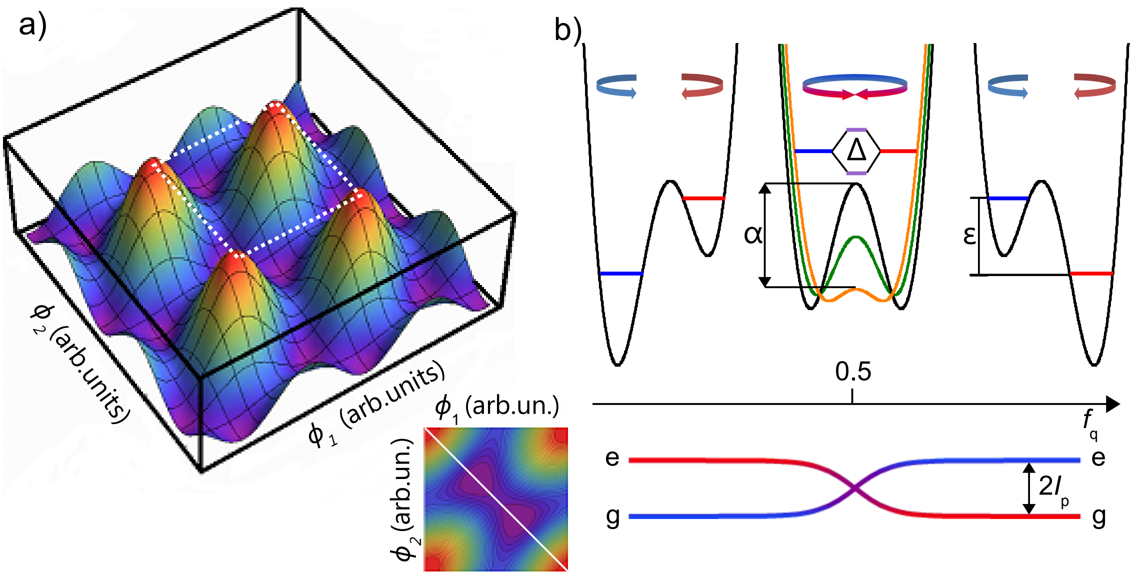

Figure 2.6 – **a)** Two dimensional qubit potential $U(\phi_1,\phi_2)$: The dashed rectangle connecting four maxima defines one unit cell, which is shown beneath as a top-view. A cut through that cell along the line $\phi_1 = -\phi_2$ yields a double well potential; **b) Top**: Double well potential for the three cases $f_{\mathrm{q}} < 0.5$, $f_{\mathrm{q}} = 0.5$ and $f_{\mathrm{q}} > 0.5$: If $f_{\mathrm{q}} = 0.5$ the qubit is in an equal superposition of the currents flowing in clockwise (red) and counterclockwise (blue) direction. In this case the ground and excited state are separated by the tunnel coupling Δ. This tunnel coupling varies with the potential height, which can be adapted by the value α. If $|f_{\mathrm{q}}-0.5| \gg 0$ the ground state corresponds to a current flowing in clock- or counterclockwise direction and can be excited with the energy ε. **Bottom**: Sketch of the expectation value of ground and excited state which is proportional to the expectation value of I_{p}.

The tunneling matrix element Δ

A finite tunneling probability Δ between the two states $|0\rangle$ and $|\mathrm{I}\rangle$ leads to formation of symmetric and antisymmetric superpositions according to (2.4.1). This tunneling probability depends exponentially on the barrier height and thus on α [132]:

$$\boxed{\Delta \propto \sqrt{E_{\mathrm{J0}}E_{\mathrm{c}}}\exp\left(-\alpha\sqrt{E_{\mathrm{J0}}/E_{\mathrm{c}}}\right).} \tag{2.4.5}$$

Equation (2.4.5) emphasizes the qubit's sensitivity to the parameters E_{J0} and E_{c} which are set up during fabrication. On the one hand a large E_{c} is required to increase the tunneling probability, but on the other hand the ratio $E_{\mathrm{J0}}/E_{\mathrm{c}}$ must be large enough to make the flux a well defined quantum variable. The main goal of this thesis is to build a flux qubit with tunable tunneling matrix element Δ which can be achieved by tuning the value α in situ.

Energy levels of a qubit

To obtain a full quantum mechanical description of a qubit, the transformation from the classical variables charge Q and phase ϕ into quantum mechanical operators has to be performed: $Q \to \hat{Q}_j = -i\hbar\partial/\partial\phi_j$ and $\phi \to \hat{\phi} = i\hbar\partial/\partial Q$, $j = 1{,}2$. Charge- and phase operator follow the commutation rule $[\hat{Q},\hat{\phi}] = -i\hbar$ [133] which leads to the uncertainty relation

$$\Delta\hat{Q}\Delta\hat{\phi} \geq \frac{\hbar}{2}. \tag{2.4.6}$$

Together with (2.4.3) the full Hamiltonian for a three junction qubit can be written as [18]

$$\mathcal{H}_{\mathrm{full}} = \frac{1}{2}\left(\frac{\hat{Q}_1^2}{2C} + \frac{\hat{Q}_2^2}{2C(1+2\alpha)}\right) + E_{\mathrm{J0}}\left[2+\alpha-\cos\hat{\phi}_1-\cos\hat{\phi}_2-\alpha\cos\left(2\pi f_{\mathrm{q}}+\hat{\phi}_1-\hat{\phi}_2\right)\right]. \tag{2.4.7}$$

At the degeneracy point the two lowest energy eigenstates corresponding to the ground state $|\mathrm{g}\rangle$ and the excited state $|\mathrm{e}\rangle$ can be used as the two qubit states (cf. Fig. 2.7). Higher energy states are separated by a large energy difference so that the system can be considered as a two-level system. Such a two-level system can be described by the Pauli spin matrices σ_i which emphasizes the similarity between the qubit and a spin ½-system, e.g. an artificial atom. The effective Hamiltonian $\mathcal{H}_{\mathrm{q}}$ is then given by [1]

$$\boxed{\mathcal{H}_{\mathrm{q}} = \frac{\varepsilon}{2}\sigma_{\mathrm{z}} + \frac{\Delta}{2}\sigma_{\mathrm{x}} = \frac{1}{2}\begin{pmatrix}\varepsilon & \Delta\\ \Delta & -\varepsilon\end{pmatrix},} \tag{2.4.8}$$

where $\varepsilon = \partial U_{\mathrm{q}}/\partial f_{\mathrm{q}}$. In (2.4.8) the energy- and flux scale are chosen such that the eigenstates of $\varepsilon(f_{\mathrm{q}})$, which are given by

$$\varepsilon(f_{\mathrm{q}}) = 2I_{\mathrm{p}}\Phi_0\left(f_{\mathrm{q}}-\frac{1}{2}\right), \tag{2.4.9}$$

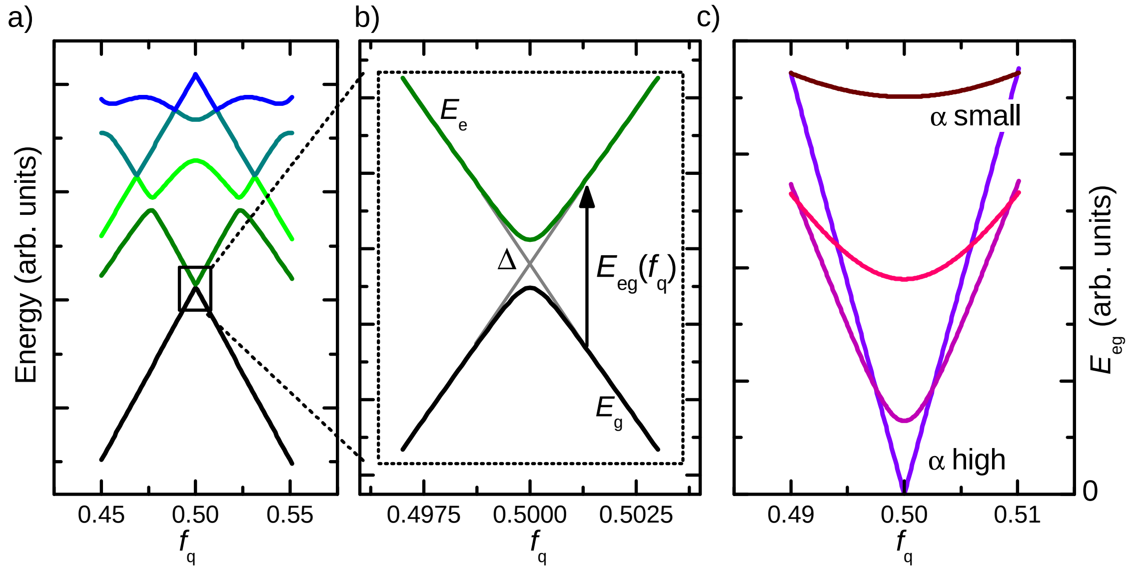

Figure 2.7 – **a)** Eigenenergies of a qubit: At $f_\mathrm{q} \approx 0.5$ higher energy levels are separated by a large energy difference, thus the two lowest energy levels can be considered as a two-level system; **b)** Enlarged view of the two lowest energy levels at $f_\mathrm{q} \approx 0.5$: The tunnel coupling Δ separates the two levels which show a classical behavior for $\Delta = 0$ (gray lines); **c)** Hyperbolic energy difference $E_\mathrm{eg}(f_\mathrm{q})$ around $f_\mathrm{q} = 0.5$ for different values of α. The minimal energy difference is small for α close to one and high for α close to 0.5. This energy difference can be measured during experiments and is in the order of several GHz$\cdot h$.

lie symmetrically around zero. For a negligible Δ the ground state $|\mathrm{g}\rangle$ and the excited state $|\mathrm{e}\rangle$ of the qubit Hamiltonian in (2.4.8) are identical to the classical persistent current states $|0\rangle$ and $|\mathrm{I}\rangle$, representing the current flowing in opposite directions. Due to a finite Δ the qubit states $|\mathrm{g}\rangle$ and $|\mathrm{e}\rangle$ are a linear superposition of $|0\rangle$ and $|\mathrm{I}\rangle$ [56].
To observe quantum mechanical behavior of $|\mathrm{g}\rangle$ and $|\mathrm{e}\rangle$ the condition $k_\mathrm{B}T \ll \Delta$ has to be fulfilled which means that for $\Delta/h \approx 4\mathrm{GHz}$ measurements have to be done at milli-Kelvin temperatures. Furthermore the parameters α, $E_\mathrm{J0}/E_\mathrm{c}$ and j_c have to fulfill the conditions mentioned earlier in this chapter.
Diagonalizing the Hamiltonian in (2.4.8) yields the eigenvalues $\pm½\sqrt{\varepsilon^2 + \Delta^2}$ which define the flux-dependent energy difference $E_\mathrm{eg}(f_\mathrm{q})$ of the two states:

$$E_\mathrm{eg}(f_\mathrm{q}) = \sqrt{\varepsilon^2 + \Delta^2} = \sqrt{4I_\mathrm{c}^2 \left(1 - \left(\frac{1}{2\alpha}\right)^2\right) \Phi_0^2 \left(f_\mathrm{q} - \frac{1}{2}\right)^2 + \Delta^2} \tag{2.4.10}$$

This energy difference is shown in Fig. 2.7c and is of the order of several GHz$\cdot h$ so it can be measured in experiments using microwave radiation to excite the qubit from its ground to its excited state.

3 Chapter
Experimental techniques

The characterization of flux qubits as discussed in chapter 4 requires a considerable experimental effort and sophisticated measuring setups. In this chapter experimental techniques as the pre-characterization of readout-SQUIDs (cf. Sec. 3.1) or the readout of flux qubits (cf. Sec. 3.2) are discussed. In Sec. 3.3 the concept of gradiometric qubits and the implementation of a tunable qubit gap are introduced. Important insights into the operation of gradiometric qubits are found in Sec. 3.4, where phase-biased SQUIDs are characterized. This chapter finishes with the discussion of the flux trapping process in Sec. 3.5, which is essential for the operation of gradiometric qubits, and a solution to on-chip heating effects in Sec. 3.6.

3.1 Characterization of dc-SQUIDs

Characterizing the Josephson junctions of a readout-SQUID is important since crucial values as E_{J0} and E_c can be extracted. The readout-SQUID junctions are identical in size and oxidation time with the qubit junctions so that E_{J0} and E_c, which mainly define a qubit's behavior, are assumed equal for SQUID and qubit.
A first estimation of the junction parameters can be made by measuring their resistance R_{rt} at room temperature. On each wafer used for fabrication there have been additional Josephson junctions in order to determine the junction's room temperature resistance without damaging the actual readout-SQUID junctions (cf. Appendix C for details). Nevertheless, due to a large spread in the junction's area and difficulties to contact the additional junctions, it turned out to be advantageous to rather make a four-point measurement at the actual readout-SQUID. For SQUID junctions with area A_J of approximately $0.03\,\mu\mathrm{m}^2$, a suitable value for the normal resistance is of the order of $200\,\Omega$ to $300\,\Omega$ to generate current densities in the superconducting state $j_c(35\mathrm{mK}) \approx 2\,\mathrm{kA/cm}^2$.
A more quantitative way to determine the junction parameters is to record a current-voltage characteristics (IVC) of a single SQUID in the superconducting state. For zero applied field, the SQUID is equivalent to a single Josephson junction with critical current $2I_c$, resistance $R_n/2$ and capacitance $C/2$ [134]. Pre-characterization is performed in a ^{3}He-evaporation cryostat which operates at approximately 500 mK and is described in

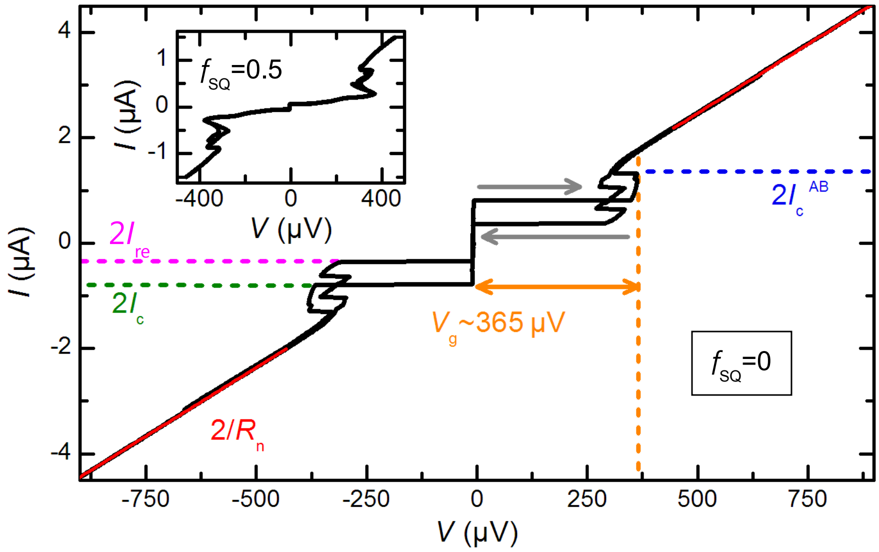

Figure 3.1 – IVC of a typical unshunted dc-SQUID fabricated during this work. The IVC shows a hysteretic behavior (gray arrows) corresponding to a small damping resulting in $I_{\mathrm{re}} < I_{\mathrm{c}}$ for $f_{\mathrm{SQ}} = 0$ (pink & green dashed lines). For zero applied magnetic field the switching current equals $2I_{\mathrm{c}}$ and a voltage drop $V_{\mathrm{g}} \approx 365\,\mu$V can be observed (orange dashed line). The slope of the ohmic part (red line) is inversely proportional to $2R_{\mathrm{n}}$ and can be used to determine I_{c}^{AB} and thus E_{J0} (blue dashed line). The inset shows the IVC recorded at a SQUID frustration $f_{\mathrm{SQ}} = 0.5$ where the switching current is strongly suppressed and no hysteresis is observable.

detail in Ref. [135]. A typical IVC of an underdamped and unshunted SQUID shows a non-linear and hysteretic behavior as shown in Fig. 3.1a. When increasing the current I above the switching current I_{sw}, the SQUID switches to the voltage state and follows a linear dependence proportional to $2/R_{\mathrm{n}}$. Decreasing the current starting in the voltage state, the retrapping into the superconducting state occurs at the current value I_{re}, which is smaller than I_{sw}. In the intermediate regime between I_{sw} and I_{re} the IVC shows a highly non-linear behavior due to self-heating effects [136].
For the operation of flux qubits the ratio $E_{\mathrm{J0}}/E_{\mathrm{c}}$ is a crucial value, where E_{J0} can be calculated from the critical current of the SQUID junctions, cf. (2.2.7). For all calculations of E_{J0} in this work the theoretical value $I_{\mathrm{c}}^{\mathrm{AB}}$ is used to calculate E_{J0}, which can be determined from the normal resistance of the SQUID junctions using (2.2.2). Although this gives only an upper limit for E_{J0} it turned out to be well suited for further calculations and for simulations performed in chapter 4.

Josephson junction capacitance

The capacitance C of a Josephson junction, which defines its charging energy E_{c}, is linked to the *Stewart-McCumber* parameter by [118, 119]

$$\beta_{\mathrm{c}} = \frac{2\pi}{\Phi_0} I_{\mathrm{sw}} R_{\mathrm{n}}^2 \cdot C. \tag{3.1.1}$$

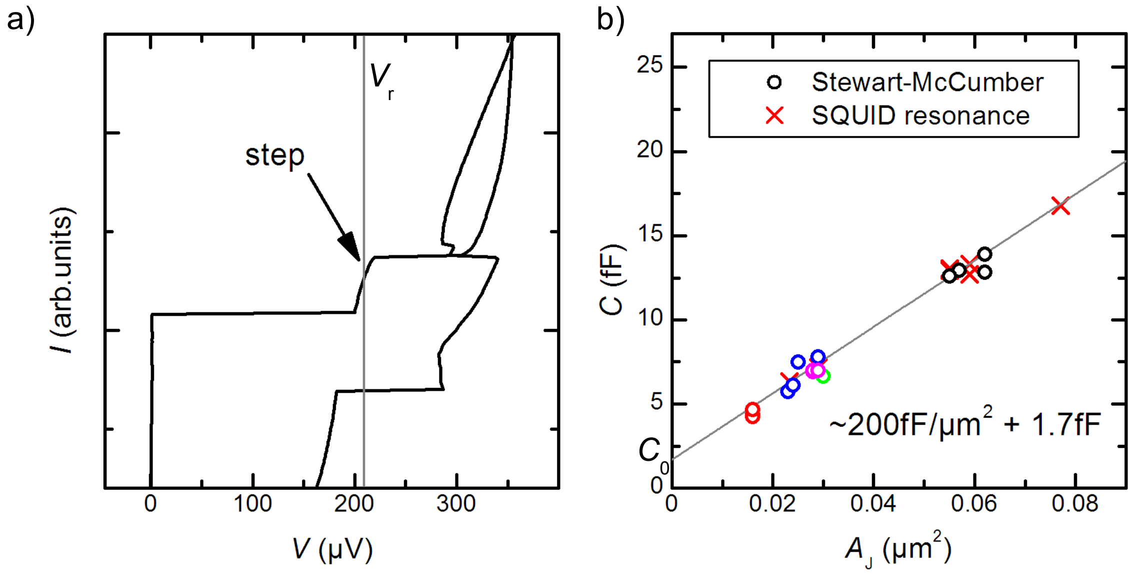

Figure 3.2 – **a)** Enlarged view of an IVC showing a resonance step at a voltage value V_r, corresponding to a junction capacitance C given by (3.1.4); **b)** Measured values of the junction capacitance C for several SQUIDs with different junction area A_J. Circles are derived from the Stewart-McCumber parameter, where the same colour denotes that the corresponding samples are located on the same wafer. Crosses are derived from dc-SQUID resonances. A linear fit to the data yields a specific capacitance $\tilde{c} = (195 \pm 10)\,\mathrm{fF}/\mu\mathrm{m}^2$ and a stray capacitance $C_0 = (1.7 \pm 0.6)\,\mathrm{fF}$.

For underdamped junctions used in this work β_c is larger than one and can be determined using the ratio $a_0 = I_{re}/I_c$ of the retrapping- to the critical current [137–139]. Using a numerical solution of (2.2.10), the Stewart-McCumber parameter can be calculated to [140]

$$\beta_c = \frac{2 - (\pi - 2)a_0}{a_0^2}, \tag{3.1.2}$$

so that the junction's capacitance can be directly determined using values extracted from the IVC. It should be noted that this is only possible for unshunted SQUIDs where the retrapping current can be clearly identified. In Fig. 3.1c the measured capacitance for all unshunted SQUIDs characterized in in this work is plotted vs. the junction area A_J, which is determined from SEM images. A linear fit to the data yields a specific capacitance $\tilde{c} = (195 \pm 10)\,\mathrm{fF}/\mu\mathrm{m}^2$ and a stray capacitance $C_0 = (1.7 \pm 0.6)\,\mathrm{fF}$. This specific capacitance is by a factor 2-6 higher than comparable values given in literature [141–145]. This could be due to a smaller effective junction area caused by a larger unevenness of the junction's surface. Nevertheless, the capacitance $C = \tilde{c} \cdot A_J + C_0$ was used for all simulations in chapter 4, which are conform to the actual measured qubit behavior.
The junction capacitance can also be determined using a dc-SQUID resonance technique [141, 146–148]. A dc-SQUID forms a resonant circuit consisting of an effective loop inductance $2L$ in series with a total capacitance $C/2$, which yields a resonance frequency

$$\nu_r = \frac{1}{2\pi} \frac{1}{\sqrt{LC}}. \tag{3.1.3}$$

Resonance steps as shown in Fig. 3.1b appear if the voltage dependent Josephson frequency $\nu_\mathrm{J}(V) = V/\Phi_0 \approx V \cdot 483\,\mathrm{MHz}/\mu\mathrm{V}$ [149] equals ν_r. Then, the junction capacitance can be calculated as

$$C = \left(\frac{\Phi_0}{2\pi}\frac{1}{V_\mathrm{r}}\right)^2 \frac{1}{L}, \tag{3.1.4}$$

where V_r is the voltage where the step appears. Resonance steps have been observed for a small number of fabricated SQUIDs, which were equipped in most cases with relatively large junctions, which had areas of approximately $A_\mathrm{J} \approx 0.06\,\mu\mathrm{m}^2$.
In Fig. 3.1c the capacitance extracted from the resonance technique is plotted as red crosses. There is a formidable agreement between the capacitance determined by either technique.

3.2 SQUID-readout of flux qubits

A schematic of the measurement setup to characterize flux qubits used in this work is shown in Fig. 3.3a. SQUID and qubit are cooled to approximately 35 mK in a ^{3}He/^{4}He-dilution refrigerator, which is described in detail in Ref. [150] & Ref. [151] and shown in Fig. A.5. The ^{3}He/^{4}He-dilution refrigerator is placed in an electromagnetically shielded room and has additional Mu-metal shields as well as a Cryoperm shield. SQUID and qubit can be frustrated by an external solenoid and the qubit can be excited by microwave radiation emitted from an antenna placed closely above the sample. The SQUID is contacted in a four-point measurement arrangement and filtered with room temperature low-pass filters as well as cryogenic copper-powder filters.
The qubit readout is performed by detecting the field dependent switching current of a readout-SQUID as shown in Fig. 3.3b. As explained in Sec. 2.3 the switching current depends on the flux penetrating the SQUID loop which allows the detection of small flux changes as for example generated by a flux qubit.
To detect the switching current depending on the SQUID frustration, a linearly increasing current I_SQ is sent through the junctions by an analog current source. The current increases with approximately $0.1\,\frac{\mu\mathrm{A}}{\mathrm{ms}}$. When I_SQ reaches I_sw, the SQUID switches to the voltage state which can with respect to a certain threshold value be detected by a comparator connected at the output of a voltage amplifier. After the switching event was detected, the current is linearly decreased back to zero. A digital multimeter receives the current value at which the switching event occurred as voltage signal from a sample and hold (S&H) stage. After each switching event an external arbitrary waveform generator triggers a new current ramp. The switching current of the SQUIDs is of the order of $0.1 - 1\,\mu\mathrm{A}$ so the trigger frequency is about 50-100 Hz.
Since quantum tunneling is a statistical process, the switching current is not defined exactly but distributed in a Gaussian pattern around a certain average value $\langle I_\mathrm{sw}\rangle$. Therefore many switching events are recorded for every flux value yielding a histogram pattern as shown in Fig. 3.4a. In most measurements presented in this work 750 switching events have been recorded per flux value.

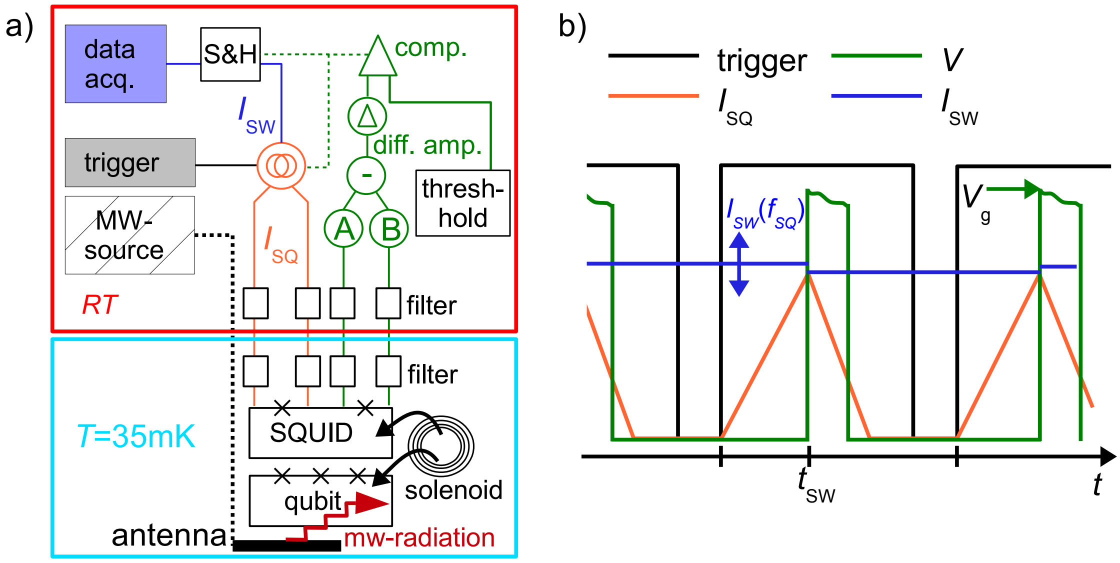

Figure 3.3 – **a)** Schematics of the measurement setup for SQUID readout: The actual experiment is performed at 35 mK (light blue box), whereas the measuring equipment is located at room temperature (red box). There are cryogenic copper-powder filters for the dc-control lines, which are additionally filtered with low-pass filters at room temperature. The microwave signal is transferred to the sample stage and irradiated by an antenna placed closely above the sample. SQUID and qubit can be frustrated with magnetic flux induced by a superconducting solenoid placed closely below the sample stage; **b)** Schematics of the measurement procedure: The f_{SQ}-depending switching current $I_{\mathrm{sw}}(f_{\mathrm{SQ}})$ of the SQUID is detected using an increasing current I_{SQ}. When $I_{\mathrm{SQ}} = I_{\mathrm{sw}}(f_{\mathrm{SQ}})$ the SQUID switches to the voltage state, which is detected with respect to a certain threshold value by a comparator. The current value I_{sw}, which is saved at a sample and hold (S&H) stage is send to the data acquisition after a trigger signal is obtained from the comparator.

Qubit signal

Detecting the switching current of a SQUID while sweeping Φ_{ext} results in a typical SQUID curve shown in Fig. 2.4c. If a flux qubit is placed very close to the SQUID, the SQUID is penetrated by the external flux and by the flux induced by the qubit. Therefore, the total flux through the SQUID is given as

$$\begin{aligned}\Phi_{\mathrm{SQ}} &= \Phi_{\mathrm{ext}} + \Phi_{\mathrm{ind,q}} \\ &= \Phi_{\mathrm{ext}} + k\sqrt{L_{\mathrm{g,SQ}} \cdot L_{\mathrm{g,q}}} \cdot I_{\mathrm{p}} \end{aligned} \tag{3.2.1}$$

where $0 \leq k \leq 1$ defines the inductive coupling strength between SQUID and qubit. $L_{\mathrm{g,SQ}}$ and $L_{\mathrm{g,SQ}}$ are the geometrical inductance of SQUID and qubit, respectively and I_{p} is the persistent qubit current. In (3.2.1) k equals one for galvanic coupling over infinite length and decreases to zero with increasing distance between the two objects. Depending on the direction of I_{p}, the qubit either adds additional flux or it lowers the flux penetrating the SQUID.

Measuring the switching current in a region f_{SQ} =¼$\pm\delta f_{\mathrm{SQ}}$, where the SQUID has a

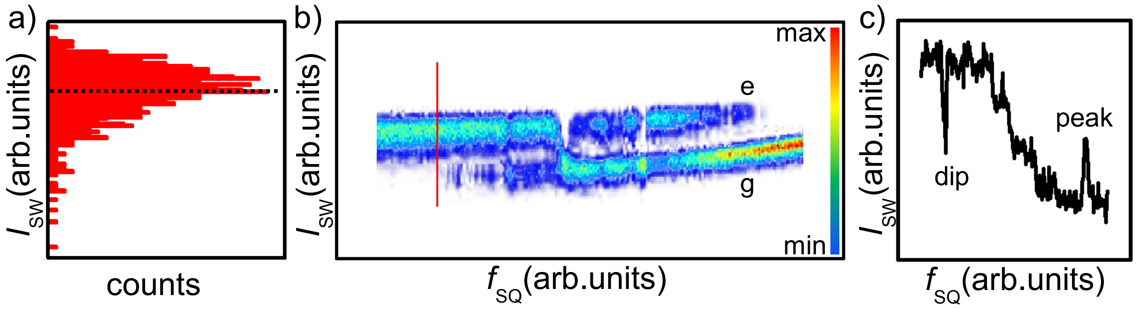

Figure 3.4 – **a)** Gaussian switching current distribution for a fixed flux value corresponding to the red line in (b). The average value $\langle I_{\rm sw}\rangle$ is indicated as a dashed line; **b)** Recording the switching current as function of $f_{\rm SQ}$ yields the signal of a qubit induced in the SQUID after subtracting a linear fit. In this graph the colour-coded switching current distributions are plotted. The qubit step consists mainly of switching events corresponding to the ground (g) state but contains also some counts in the excited (e) state; **c)** Average values of the switching current distribution for a qubit step with microwave irradiation. If the microwave frequency equals $E_{\rm eg}/h$ characteristic peaks and dips are observable.

steep and approximately linear $I_{\rm sw}(f_{\rm SQ})$-dependence, the additional flux induced by the qubit modulates the $I_{\rm sw}(f_{\rm SQ})$-curve as shown in Fig. 3.4b after a linear background is subtracted. This modulation is the so called *qubit step*, which is an indicator for the quantum mechanical behavior of the qubit. A classical bit would result in a discrete step, whereas the qubit step is smooth as a result of the superposition of persistent currents flowing simultaneously in opposite directions. Generally, the qubit parameters Δ and ε can be extracted from the qubit step itself, recording it for several temperatures in the regime $\Delta/k_{\rm b} \gg T \approx 30-300\,{\rm mK}$ [152]. But for a more reliable evaluation of these parameters a common technique, which is continuous microwave spectroscopy [56, 132], is used in this thesis.
Electromagnetic radiation in the GHz-regime is generated by a microwave source and sent through coaxial cables into the cryostat to an antenna which is placed closely above the samples. With this irradiation in the GHz-regime, qubit transitions from the ground to the excited state can be induced when the qubit absorbs the energy

$$E_{\rm mw} = h\nu_{\rm mw} \stackrel{!}{=} E_{\rm eg}(f_{\rm q}), \tag{3.2.2}$$

where $\nu_{\rm mw}$ is the microwave frequency. Such a transition becomes observable as characteristic peaks and dips as displayed in Fig. 3.4c. Recording the $f_{\rm q}$-coordinate of these peaks and dips for several frequencies results in a qubit hyberbola as given by (2.4.10).

3.3 Gradiometric qubits with tunable tunnel coupling

One disadvantage of *standard*[1] flux qubits compared to other superconducting qubit types [75, 153] is that the minimal transition frequency Δ/h is fixed during fabrication. Since Δ depends exponentially on α, the tunnel coupling can be tuned by tuning the α-value, which is proportional to the critical current of the α-junction. The critical current in turn can be tuned by replacing the α-junction with a dc-SQUID as already suggested in the very first proposal on flux qubits [1] and shown in Fig. 3.5.

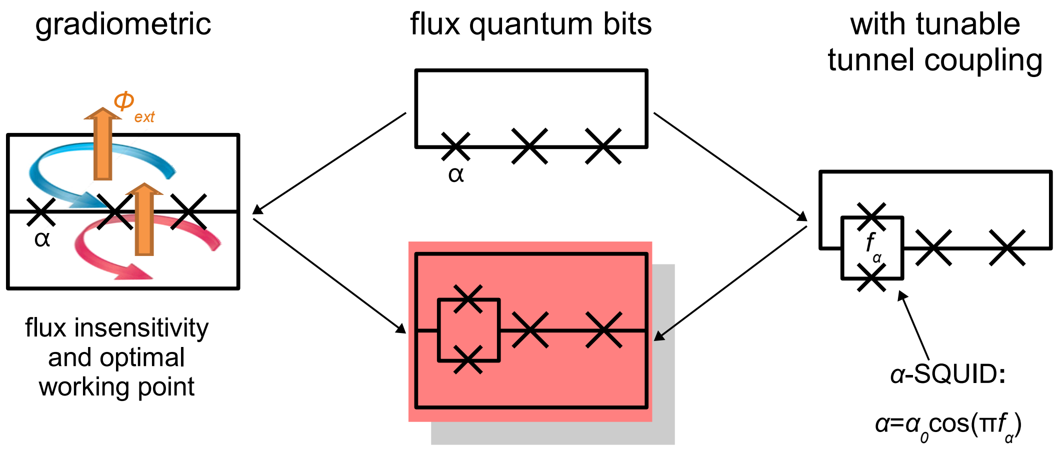

Figure 3.5 – Sketch showing how a gradiometric flux qubit with tunable tunnel coupling can be realized: The gap tuning is achieved by replacing the α-junction by a dc-SQUID (right). To avoid unwanted flux changes in the qubit loop, a gradiometric design is chosen to bias the qubit at an optimal working point (left). Combining these two concepts results in a layout as it is used in this work (bottom).

The α-SQUID modulates the Josephson energy E_{J0} of the α-junctions as a function of its frustration f_α, while E_c stays constant. The flux dependent Josephson energy $E_{\mathrm{J}\alpha}(f_\alpha)$ for the SQUID is therefore given as

$$E_{\mathrm{J}\alpha}(f_\alpha) = E_{\mathrm{J0}} \cdot \alpha(f_\alpha) = E_{\mathrm{J0}}\alpha_0|\cos(\pi f_\alpha)|, \tag{3.3.1}$$

which means that for zero applied magnetic field the α-SQUID can effectively be replaced by a junction with area $2A_{\mathrm{J,s}}$, resulting in $\alpha_0 = 2A_{\mathrm{J,s}}/A_{\mathrm{J,q}}$. Here $A_{\mathrm{J,q}}$ is the area of one of the larger qubit junctions and $A_{\mathrm{J,s}}$ is the area of one of the α-SQUID junctions. The α-SQUID junctions can be designed such that α_0 is approximately 0.7 and thus the system works as a *standard* qubit. Tunability is achieved by the fact that the actual α-value can be decreased from α_0 to zero due to the SQUID behavior. Since α can always be tuned to lower values, α_0 can even be designed to be larger than one, so that a higher sensitivity $\partial\Delta/\partial f_\alpha|_{\alpha\approx 0.7}$ is achieved (cf. 4.3.7).
Unfortunately, with this design one cannot change the frustration of the α-SQUID and simultaneously leave the frustration of the qubit loop unaffected. That means that a

[1] In the following, the qubit design presented in Fig. 2.5, which is the most commonly used design, will only be denoted as *standard* qubit.

system where only the α-junction is replaced by a SQUID is not well suited for fast changes of α since the qubit frustration has always to be readjusted. An elegant way to avoid this problem is to use a gradiometric design as shown in Fig. 3.5. A gradiometer works in a way that homogeneous magnetic fields leave the qubit phase unaffected so that one can change the frustration of the α-SQUID without changing the qubit frustration using homogeneous fields.

3.3.1 Gradiometer circuit

A gradiometric design, which will be used to bias the qubit at its flux degeneracy point, consists of two equally sized loops (1,2) with one shared line, resulting in an 8-shaped geometry as shown in Fig. 3.6a [89]. One advantage of this design compared to the *standard* qubit design is that homogeneous magnetic fields couple equally in both halves leaving the phase between two points A and B on the symmetry axis of the outer loop unaffected [90]. The center line can be interrupted by three Josephson junctions to build a qubit together with one of the two gradiometer loops.

In the outer ring, used as a trap-loop (broken blue line in Fig. 3.6a), an amount of n flux quanta can be trapped resulting in a phase difference $\theta = 2\pi n$ around the loop. Assuming ideal and identical aluminum layers, the phase difference ϕ_q between the two points A and B is therefore always πn. For the case of an odd number of trapped flux quanta, the qubit is biased at a phase π corresponding to its flux degeneracy point. This makes the use of a gradiometric design an elegant way to operate flux qubits at their optimal working point without any external field applied.

The connection between the points A and B positioned on the symmetry axis of the trap-loop also forces fluxoid quantization in each of the two smaller loops but does not affect the quantization condition of the outer loop. Fluxoid quantization in each loop is guaranteed by circulating currents I_circ and the inductance $L = L_\mathrm{g,i} + L_\mathrm{k,i}$ of either of the two half squares (cf. Fig. 3.6b). For homogeneous magnetic fields ($f_1 = f_2$) the circulating currents around loop 1 and loop 2 are equal in size and direction such that the net current I_q through the center line is zero. In this way a homogeneous magnetic field leaves the qubit phase ϕ_q unaffected such that it stays constant at πn.

The phase difference ϕ_q and thus the qubit phase can be affected by an inhomogeneous magnetic field yielding a deviation

$$\delta\phi_\mathrm{q} = 2\pi\,(f_1 - f_2) \neq 0 \tag{3.3.2}$$

from $n\pi$. In this case the currents $I_\mathrm{circ,1}$ and $I_\mathrm{circ,2}$ are not equal anymore such that $I_\mathrm{q} = I_\mathrm{circ,1} - I_\mathrm{circ,2} \neq 0$ can be handled analogously to the persistent qubit current I_p introduced in Sec. 2.4.

In the experiment the inhomogeneous magnetic field is generated by a current I_ε flowing through the ε-flux line, which is placed closely beneath the trap-loop as shown in Fig. 3.6b. This flux line couples stronger into the lower half ($f_{2\varepsilon}$) than into the upper half ($f_{1\varepsilon}$) such that $f_2 > f_1$. Estimating the difference of mutual inductance $\delta M = M_{2\varepsilon} - M_{1\varepsilon}$ between ε-line and trap-loop to be of the order of 1 pH requires an ε-current $I_\varepsilon \approx 20\,\mu\mathrm{A}$ to induce a flux difference $\delta\Phi = 10\,\mathrm{m}\Phi_0$. This flux difference is sufficient to record a qubit hyperbola

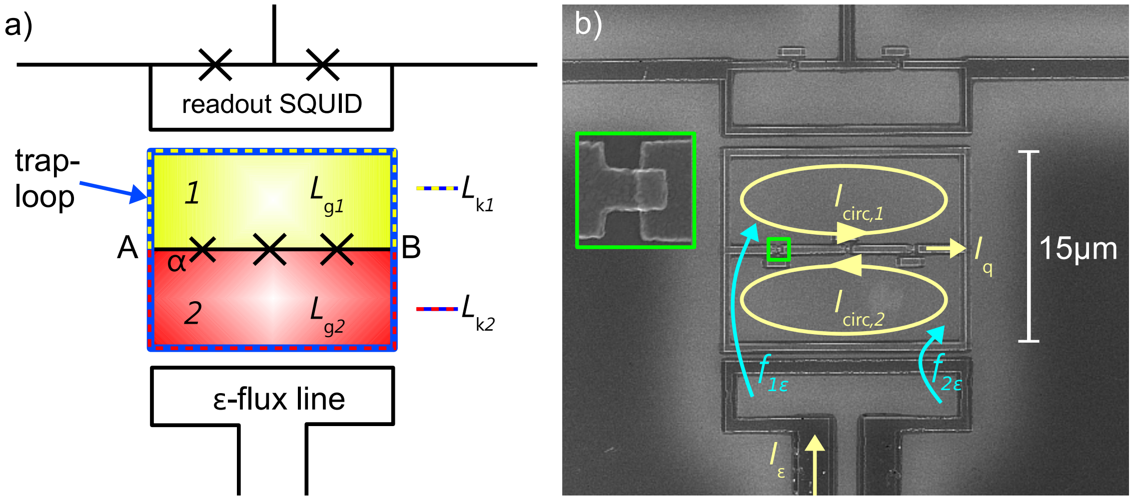

Figure 3.6 – **a)** Sketch of a gradiometric qubit with readout-SQUID and ε line: The outer ring (broken blue line) forms a trap-loop that biases the Josephson junctions between the points A and B at a phase πn, which corresponds to the flux degeneracy point for an odd number of trapped fluxoids. The qubit is formed by the three Josephson junctions together with the inductance $L = L_{\mathrm{g},i} + L_{\mathrm{k},i}$ of one of the two loops. **b)** SEM image of the system described in (a): The phase difference $\delta\phi_{\mathrm{q}}$ between A and B can be changed by inhomogeneous magnetic fields such that $f_1 \neq f_2$, which is achieved by the ε-flux line coupling stronger into the lower half than into the upper half ($f_{2\varepsilon} > f_{1\varepsilon}$). Fluxoid quantization is achieved by circulating currents $I_{\mathrm{circ},i}$, which compensate each other on the center line for homogeneous magnetic fields ($I_{\mathrm{q}} = 0$) and yield a finite current through the qubit junctions $I_{\mathrm{q}} \mathrel{\widehat{=}} I_{\mathrm{p}}$ for $f_1 \neq f_2$. The inset shows an enlarged view of one of the Josephson-junctions.

as given by (2.4.10) and agrees to measurements performed at the gradiometric design presented in Sec. 4.2.

Another advantage of the gradiometric design, besides the ability of biasing qubits at their degeneracy point, is that such systems are much less sensitive to external $1/f$-flux noise [89], which is a major reason for decoherence in flux qubits [10–14] next to charge or critical-current noise [154]. Global flux noise, which couples equally into the two loops decouples the center line from this noise source. But also local fields that couple asymmetrically into the two halves are strongly suppressed by the gradiometer. This is because the gradiometer interacts as a magnetic quadrupole, coupling with $1/r^3$, whereas the ordinary flux qubit interacts as a dipole, coupling with $1/r^2$ [90].

3.3.2 Tuning the tunnel coupling Δ

As mentioned in the beginning of Sec. 3.3, the α-junction of a qubit can be replaced by a dc-SQUID to tune the tunnel coupling Δ in situ. Furthermore, the qubit is integrated into a gradiometric design as described in the previous section to leave the qubit phase $\delta\phi_{\mathrm{q}}$ unaffected by homogeneous magnetic fields.

In the design presented in Fig. 3.7 the value α can either be changed by flux induced from an additional α-flux line placed on the symmetry axis of the gradiometer (cf. $f_{\alpha\alpha}$ in Fig. 3.7), or by homogeneous magnetic fields penetrating the trap-loop induced by a superconducting solenoid. However, the external flux Φ_{ext} cannot be linked directly to the magnetic flux inside the α-SQUID since the trap-loop tends to suppress external magnetic flux. In this section a detailed analysis concerning the flux penetrating a superconducting loop consisting of thin layers with dimensions smaller than the London penetration depth is given.

Tuning α using a solenoid

Without fluxoid quantization, a homogeneous magnetic field generated by an external solenoid would provide a frustration $f_{\mathrm{tr}} = \Phi_{\mathrm{tr}}/\Phi_0$ of the trap-loop, which would also result in a finite frustration f_α of the α-SQUID. Due to fluxoid quantization the applied magnetic flux does not equal the actual magnetic flux through the trap-loop, which can be characterized by a factor $\beta = L_{\mathrm{g}}/L_{\mathrm{k}}$ given as the ratio of geometric to kinetic inductance [155]. This factor represents the ability of the loop to preserve its actual frustration $f_{\mathrm{tr,act}}$, which means that for $\beta \gg 1$ the loop always keeps the same actual frustration $f_{\mathrm{tr,act}}$ even if the external applied frustration f_{tr} is changed, but for $\beta \ll 1$ the actual frustration can more easily be changed using external fields.
To calculate the actual frustration of the trap-loop, it is therefore essential to know how much of the phase difference $\theta = 2\pi n$ around the trap-loop is generated by a kinetic part ϕ_{k} and how much by a geometric contribution ϕ_{g}. In order to calculate either ϕ_{k} or ϕ_{g}, one can rewrite (2.1.7) to

$$\begin{aligned} 2\pi f_{\mathrm{tr}} + \phi_{\mathrm{k}} + 2\pi \frac{L_{\mathrm{g}} I_{\mathrm{circ}}}{\Phi_0} &= 2\pi \cdot n \\ 2\pi f_{\mathrm{tr}} + \phi_{\mathrm{k}} + \beta\phi_{\mathrm{k}} &= 2\pi \cdot n. \end{aligned} \tag{3.3.3}$$

After rearranging (3.3.3), the phase difference induced by kinetic inductance for n fluxoids trapped and for finite frustration f_{tr} is obtained as [106]:

$$\phi_{\mathrm{k}} = 2\pi \frac{n - f_{\mathrm{tr}}}{1+\beta}. \tag{3.3.4}$$

The contribution $\phi_{\mathrm{g}} = \beta\phi_{\mathrm{k}}$, corresponding to the geometric inductance, generates the self-induced frustration

$$f_{\mathrm{ind}} = \frac{\Phi_{\mathrm{ind}}}{\Phi_0} = \frac{\beta}{1+\beta}(n - f_{\mathrm{tr}}), \tag{3.3.5}$$

which results in an actual frustration

$$\boxed{f_{\mathrm{tr,act}} = f_{\mathrm{tr}} + f_{\mathrm{ind}} = \frac{1}{1+\beta} f_{\mathrm{tr}} + \frac{\beta}{1+\beta} n.} \tag{3.3.6}$$

of the trap-loop. For $\beta \gg 1$ the flux part dominates so that $f_{\mathrm{tr,act}} \approx n$ and $\phi_k \approx 0$, which means that such a system is not suited for building a tunable qubit since the frustration inside the trap-loop can only be changed stepwise by varying n. For $\beta \ll 1$ the kinetic

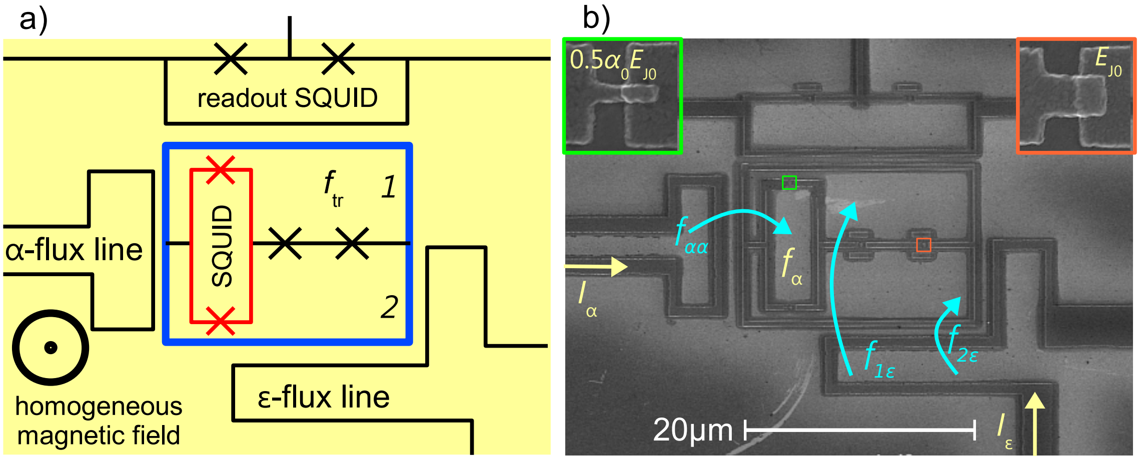

Figure 3.7 – **a)** Sketch of a gradiometric qubit with tunable tunnel coupling: The α-junction is replaced by a dc-SQUID (red), modulating the Josephson energy $E_J(\alpha) = E_{J0}\alpha_0|\cos(\pi f_\alpha)|$. A homogeneous magnetic field (yellow background) changes the frustration f_α of the α-SQUID but does not change the qubit phase $\delta\phi_q$. An additional α-flux line is placed on the symmetry axis of the gradiometer, coupling equally into both halves (1,2), which does not affect $\delta\phi_q$ but changes f_α; **b)** SEM image of the system described in (a): The qubit phase is changed, as described in the previous section, via an ε-current I_ε inducing a frustration $f_{2,\varepsilon}$ larger than $f_{1,\varepsilon}$. A current I_α through the α-flux line induces an additional frustration $f_{\alpha\alpha}$ in the α-SQUID. The insets show an enlarged view of two of the Josephson junctions. The green framed junction belongs to the α-SQUID and has a Josephson energy $E_J = 0.5\alpha_0 E_{J0}$. The orange framed junction is one of the two regular sized qubit junctions with Josephson energy E_{J0}.

part is dominant so that $\phi_k \approx 2\pi(n - f_{tr})$ and $f_{tr,act} \approx f_{tr}$. Trap-loop geometries realized in this work have dimensions of several μm and thus β-values of the order of 1. These the systems are in an intermediate regime where part of the fluxoid is generated kinetically and part is generated geometrically.
Following (3.3.6), the actual frustration $f_{\alpha,act}$ of the α-SQUID is given as

$$f_{\alpha,act} = \frac{A_\alpha}{A_{tr}} f_{tr,act} = \frac{A_\alpha}{A_{tr}} \left[\frac{1}{1+\beta} f_{tr} + \frac{\beta}{1+\beta} n \right], \tag{3.3.7}$$

where A_α/A_{trap} is the ratio of the areas of α- and trap-loop. A change of $f_{\alpha,act}$ modulates the Josephson energy of the two α-SQUID junctions, so that the actual α value is obtained as

$$\alpha = \alpha_0 \left|\cos\left(\pi f_{\alpha,act}\right)\right| = \alpha_0 \left| \cos\left(\pi \frac{A_\alpha}{A_{tr}} \left[\frac{1}{1+\beta} f_{tr} + \frac{\beta}{1+\beta} n \right] \right) \right|. \tag{3.3.8}$$

From (3.3.8) it follows that depending on β the value α can be either continuously changed by external magnetic fields causing a frustration proportional to f_{tr} or stepwise by the number n of trapped fluxoids.
It should be noted that (3.3.7) only represents the case where the α-SQUID shares no segment with the trap-loop. For a situation where the α-SQUID shares a segment with the trap-loop (cf. Ref. [18]) the ϕ_k-term of (3.3.4) has also to be considered.

Tuning α using an on-chip flux line

A second method to change $f_{\alpha,\mathrm{act}}$, next to using a homogeneous magnetic field induced by a solenoid, is to use an on-chip flux line as shown in Fig. 3.7. If such a flux line is placed on the symmetry axis of the gradiometer, the induced field couples equally into the upper and the lower half such that the qubit phase $\delta\phi_{\mathrm{q}}$ is not affected. This is the main difference to the ε-flux line that is placed perpendicular to the symmetry axis and can thus be used to change $\delta\phi_{\mathrm{q}}$. Due to a finite mutual inductance $M_{\alpha\alpha}$ between α-line and α-SQUID, a current I_α through the flux line induces a magnetic frustration

$$f_{\alpha\alpha} = \frac{1}{\Phi_0}\frac{1}{1+\beta}M_{\alpha\alpha}I_\alpha. \tag{3.3.9}$$

The samples presented in this thesis are designed such that $\alpha_0 \approx 1$, which means that a frustration of $f_{\alpha\alpha} = 1/3$ is required to tune α from 1 to 0.5. The mutual inductance $M_{\alpha\alpha}$ for the given geometry is of the order of 1 pH and β is of the order of one, so that a current through the α-line $I_\alpha \approx 1.5\,\mathrm{mA}$ is required to tune α down to 0.5.
As described in Sec. 3.6 the maximum current through an on-chip line is limited due to heating effects, which means that $I_\alpha \approx 1.5\,\mathrm{mA}$ cannot be reached during the experiment. However, one can use the external solenoid or a certain amount of trapped flux quanta to bias the α-SQUID close to $\alpha = 0.7$ and use the on-chip line for fine tuning.

3.4 Phase-biased SQUIDs

To estimate the factor β, which characterizes the ability to frustrate a trap-loop as described in the previous section, phase-biased SQUIDs as shown in Fig. 3.8a can be used [106]. A phase-biased SQUID has a trap-loop integrated into the SQUID loop, sharing a segment a of the trap-loop circumference s. This allows to shift the I_{sw}-curve of the SQUID in f_{SQ}-direction and to change the oscillation *frequency*[2] as shown in Fig. 3.8b.

3.4.1 Working principle of phase-biasing

For a standard SQUID the magnetic field dependence of the switching current is given by (2.3.1). Due to the shared segment a of the total trap-loop circumference s there is an additional contribution $a/s \cdot \phi_{\mathrm{k,tr}}$ to the kinetic phase difference $\phi_{\mathrm{k,SQ}}$ of the SQUID [156]. Furthermore, the trap-loop adds a frustration f_{M} to the SQUID caused by a mutual inductance M_{g} between trap-loop and SQUID. This frustration can be derived in analogy to (3.3.5), where the self-induced field inside a trap-loop is given. In the case of a phase-biased SQUID, the field is induced outside the trap-loop so that the direction and thus the sign of f_{M} is inverted:

$$f_{\mathrm{M}} = -\frac{\frac{M_{\mathrm{g}}}{L_{\mathrm{k}}}}{1+\beta}(n - f_{\mathrm{tr}}). \tag{3.4.1}$$

[2] It should be noted that the word *frequency* used here and in the rest of this section does not describe a time-dependent frequency but the difference in frustration resulting in one oscillation of the switching current curve of a phase-biased SQUID.

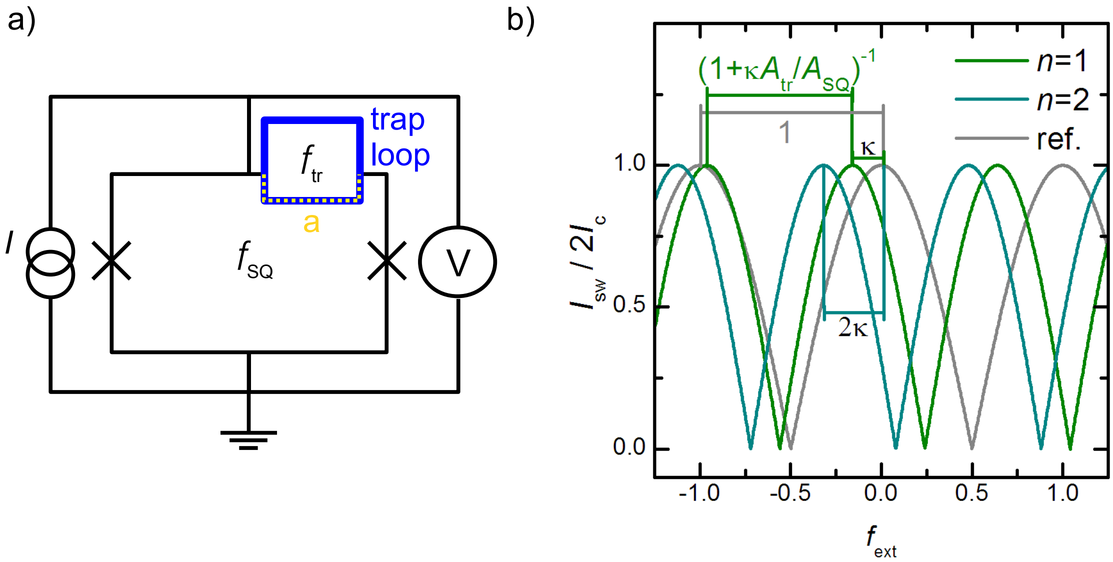

Figure 3.8 – **a)** Equivalent circuit of a phase-biased SQUID: A trap-loop (blue) is integrated in the SQUID sharing a segment a (dotted yellow) of the trap-loop circumference s. The trap-loop frustration f_{tr} can be calculated from the SQUID frustration and the ratio of the ares $A_{\mathrm{tr}}/A_{\mathrm{SQ}}$; **b)** Calculated switching-current curves for $n = 1$ and $n = 2$ (green and turquoise, respectively) using (3.4.2) with $\kappa = 0.2$ and $A_{\mathrm{tr}}/A_{\mathrm{SQ}} = 1.25$ plotted vs. the external applied frustration of the SQUID loop. The gray curve represents a reference SQUID with no trap-loop included. The phase-biased SQUID curves are shifted in f_{ext}-direction by a value κn and the oscillation period is changed by the factor $(1 + \kappa A_{\mathrm{tr}}/A_{\mathrm{SQ}})^{-1}$.

Modifying the f_{SQ}-depending switching current dependence of a SQUID, given in (2.3.1) with $a/s \cdot \phi_{\mathrm{k,tr}}$ and f_{M} one obtains

$$\begin{aligned} I_{\mathrm{sw}}(f_{\mathrm{SQ}},n) &= 2I_{\mathrm{c}} \left| \cos\left(\pi f_{\mathrm{SQ}} + \frac{1}{2}\frac{a}{s}\phi_{\mathrm{k,tr}} + \pi f_{\mathrm{M}}\right)\right| \\ &= 2I_{\mathrm{c}} \left| \cos\left(\pi f_{\mathrm{SQ}}\left[1 + \kappa\frac{A_{\mathrm{tr}}}{A_{\mathrm{SQ}}}\right] - \kappa\pi n\right)\right|, \end{aligned} \tag{3.4.2}$$

where

$$\kappa = \frac{\frac{a}{s} + \frac{M_{\mathrm{g}}}{L_{\mathrm{k}}}}{1+\beta} \tag{3.4.3}$$

and $A_{\mathrm{SQ}}/A_{\mathrm{tr}}$ is the ratio of SQUID area to trap-loop area. Equation (3.4.2) implies that the modulation *frequency* of I_{sw} is changed by the factor $(1 + \kappa A_{\mathrm{tr}}/A_{\mathrm{SQ}})$ and the phase is shifted stepwise by $\kappa\pi n$. If A_{tr} is small compared to A_{SQ}, the ratios $M_{\mathrm{g}}/L_{\mathrm{g}}$ and a/s are equal so that $\kappa \approx a/s$, which can be used to bias a SQUID exactly at a phase π using $a/s = 0.5$ [106].

3.4.2 Characterization of phase-biased SQUIDs

Unfortunately, the value β cannot be determined exactly using only switching current measurements of phase-biased SQUIDs since the physical system described by (3.4.2) has too many unknown. In the following an estimation of $\beta = L_\mathrm{g}/L_\mathrm{k}$ is made using calculations for L_g on the one hand and an estimation of L_k using room temperature resistance values of the aluminum layers on the other hand. Switching current measurements of SQUIDs are finally performed to check whether the estimations for β yield reasonable values for M_g.

Loop inductance

An approximation of the factor β for a certain loop geometry can be made by determining the kinetic inductance of the loop from its normal resistance and by calculating its geometric inductance using an approximation for the low frequency[3] limit as given in Ref. [157]. In the *dirty limit* of superconductivity the kinetic inductance of a superconducting wire can be calculated from its resistance in the normal state [105]. The aluminum layers used in this work can be considered to be in the dirty limit of superconductivity, where the BCS coherence length at zero temperature ξ_0 is much larger than the mean free path l_tr [158, 159]. In this case the London coefficient Λ_L can be approximated to [105, 155]

$$\Lambda_\mathrm{L} \approx \frac{\hbar \rho_\mathrm{n}}{\pi \Delta_0}, \tag{3.4.4}$$

where $\rho_\mathrm{n} = R_\mathrm{n} A_\mathrm{w}/s$ is the resistivity of the superconducting material with cross section A_w and length s in the normal state and $2\Delta_0$ is the energy gap of the superconductor at $T = 0\,\mathrm{K}$. Using (2.1.6), the kinetic inductance can be expressed as

$$L_\mathrm{k} = \frac{\hbar R_\mathrm{n}}{\pi \Delta_0}. \tag{3.4.5}$$

To measure the normal resistance of the aluminum layers, several structures have been fabricated as shown in Fig. A.6. The cross section of the aluminum layers is fixed during fabrication to be $A_\mathrm{w} = (506 \cdot 90)\,\mathrm{nm}^2$, whereas length s and shape of the loops has been varied in different samples.
From the resistance measurements a specific inductance $l_\mathrm{k} \approx 1\,\frac{\mathrm{pH}}{\mu\mathrm{m}}$ was obtained (cf. Appendix C for details), which is in very good agreement with comparable values given in literature (cf. Ref. [104]). The calculated values for L_g and L_k are shown in table 3.1.

SQUID measurements

The value κ can be measured either from a phase shift, which is proportional to $\kappa\pi n$, or from a *frequency* change proportional to $(1 + \kappa A_\mathrm{tr}/A_\mathrm{SQ})$, cf. (3.4.2). To detect the *frequency* a reference SQUID without trap-loop but equal area as the phase-biased SQUID is required to calibrate the field-generating solenoid.

[3] Here the time-dependent frequency is meant, so that the dc-case is described by the *low frequency limit*.

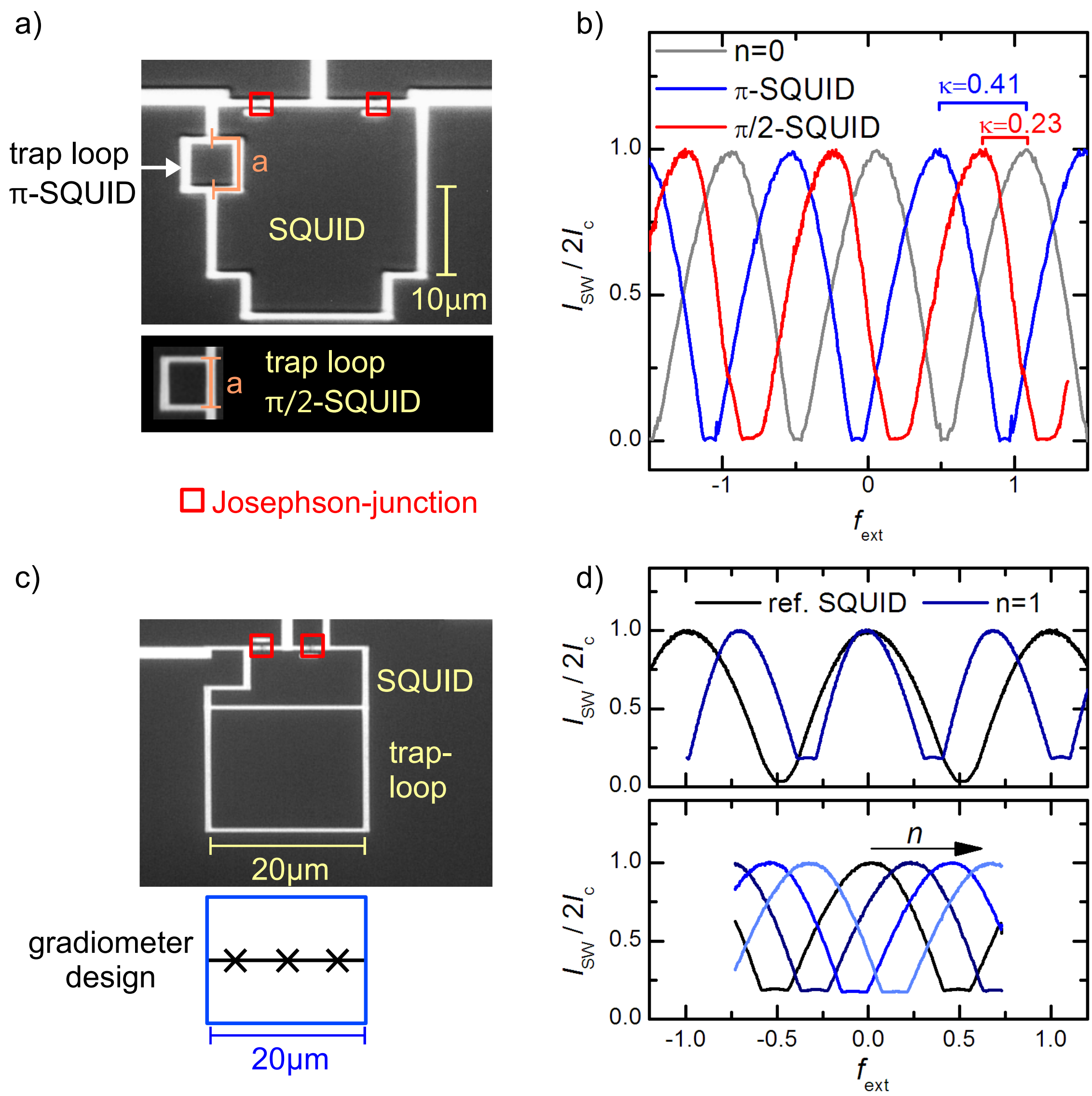

Figure 3.9 – **a) Top:** Microscope image of the π-SQUID: The trap-loop shares half of its circumference with the SQUID loop ($a/s = 0.5$). **Bottom:** Section of the $\pi/2$-SQUID which only shows the trap-loop with $a/s = 1/4$; **b)** Switching current of the π- and the $\pi/2$-SQUID for $n = 1$ (blue and red, respectively) as function of external frustration f_{ext}. The unshifted curve for $n = 0$ is shown in gray for clarity. The π-SQUID is shifted by $\kappa = 0.409$ and the $\pi/2$-SQUID by $\kappa = 0.230$; **c)** Microscope image of a SQUID that is biased with a trap-loop equally sized as the gradiometer trap-loop, which is drawn for clarity below; **d) Top:** Switching current of the phase-biased SQUID shown in (c) as a function of external frustration f_{ext} (blue), compared to a reference SQUID without trap-loop (black). The curve for $n = 1$ is shifted by hand in f_{ext}-direction such that the maxima coincide at $f_{\mathrm{ext}} = 0$. From the difference in oscillation period compared to the reference SQUID one can determine the value κ. The modulation depth of the I_{sw}-curve is decreased, which could be due to an increased screening parameter β_{L} since the phase biased SQUID has a larger inductance or due to readout problems; **Bottom:** Switching current recorded for different amounts n of trapped fluxoids, which shifts the I_{sw}-curve proportional to $\kappa n = 0.18 \cdot n$.

In the following the results of two phase-biased SQUIDs with ratio a/s=½ and a/s=¼ will be discussed. These phase-biased SQUIDs correspond to the so called π-SQUID and the $\pi/2$-SQUID, respectively, which can be used to probe whether a phase-bias of π as desired for the gradiometric qubit can be realized. Additionally, a phase-biased SQUID with equally sized trap-loop as the trap-loop of the gradiometric qubits (cf. Fig. 3.9c) is analyzed. This allows important conclusions concerning this trap-loop design, especially the ability to frustrate the α-SQUID as described in Sec.3.3.2 can be estimated. The characterization of additional phase-biased SQUIDs is discussed in Appendix C.

Table 3.1 – Measured and calculated values for the different phase-biased SQUIDs. The ratio a/s representing the shared segment a of the total trap-loop circumference is set during fabrication. The values for L_g are calculated and the values for L_k estimated from normal resistance measurements. κ is measured from the phase shift and from the *frequency* change compared to a reference SQUID. For the π and the $\pi/2$-SQUID no such reference SQUID was cooled down so that these values for κ(frequency) are missing. Using the κ-values one can make a consistency-check of the resulting values for M_g.

sample	$\frac{a}{s}$	L_g [pH]	L_k [pH]	β	κ (phase)	κ(frequency)	M_g [pH]
π-SQUID	0.500	11	20	0.550	0.409	-	2.68
$\pi/2$-SQUID	0.250	11	20	0.550	0.230	-	2.13
gradiometer design	0.286	57	70	0.814	0.182	0.179	3.37

The π- and the $\pi/2$-SQUID To clarify whether a phase-biasing of π is reliably working, a quadratic trap-loop was integrated into a SQUID sharing exactly one half of its circumference as well as its area as shown in Fig. 3.9a. The area was chosen to be small compared to the SQUID area ($A_\mathrm{tr}/A_\mathrm{SQ} = 0.06$) such that one can neglect M_g and the value of κ should be close to ½. Such a setup has the same effect as using a π-junction which can also be used to phase-bias a qubit at its degeneracy point [160].
The corresponding $\pi/2$-SQUID was fabricated identically to the π-SQUID with the only difference that the trap-loop in this case shares just one of its edges (a/s =¼) as shown in the inset of Fig. 3.9a, so that the SQUID should be biased at a phase $\pi/2$.
The resulting I_sw-curves for the π- and $\pi/2$-SQUID are shown in Fig. 3.9b for the case $n = 0$ and $n = 1$. The displacement Δf_SQ between the curve for $n = 1$ and $n = 2$ can be used to determine κ, which is achieved by a fit of (3.4.2) to the data. The results for both phase-biased SQUIDs are shown in table 3.1. For the π and the $\pi/2$-SQUID the value κ could be only determined from the phase shift since no reference SQUID was cooled down during these measurements.
The fact that κ is smaller than expected ($\kappa(\pi-\mathrm{SQUID}) = 0.409, \kappa(\pi/2-\mathrm{SQUID}) = 0.230$) shows that the assumption of a negligible inductance is not applicable in this case.The deviation from $\kappa = 0.5$ and $\kappa = 0.25$, respectively, could also be due to the fact that the aluminum layer of the SQUID loop has a finite extent at both points where it contacts the trap-loop. This extent, which is $2d = 2 \cdot 506\,\mathrm{nm}$, is approximately 6% of the total circumference s and thus not negligible for calculating the ratio a/s. Using (3.4.3), the mutual inductance is estimated to $M_\mathrm{g} \approx 2.5\,\mathrm{pH}$.

However, the deviation from $\kappa = 0.5$ should be no obstruction for the use of a gradiometric design to phase-bias a qubit at a phase π. This is because in the case of a gradiometric design the phase-biased system, which is the qubit, is placed inside the trap-loop so that the mutual inductance couples equally into both loops.

Characterizing the qubit trap-loop To gain information about the factor β belonging to the trap-loop of the gradiometric qubits, a phase-biased SQUID with an integrated trap-loop equally designed as the one used for the gradiometers has been fabricated (cf. Fig. 3.9c). This alignment of trap-loop and SQUID also corresponds to a setup in which the gradiometric qubit is coupled galvanically to the readout-SQUID, which will be an improvement of the system used in this thesis in the matter of readout quality.
For this design the value κ was determined from both, the phase and the *frequency* part, where the latter was done by detecting the *frequency* change of I_{sw} compared to a reference SQUID. For a given ratio $A_{\mathrm{tr}}/A_{\mathrm{SQ}}$ between trap-loop and SQUID area, one obtains

$$\kappa(\text{frequency}) = \frac{A_{\mathrm{SQ}}}{A_{\mathrm{tr}}}\left(\frac{f_{\mathrm{ref}}}{f_{\mathrm{pb}}} - 1\right), \tag{3.4.6}$$

where f_{ref} and f_{pb} is the oscillation period of reference and phase biased SQUID, respectively. Figure 3.9d shows the f_{ext}-depending switching current of reference and phase-biased SQUID. The value κ determined from these measurements is $\kappa = 0.179$ (cf. table 3.1). Considering a uncertainty of the measured areas A_{tr} and A_{SQ} as well as of the ratio a/s, resulting in an error $\delta\kappa \approx \pm 0.041$, the result for κ is in good agreement with $\kappa = 0.182$ extracted from the phase part. Assuming $\kappa \approx 0.18$, the mutual inductance is calculated to $M_{\mathrm{g}} = 3.37\,\mathrm{pH}$, using that $\beta = 0.814$.

Summarizing, there are two central results of the phase-biased SQUID measurements presented in this section: On the one hand the phase-biasing itself is reliably working and can be used to bias a qubit at a phase π and on the other hand the frustration of the α-SQUID can be changed by applying approximately twice the flux that is expected without fluxoid quantization, so that $f_{\alpha,\mathrm{act}} \approx 0.55 f_{\alpha}$ using (3.3.7) and $\beta \approx 0.8$.

3.5 Flux trapping

The concept of trap-loops and gradiometric designs is based on a reliable technique to trap a certain amount of fluxoids in a given geometry. During this thesis a flux-trapping process for a ^{3}He evaporation refrigerator as well as for a ^{3}He/^{4}He dilution refrigerator has been explored.
To trap an amount of n flux quanta, the aluminum loop has to be heated above its critical temperature $T_{\mathrm{c}} \approx 1.2\,\mathrm{K}$ while it is frustrated at $f_{\mathrm{app}} = n$. As described in Sec. 2.1 it is sufficient if the frustration is only close to n since the loop starts a persistent current that compensates the missing flux to the next integer value. However, to reach the desired value of n trapped flux quanta and to avoid that there will be $n \pm 1$ fluxoids trapped, the mismatch must not exceed $|f_{\mathrm{app}} - n| = 0.5$ during the transition into the superconducting

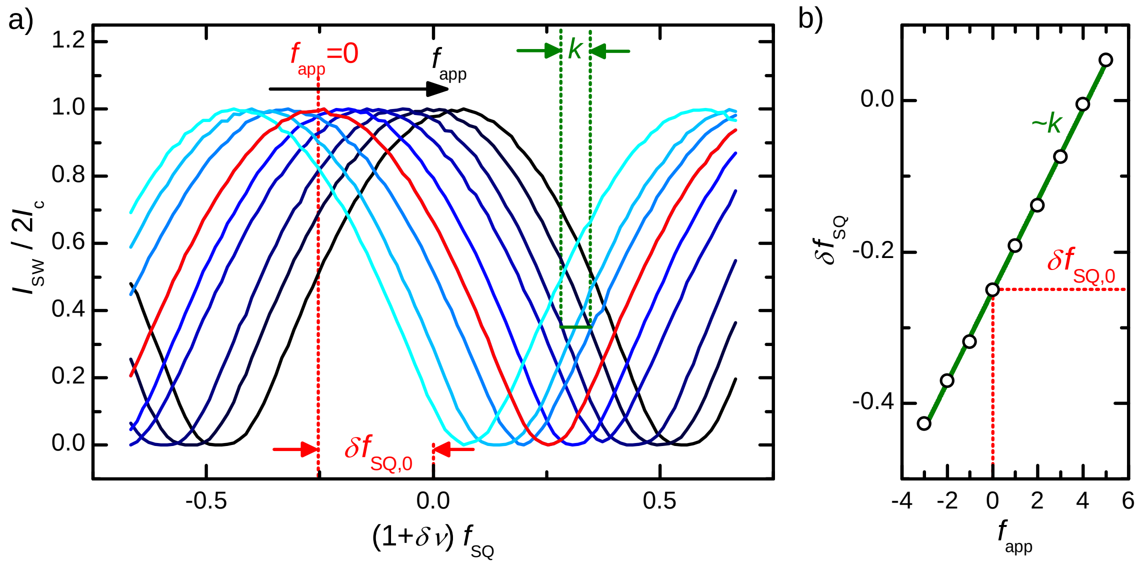

Figure 3.10 – **a)** Switching current I_{sw} of a readout-SQUID for different values of trapped flux quanta n in the trap-loop, recorded as a function of external frustration f_{SQ}. The curves are shifted stepwise in f_{SQ}-direction proportional to n. The curve corresponding to $f_{\text{app}} = 0$ (red) is not centered with respect to $f_{\text{SQ}} = 0$, which means that there is additional flux in the loop; **b)** Displacement δf_{SQ} vs. the amount of trapped flux quanta n. The slope k of a linear fit can be used to calculate $\delta\nu$ and the y-axis intercept $\delta f_{\text{SQ},0}$ is used to determine the background field B_{b}.

state. This transition into the superconducting state will be called *cool down* in the following.
Flux trapping is possible up to a critical value n_{max} where the circulating current

$$I_{\text{circ}} = \Phi_0 \frac{n - f_{\text{tr}}}{L_{\text{k}} + L_{\text{g}}} \tag{3.5.1}$$

reaches the critical current of the wires. For geometries used in this work with $L_{\text{k}} + L_{\text{g}} \approx 114\,\text{pH}$, the actual circulating current can be approximated to $I_{\text{circ}} = 17\mu\text{A}(n - f_{\text{tr}})$. Assuming the critical current of the wire to be of the order of some mA and neglecting external frustration means that n_{max} is larger than 50 and thus larger than typical values for n used in this thesis, where $|n| \lesssim 9$.

For experimental reasons it is not only important to be able to trap flux quanta but also to detect whether the flux trapping process was successful and to determine how many flux quanta have been trapped. This can be achieved by comparing the SQUID's switching current curve before and after the flux trapping process.
Following the derivation of (3.4.2) for only mutual inductance M_{g} and no shared segement a between trap-loop and SQUID, the switching current dependence for a SQUID with a trap-loop placed nearby can be expressed as

$$I_{\mathrm{sw}}(f_{\mathrm{SQ}},n) = 2I_{\mathrm{c}} \left| \cos\left(\pi f_{\mathrm{SQ}} \left[1 + \underbrace{\frac{A_{\mathrm{tr}}}{A_{\mathrm{SQ}}} \frac{\frac{M_{\mathrm{g}}}{L_{\mathrm{k}}}}{1+\beta}}_{\delta\nu} \right] - \pi n \underbrace{\frac{\frac{M_{\mathrm{g}}}{L_{\mathrm{k}}}}{1+\beta}}_{k} \right) \right| . \tag{3.5.2}$$

Equation (3.5.2) implies that the change of trapped flux quanta after the flux trapping process can be detected as a stepwise displacement $\delta f_{\mathrm{SQ}}(n)$ of the switching current-curve, which is equal to $k \cdot n$ (cf. Fig. 3.10a). Furthermore, the oscillation *frequency* of the SQUID is changed by a factor $(1 + \delta\nu)$. This *frequency* change, which is caused by the additional induced flux of the trap-loop, cannot be observed during the experiment since there is no reference SQUID to calibrate the actual flux-scale. However, since the switching current curve given by (3.5.2) will be used to calculate the applied flux to the trap-loop, it is indispensable to estimate $\delta\nu$. This estimation can be performed using the value k, which is linked to $\delta\nu$ via the ratio $A_{\mathrm{tr}}/A_{\mathrm{SQ}}$. The value k can be determined by recording the displacement $\delta f_{\mathrm{SQ}}(n)$ of the first maximum of the I_{sw}-curve for various n as shown in Fig. 3.10b, so that one obtains

$$\delta f_{\mathrm{SQ}}(n) = \delta f_{\mathrm{SQ},0} + kn \tag{3.5.3}$$

between the shift of the switching current curve and n.

Background field in the dilution refrigerator

In principle, for no applied field ($f_{\mathrm{app}} = 0$) during cool down the switching current curve is expected to be centered symmetrically around $f_{\mathrm{SQ}} = 0$, i.e. $\delta f_{\mathrm{SQ},0} = 0$. However, in Fig. 3.10 a finite displacement $\delta f_{\mathrm{SQ},0} \neq 0$ for the case $f_{\mathrm{app}} = 0$ during cool-down can be observed. This shows that there is a finite frustration of the readout-SQUID even though there is no magnetic field applied and there was no magnetic field applied during cool down. This issue has been observed during all measurements performed in the ^{3}He/^{4}He dilution refrigerator and is most probably caused by a constant but not shieldable magnetic field B_{b} in the dilution fridge, since it was not observed for identical samples in the ^{3}He evaporation refrigerator.
The assumption of a finite background field rises the question whether there is already a certain amount of flux quanta trapped for $f_{\mathrm{app}} = 0$ during cool down, or not. This is essential to know since for the operation of gradiometric qubits one needs to be sure to have an odd number of flux quanta trapped and for tunable qubits one even wants to be sure of the exact amount of trapped flux quanta.
The SQUID frustration $\tilde{f}_{\mathrm{SQ}}$ that is generated by a background field is composed of a frustration $f_{\mathrm{SQ,b}} = B_{\mathrm{b}} A_{\mathrm{SQ}}/\Phi_0$ directly induced by the background field as well as of a frustration $f_{\mathrm{M,b}} = k(f_{\mathrm{tr,b}} - n_{\mathrm{b}})$ induced by the trap-loop. Here $f_{\mathrm{tr,b}} = B_{\mathrm{b}} A_{\mathrm{tr}}/\Phi_0$ and n_{b} is the amount of flux quanta trapped due to the existing background field B_{b} during cool down.
To determine the value n_{b} one can calculate the trap-loop frustration

$$f_{\mathrm{tr,b}} = \frac{\delta f_{\mathrm{SQ},0} - k n_{\mathrm{b}}}{1 + \delta\nu} \tag{3.5.4}$$

for different values n_{b} and check whether the calculated frustration lies within $(n_{\mathrm{b}} - 0.5) > f_{\mathrm{tr,b}} > (n_{\mathrm{b}} + 0.5)$. This should be true for only one value of n_{b}. Here $\delta f_{\mathrm{SQ},0}$ such as k and thus $\delta\nu$, are obtained by a linear fit of (3.5.3) to the the maxima of the shifted $I_{\mathrm{sw}}(f_{\mathrm{SQ}=0}, n)$-curve.
From a calculation of $f_{\mathrm{tr,b}}$ one obtains for the three characterized gradiometric qubits that $n_{\mathrm{b}} = -1$, i.e. there is already one flux quantum trapped for zero applied fields during cool down, which is in agreement with the fact that the gradiometric qubits showed qubit steps only for even values of f_{app} (cf. Sec. 4.2). The corresponding frustration $f_{\mathrm{tr,b}} \approx 0.8$ means that the strength of background field is $B_{\mathrm{b}} \approx 6\,\mu\mathrm{T}$, which is approximately 14% of the magnetic field of the earth.

3.6 Heating effects of control circuits

The working principle of a gradiometric qubit is based on the fact that an ε-line as shown in Fig. 3.6 induces a locally inhomogeneous magnetic field via mutual inductance in the trap-loop. Consequently, the ε-line also induces a field $\Phi = M_{\mathrm{SQ},\varepsilon} I_\varepsilon$ in the SQUID. Since the induced field changes linear with I_ε, the I_ε-dependent switching current curve of the SQUID should be given by $I_{\mathrm{sw}}(I_\varepsilon) = |\cos(\pi M_{\mathrm{SQ},\varepsilon} I_\varepsilon / \Phi_0)|$, where typical current values that are applied through the ε-line are of the order of $10\,\mu\mathrm{A} - 100\,\mu\mathrm{A}$.
In Fig. 3.11a the colour-coded switching current distribution as a function of applied ε-current is plotted as it was recorded in the beginning of this thesis. In this case the SQUID's working point for $I_\varepsilon = 0$ is chosen such that $f_{\mathrm{SQ}} \approx 0.25$, i.e. a linear part of the $I_{\mathrm{sw}}(f_{\mathrm{SQ}})$-curve. In this case the switching current dependence as a function of I_ε is also expected to be linear. As this is obviously not the case in Fig. 3.11a means that the switching current is significantly suppressed for increasing $|I_\varepsilon|$. This circumstance made the detection of a qubit step impossible, which mainly obstructed the attempt to implement a working gradiometric qubit in the beginning of this thesis.
Similar effects have been observed in Ref. [90] as well as Ref. [161] and have been analyzed concerning the impact of flux noise and heating influences, with the result that these effects are caused by a temperature dependent increase of the SQUID's switching probability. However, no solutions to that issue are presented.

Heating due to resistive contacts

To identify the disturbing source of the switching current measurements, which was assumed to be heating, the current-voltage characteristic of all flux lines and the temperature dependence on the applied dc-current has been studied in more detail. Figure 3.12a shows the sample stage temperature for two cases as a function of applied ε-current. The one case, where a parabolic dependence of temperature on the ε-current was obtained, describes the situation in the beginning of this thesis. The other case, where a constant temperature $T_{\mathrm{s}} \approx 35\,\mathrm{mK}$ was measured, represents the situation after a solution to that

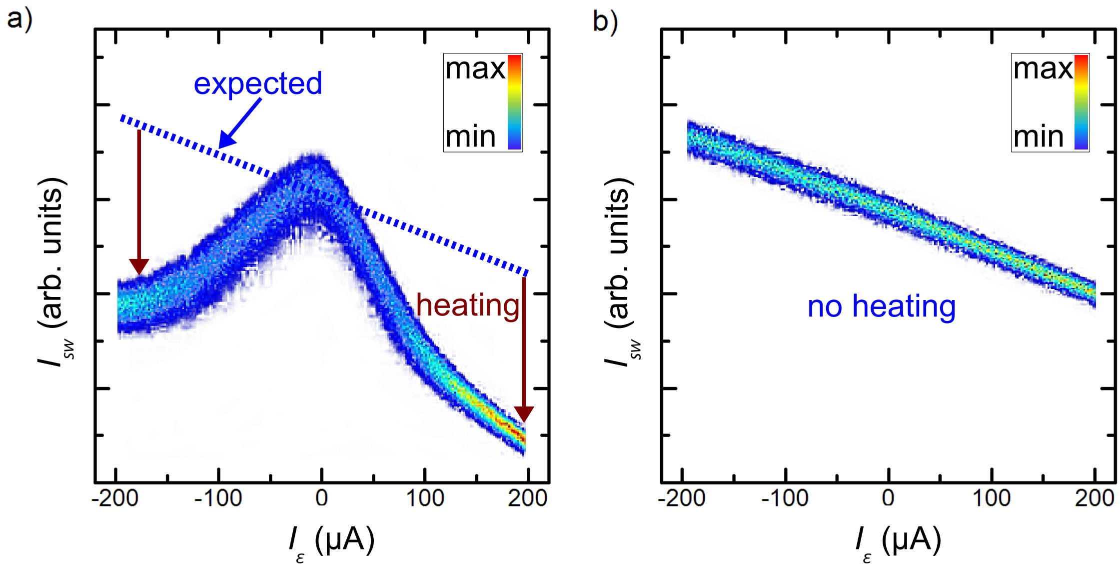

Figure 3.11 – **a)** Colour-coded switching current distribution as a function I_ε recorded on a linear part of the SQUID-curve. Heating by the ε-line suppresses the switching current significantly so that one does not obtain the expected linear behavior. These heating effects are stronger than signals from a qubit such that recording a qubit step is impossible; **b)** Switching current dependence $I_{\mathrm{sw}}(I_\varepsilon)$ recorded on a linear part of the SQUID-curve without heating effects. After the heating issue was solved and the switching current curve followed the expected behavior, it was possible to detect qubit steps.

issue has been found.
Even though the temperature change is only several mK, one can assume the on-chip temperature to be much higher due to the low thermal conductance between sample and thermometer. The steep temperature increase at the beginning of the measurement with parabolic dependence is owed to fact that the ε-current had to be increased to $I_\varepsilon = -200\,\mu\mathrm{A}$ before the start of each measurement but could not kept at this current value until a relaxation of the temperature. This was due to the measurement program, which also does not allow to start at zero current, sweep upwards and then downwards again. Nevertheless, parabolic temperature rise has also been observed for measurements using the α-line This forced the assumption of a general heating due to applying a dc-current through the control lines, leaving open the question where exactly this heat was generated.
The heat generating source could have been either on the sample itself or in the filters and cables that connect the sample stage to the room temperature devices. Comparing the sample stage temperature to the mixing chamber temperature showed that the sample stage heated up stronger and earlier than the mixing chamber after applying an ε-current. This indicates that the heat source must have been located either on the sample itself or on the sample stage. This question was clarified by applying a dc-current between two contact pins of the sample stage as shown in Fig. A.5a. The pins were connected with only a single bond, which caused an even stronger heating than what has been observed for the feed lines.
This result confirmed the assumption that the heating source is the contact-resistance of

the bonds that contact sample and sample stage. As a first consequence the gold pads have been covered with aluminum, which becomes superconducting at milli-Kelvin temperatures and has therefore no resistive energy dissipation. The second, probably more effective change, was the attempt to bond the contact pads as many times as possible to decrease the current flowing through each contact. For the given sample layout 10-15 bonds per contact are possible. An exemplarily sample contacted in this way, which shows no heating effects for currents up to 0.6 mA, is shown in Fig. 3.12c.
A more quantitative analysis of the heating effects can be made by characterizing the of current-voltage characteristic of a single flux line, which is measured as depicted in Fig. 3.12c. Recording an IVC of the flux lines shows primarily a linear, i.e. ohmic, dependence with a resistance R_{lin} of approximately 10 kΩ, owed to the filters of the measurement setup. However, subtracting a linear background of the current-voltage characteristic results in an additional non-linear voltage $\Delta V(I_\varepsilon) = V_{\text{tot}} - V_{\text{lin}}$, which is shown in Fig. 3.12b. This non-linear behavior results in a differential resistance $R_{\text{diff}}(I_\varepsilon) = \partial\Delta V/\partial I_\varepsilon$, as shown in Fig. 3.12d. Fitting a polynomial function $R_{\text{fit}} = \sum_i a_i \cdot I_\varepsilon^i$ to the data yields only significant contributions for $i \geq 3$, i.e. a parabolic dependence similar to the temperature dependence in Fig. 3.12a.
From the result in Fig. 3.12d follows that the additional heat is dissipated due to an additional resistance R_{diff}. The I_ε-dependent heating power can be estimated by $P_{\text{dis}} = \Delta V I_\varepsilon$, which is of the order $P_{\text{dis}} = 10\,\mu$W for $I_\varepsilon = \pm 200\,\mu$A and $R_{\text{diff}} = 500\,\Omega$. This power exceeds the cooling power of the cryostat so that the heat cannot be absorbed, which causes the strongly suppressed switching current shown in Fig. 3.11a.

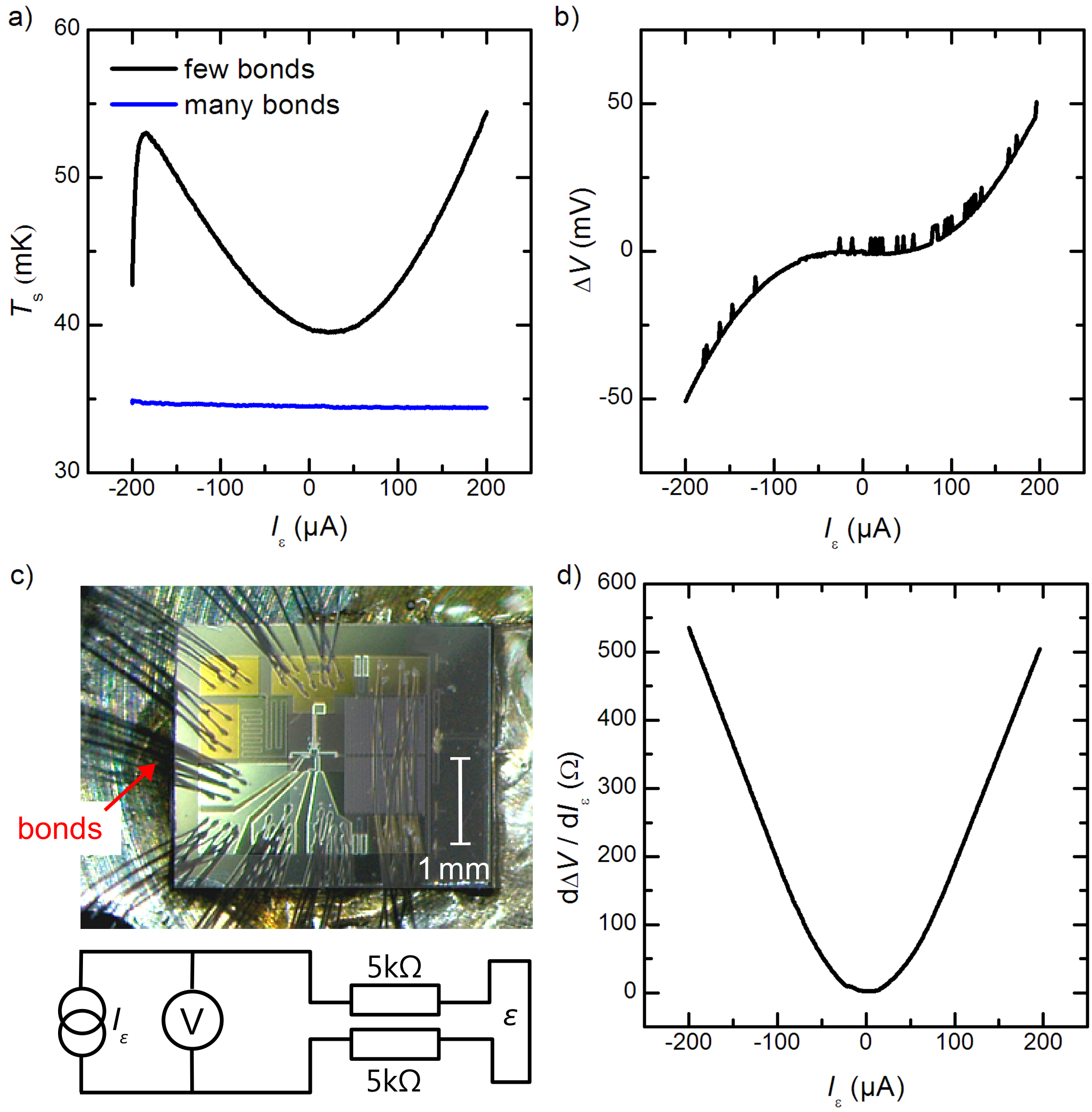

Figure 3.12 – **a)** Sample stage temperature in dependent on I_ε for 2 and 12 bonds connecting the contact pads on the chip and the sample holder (black and blue line, respectively). For ~ 2 bonds the temperature has a I_ε^2-dependence, whereas for ~ 12 bonds the temperature stays constant; **b)** Applying a dc-current to the ε-line results in non-linear change of the voltage drop; **c) Top:** One possible solution to the heating problem is to connect the contact pads with many bonds to the sample holder. A second improvement is to cover the gold contact pads with aluminum that becomes superconducting. This is done only for the ε- and the α-line as can be seen by the four silver-shining pads in the lower left corner of the sample. **Bottom:** Circuit diagram of the experiment. The ε-line is biased with a dc-current I_ε and the voltage drop V over the line is measured. The lines have a resistance of $R_{\mathrm{lin}} \approx 2 \cdot 5\,\mathrm{k}\Omega$; **d)** The additional voltage measured in (c) results in an additional differential resistance $R_{\mathrm{diff}} = \mathrm{d}\Delta V/\mathrm{d}I_\varepsilon$ which is of the order of $100 - 500\,\Omega$. This additional resistance can be related to an additional power dissipation $P_{\mathrm{dis}} = \Delta V \cdot I_\varepsilon$ of the order of several μW.

Chapter

4 Spectroscopy measurements

In this chapter the main experimental results of this thesis are presented, which are microwave spectroscopy measurements on flux qubits. All measurements were performed in a ^{3}He/^{4}He-dilution fridge described in detail in Ref. [150] & Ref. [151] and shown in Fig. A.5. To determine the qubit parameters Δ and ε, a readout technique as described in Sec. 3.2 has been used to perform continuous microwave spectroscopy.
In the first section measurements have been done on two *standard* three Josephson junction flux qubits, where the qubit frustration f_{q} and thus the qubit working point is changed by frustrating the qubit loop with a solenoid. In contrast to that, the working point of the two gradiometric qubits presented in Sec. 4.2 is changed inducing a phase difference $\delta\phi_{\mathrm{q}}$ over the center line. This is achieved using an on-chip control flux line, which couples asymmetrically into the two loops of the gradiometer. In the last section of this chapter the central result of this thesis is presented, which is the successful characterization of a gradiometric flux qubit with tunable tunnel coupling.
Readout was performed for all qubits with an unshunted and underdamped SQUID, as characterized in Sec. 3.1. For all spectroscopy measurements, the flux resolution was in the order of several $\mu\Phi_0$, which allows to record qubit excitations appearing as characteristic peaks and dips with a typical width of approximately 0.1 to 1 mΦ_0.
In contrast to pulsed readout techniques [162], the readout scheme used in this work is not capable of determining the tunnel coupling Δ directly, since the expectation value of the persistent current at the flux degeneracy point of the qubit is zero and therefore no signal is generated. As a consequence no peaks and dips can be recorded in a region of approximately 2 mΦ_0 around the degeneracy point. This is the case for both, *standard* and gradiometric qubits, such that Δ and ε can only be obtained as fit parameters. Even though this is a disadvantage compared to the pulsed readout scheme, it has been possible to characterize several qubits with finite tunnel coupling as well as a tunable gradiometric qubit, for which the minimal transition frequency could be to tuned in the range of several GHz.

4.1 Regular three-Josephson junction flux qubit

In the early stage of this thesis two *standard* three Josephson junction qubits as depicted in Fig. 4.1a have been characterized to verify fabrication parameters and to check whether an adequate tunneling coefficient Δ can be realized. These measurements were also used to verify whether the specific capacitance $\tilde{c}$ determined in Sec. 3.1 can be used to calculate the charging energy E_c, which is necessary for the simulations[1] discussed in Sec. 4.2 & Sec. 4.3.

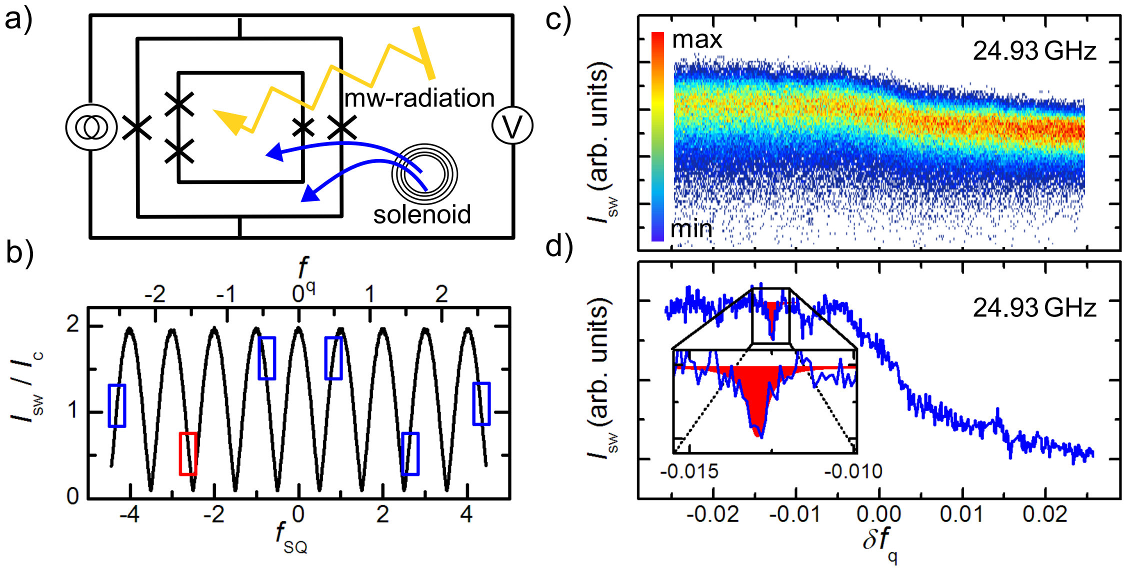

Figure 4.1 – **a)** Readout technique to characterize the non-gradiometric three Josephson junction qubit: The qubit is placed inside the readout-SQUID so that both are frustrated simultaneously by a solenoid: $f_{SQ} = 1.76 f_q$ (blue arrows). In the experiment this solenoid is placed below the sample. The system can be irradiated with electromagnetic waves in the GHz-regime to excite the qubit from its ground to the excited state (yellow zickzack arrow); **b)** SQUID switching current as a function of applied magnetic frustration f_{SQ}. Possible qubit steps are marked with blue rectangles, whereas the red rectangle belongs to the actual position at which all measurements were performed; **c)** Colour-coded switching-current distribution of a SQUID, which is operated as shown in (a): For a frustration around $\delta f_q = 0$ a qubit step is observable; **d)** Taking the mean value of the switching current distribution presented in (c), the qubit step can be recognized more clearly. For irradiation with frequency $\nu_{mw} = 24.93$ GHz, a characteristic peak and dip appears at $\delta f_q \approx \pm 0.011$. The inset shows an enlarged view of the dip that can be analyzed by a Lorentzian fit shown in red to record the δf_q-coordinate.

The measurement principle is shown in Fig. 4.1a. The qubit is placed inside the SQUID such that both frustrations f_q and f_{SQ} can be changed simultaneously by a solenoid. The working point on the SQUID-curve at which qubit steps appear is given by the ratio of SQUID area to qubit area, which is $A_{SQ}/A_q \approx 1.76$. The possible positions for observable qubit steps are shown in Fig. 4.1b. All measurements presented in this section were performed at the same qubit frustration $f_q = -1.5$ (red rectangle), such that the

[1] The simulation program, which uses a full Hamiltonian $\mathcal{H}_{full}$ to calculate the eigenenergies of a qubit for given E_{J0}, E_c and α, was kindly provided by T. Hümmer, *Institut für Physik, Universität Augsburg.*

qubit working point can be defined as $\delta f_\mathrm{q} = f_\mathrm{q} + 1.5$.
An exemplary switching-current distribution around $\delta f_\mathrm{q} = 0$ with applied microwave irradiation of frequency $\nu_\mathrm{mw} = 24.93\,\mathrm{GHz}$ is shown in Fig. 4.1c. Taking the mean value of the colour-coded histograms results in a switching-current curve as shown in Fig. 4.1d. In this graph the qubit step as well as the chracteristic peak and dip appearing due to excitations from ground to excited state are visible more clearly.
The δf_q-coordinates of the peaks and dips are obtained by the center coordinates of Lorentzian fits applied to the excitations as shown in the inset of Fig. 4.1d. These fits been applied to all spectroscopy measurements presented in this thesis to obtain the peak and dip coordinate and could in most cases be applied with a very good accuracy resulting in relative errors for δf_q of less than 1%, which is obtained as the standard deviation of the fitted coordinate.

Qubit parameters

The spectroscopy results for two *standard* three Josephson junction qubits are presented in Fig. 4.2. In (a) the data points $(\delta f_\mathrm{q}, \nu_\mathrm{mw})$ for various frequencies are plotted for a qubit with fixed $\alpha = 0.75$ and in (b) for a qubit which is identically designed but with $\alpha = 0.6$. In the latter case a hyperbolic behavior of the data is observable, which is for flux qubits given by (2.4.10). A two-parameter fit of (2.4.10) applied to the recorded peak and dip positions (black line in Fig. 4.2) yields the qubit parameters Δ/h as the minimal transition frequency and ε/h as the slope for the asymptotic limit $\delta f_\mathrm{q} \gg 0$.

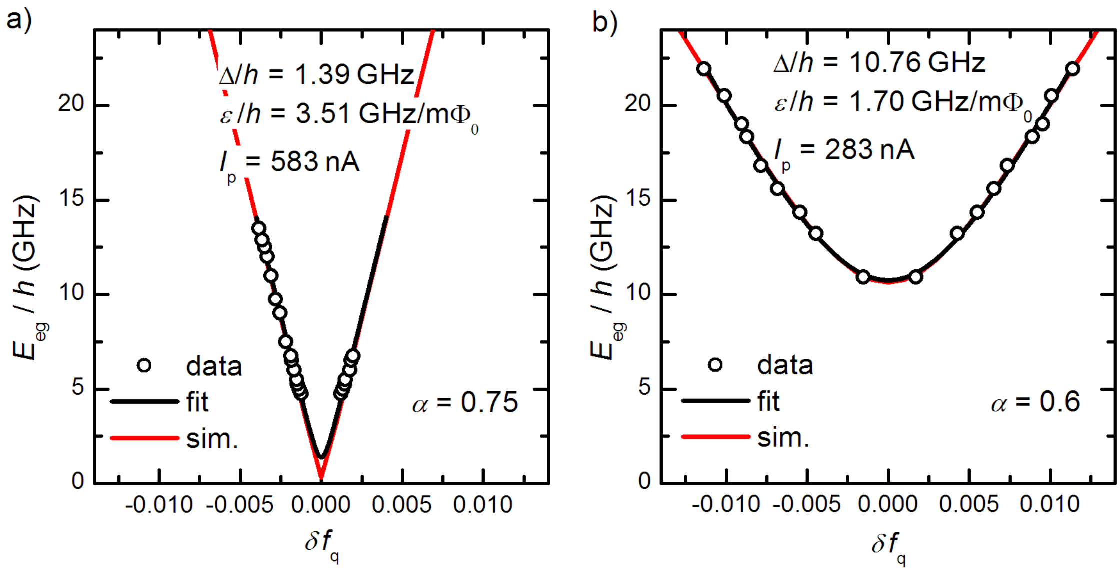

Figure 4.2 – Measured peak and dip coordinates (open circles) distributed around $\delta f_\mathrm{q} = 0$, reproducing the qubit hyperbola $E_\mathrm{eg}(\delta f_\mathrm{q})$ for two qubits with $\alpha = 0.75$ in **a)** and $\alpha = 0.6$ in **b)**. The black lines are two-parameter fits of (2.4.10) to the data points, extracting the minimal transition frequency Δ/h and the asymptotic slope ε/h. The red lines are simulated transition frequencies using a full Hamiltonian $\mathcal{H}_\mathrm{full}$. The results are in very good agreement with theory, which predicts large Δ/h and small ε/h for α closer to 0.5 and vice versa for α closer to 1.

As expected from (2.4.5), the minimal transition frequency $\Delta/h = (1.39 \pm 0.29)\,\mathrm{GHz}$ is smaller for the qubit with larger α, than for the qubit with smaller α, where $\Delta/h = (10.76 \pm 0.14)\,\mathrm{GHz}$. This agrees with the fact that $\varepsilon/h = (3.51 \pm 0.03)\,\mathrm{GHz/m}\Phi_0$ is much higher for $\alpha = 0.75$, than for $\alpha = 0.6$ where $\varepsilon/h = (1.70 \pm 0.01)\,\mathrm{GHz/m}\Phi_0$.
The measured asymptotic slope ε can be used to calculate the persistent current $I_\mathrm{p} = (583 \pm 6)\,\mathrm{nA}$ for $\alpha = 0.75$ and $I_\mathrm{p} = (283 \pm 2)\,\mathrm{nA}$ for $\alpha = 0.6$, using (2.4.9). A calculation using (2.4.4) and I_c^AB of the readout-SQUID can be taken for a consistency check of theses values. In the case of the two qubits one obtains $I_\mathrm{p} = 619\,\mathrm{nA}$ for $\alpha = 0.75$ and $I_\mathrm{p} = 310\,\mathrm{nA}$ for $\alpha = 0.6$, which agrees in both cases with the values for I_p determined by ε. The slightly higher values for I_p from the calculations using (2.4.4) can be explained by the fact that in (2.4.4) the value of I_c^AB was used for I_c, which is an upper limit.

Simulation routine

For future applications of systems containing flux qubits fabricated at the WMI and for the analysis various measurements performed in Sec. 4.2 and Sec. 4.3 it is important to have a reliably working simulation routine that provides qubit transition frequencies for certain parameters. The simulation requires the qubit parameters E_J0, E_c and α to diagonalize the full qubit Hamiltonian $\mathcal{H}_\mathrm{full}$ given by (2.4.7) in order to calculate the eigenergies of the system. The two lowest eigenergies can be used to extract the flux-depending transition frequencies $E_\mathrm{eg}(f_\mathrm{q})/h$. To probe whether the simulation program[1] generates trustworthy results for certain input parameters, the characterization of the two *standard* flux qubits is used.
For all simulations in this thesis the charging energy E_c is calculated using the specific capacitance $\tilde{c} \approx 200\,\mathrm{fF/cm^2}$ determined in Sec. 3.1 and the junction area A_J. The junction area, which is also important to obtain α, was determined by SEM images of comparable samples fabricated on the same wafer. The Josephson coupling energy E_J0 is obtained using the value I_c^AB of the corresponding readout-SQUID, which can be extracted from the SQUID's current-voltage characteristic (cf. 3.1).
Using these parameters to determine E_J0 and E_c yields the simulated transition frequency plotted as a red curve in Fig. 4.2. Here the simulation is shown together with data points and a two-parameter fit for both characterized qubits. Generelly, there is a good agreement in both cases between data and simulation. For the qubit with $\alpha = 0.75$ a deviation between fit and simulation for the value Δ can be observed. This is mostly to the fact that there are no data points very close to $\delta f_\mathrm{q} = 0$, which leads to larger uncertainty and also larger values for Δ. Throughout this thesis it was observed that the fit routine is more complicated for hyperbolas with a relatively small Δ. In these cases the fit yields large error bars and smaller values for the coefficient of determination R^2. This issue has been observed for several measurements presented in Sec. 4.2 & Sec. 4.3, where simulated values for Δ are slightly different than values obtained by a fit.
Nevertheless, the comparison between experiment and simulations confirms the assumptions made for the calculation of E_J0 and E_c and shows that the simulations are well suited to predict a qubit's behavior. Thus the simulation routine presented here is used for all simulations in this thesis.

4.2 Gradiometric qubits

In this section measurements at gradiometric qubits are presented, which were performed to verify the working principle of the gradiometric qubit design. A short introduction to the measurement principle is provided in Sec. 4.2.1. A detailed characterization of the gradiometric qubits is given in Sec. 4.2.2, where the qubit properties are analyzed with respect to their parameters Δ and ε. Furthermore, the quality of the gradiometer, i.e. the insensitivity to an external applied magnetic field is determined in Sec. 4.2.3. The measurements presented in this section provide an important background concerning the gradiometric design, which will in the following section be used to realize a gradiometric flux qubit with tunable tunnel coupling by replacing the α-junction with a SQUID.

4.2.1 Experimental basics

In order to characterize gradiometric qubits, a locally inhomogeneous magnetic field is applied via an on-chip line to change the qubit phase. This is in contrast to the measurements presented before, where a magnetic field was applied by a solenoid to change the frustration of the qubit. The experimental setup used to readout gradiometric qubits is shown in Fig. 4.3a. There is still a solenoid in the experiment, which is placed centered underneath the sample to generate a locally homogeneous field Φ_{hom} (light blue arrows in Fig. 4.3a) in order to change the SQUID's working point. Due to the gradiometric design the qubit working point δf_{q} should not be affected by that. As described above, the qubit can be excited by irradiation in the GHz regime depicted as a yellow zickzack arrow in Fig. 4.3a.
Applying a dc-current to the ε-flux line frustrates the lower loop of the gradiometer stronger than the upper loop, which results in a change of the qubit working point δf_{q}. After trapping an odd number of flux quanta as described in Sec. 3.5, a qubit step is observable while recording the SQUID's switching current as a function of I_ε. This is plotted as a colour-coded switching current distribution in Fig. 4.3b and in Fig. 4.3c the mean value of this switching current distribution is shown, which is used to determine the peak and dip positions as explained in Sec. 4.1.
It should be noted that the strength of the qubit signal recorded by the SQUID, being proportional to MI_{p}, is much lower for the gradiometric design than for the *standard* flux qubit. This is because the gradiometric qubit has to be placed outside the SQUID, so that the mutual inductance M, which is mainly determined by the length of the two close-by lines, is increased. The mutual inductance between trap-loop and qubit can be estimated to be 1/4 compared to the design of the *standard* qubit. This agrees with the measured qubit step height and means that one has to average 16-times more switching events of the SQUID to reach comparable accuracy. Typical measurements with *standard* flux qubits performed in Ref. [150] & Ref. [163] at the WMI averaged typically 300 switching events, which would result in nearly 5000 averaging events for the gradiometric design to achieve comparable accuracy. This large number of averages would exceed the available measuring time by far, so that in most measurements presented in the following the averaging value was restricted to 750. Recording a single spectrum as shown in Fig. 4.3b with an averaging

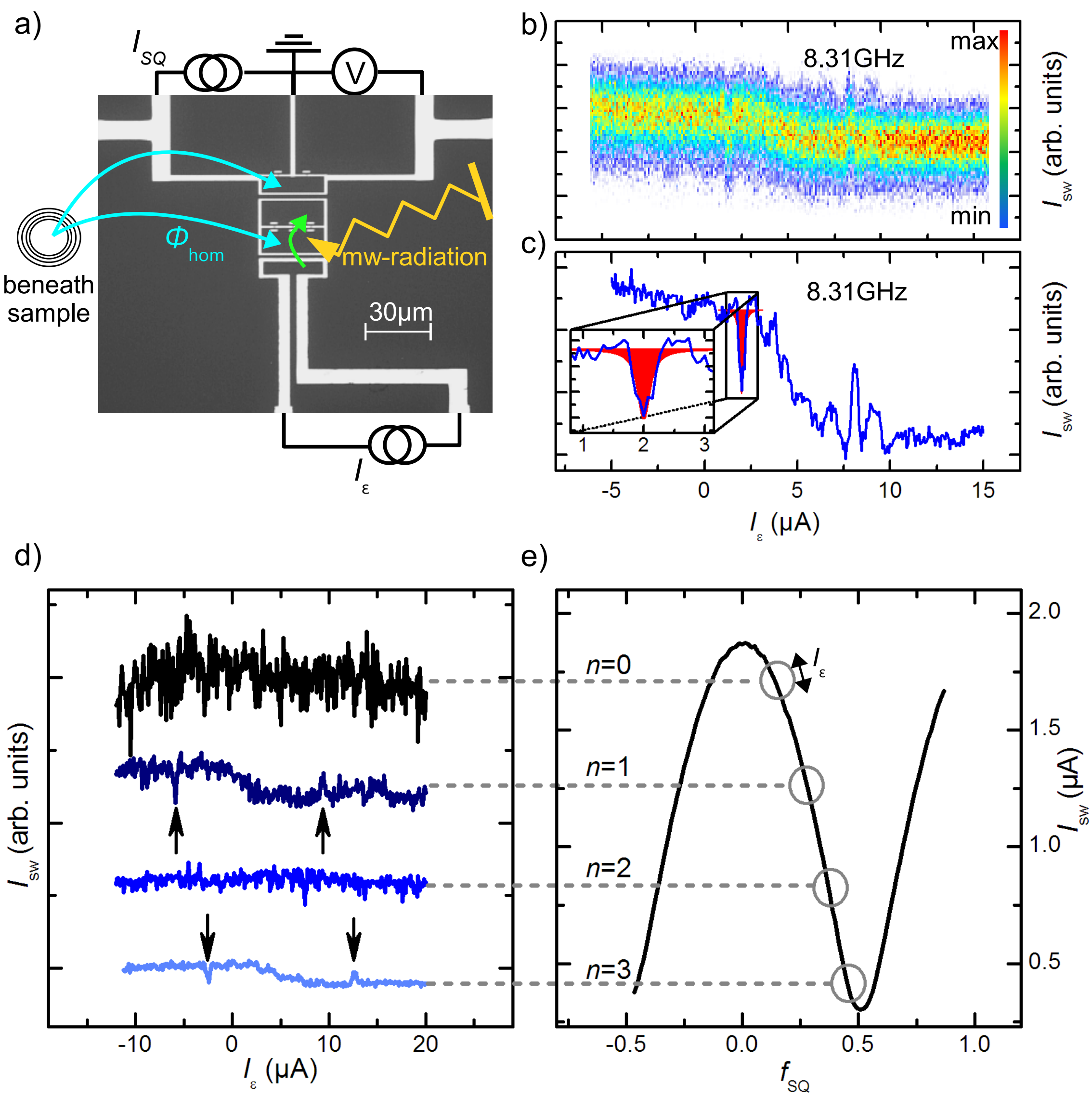

Figure 4.3 – **a)** Measurement setup for the gradiometric qubit displayed as microscope image. The solenoid generates a magnetic field Φ_{hom} that can be assumed to be homogeneous (light blue) since the solenoid is placed centered underneath the sample. The system can be irradiated with electromagnetic waves in the GHz-regime to excite the qubit from its ground to the excited state (yellow zickzack arrow). The qubit working point δf_{q} can be changed by the ε-flux line as explained in Sec. 3.3.1 (pink); **b)** Colour-coded switching-current distribution of a SQUID, which is operated as shown in (a), as a function of applied ε-current for irradiation with frequency $\nu_{\text{mw}} = 8.13\,\text{GHz}$. A qubit step and induced excitations are clearly visible; **c)** Mean value of the current distribution shown in (b). The inset shows a characteristic dip that can be analyzed by a Lorentzian fit; **d)** Switching current recorded for increasing values of trapped fluxoids. A qubit step appears only at odd numbers of n which can be recognized by the appearance of a qubit step with characteristic peaks and dips (cf. black arrows). The SNR improves for working points closer to $f_{\text{SQ}} = 0.5$; **e)** Equivalent SQUID working point for the measurements shown in (d).

value of 750 still lasts approximately 1-2 hours, so that almost one day is required to record a complete qubit hyperbola.

Figure 4.3d is a proof of principle for the gradiometric qubit design, since qubit steps appear only for every odd n. As described in Sec. 3.5, there is already one flux quantum trapped in the loop even if no magnetic field was applied during the transition into the superconducting state. For increasing n, the SQUID's working point changes due to the induced flux, which is proportional to I_{circ} and thus to n. The different SQUID working points have different signal-to-noise ratios (SNR), which can be defined as ratios between excitation height and averaged noise of the spectrum (cf. Fig. 4.3e). This is due to a smaller standard deviation σ_I of the I_{sw}-histograms for points located on a position with larger slope, i.e. closer to a minimum, on the SQUID's switching current curve. At these points the transfer function $H_{\mathrm{t}} = \partial I_{\mathrm{sw}}/\partial f_{\mathrm{SQ}}$ is larger compared to points located at a position closer to a maximum, i.e. with smaller slope. The SNR can be determined using the amplitude h_{fit} of the Lorentzian fit of the peaks and dips, compared to the standard deviation σ_{s} of the averaged switching current in a region far away from these excitations: SNR=$h_{\mathrm{fit}}/\sigma_{\mathrm{s}}$. For the measurements presented in Fig. 4.3d the signal-to-noise ratio is $\mathrm{SNR}_{n=1} = 1.9 \pm 1.0$ and $\mathrm{SNR}_{n=3} = 8.2 \pm 0.7$. As expected from the definition of H_{t}, the measurement close to a minimum, corresponding to $n = 3$, has the highest SNR. This is also the reason that the following measurements were performed at this working point. One big advantage of the gradiometric design is that the SQUID can always be biased by the solenoid at a working point with good SNR since the qubit working point is not affected due to fluxoid quantization in the trap-loop.

From Fig. 4.3c it can be recognized that peaks and dips of each spectrum are not centered with respect to $I_\varepsilon = 0$, as expected for a gradiometric qubit biased at a phase π. This indicates that the fabricated gradiometer used for these measurements is not perfectly gradiometric. This will be analyzed in more detail in Sec. 4.2.3 after a calibration of the ε-flux line was performed in Sec. 4.2.2.

4.2.2 Qubit parameters

Recording qubit steps with the gradiometric design for various mw-frequencies results in a qubit hyperbola E_{eg} as a function of applied ε-current I_ε, which is shown in Fig. 4.4 top row. A two-parameter fit (gray curve in Fig. 4.4) can extract the minimal transition frequency Δ/h but the asymptotic slope is obtained as a function of applied ε-current ($\eta(I_\varepsilon)$) and not of applied frustration ($\varepsilon(\delta f_{\mathrm{q}})$) as desired in (2.4.10) (cf. green line in Fig. 4.4b). This requires a technique to scale the ε-line in a way that transforms η to ε. This transformation is achieved by a scaling factor $x = \partial\delta f_{\mathrm{q}}/\partial I_\varepsilon$, which is assumed to be constant.

The factor x is extracted from comparing the two-parameter fit to simulated qubit transition frequencies $E_{\mathrm{eg}}(\delta f_{\mathrm{q}})/h$, which are simulated as described in Sec. 4.1. For exact simulations and after shifting the recorded qubit steps in I_ε-direction to be symmetric with respect to $I_\varepsilon = 0$, the I_ε-axis can be scaled in a way that

$$\varepsilon(\delta f_{\mathrm{q}}) \stackrel{!}{=} x \cdot \eta(I_\varepsilon). \tag{4.2.1}$$

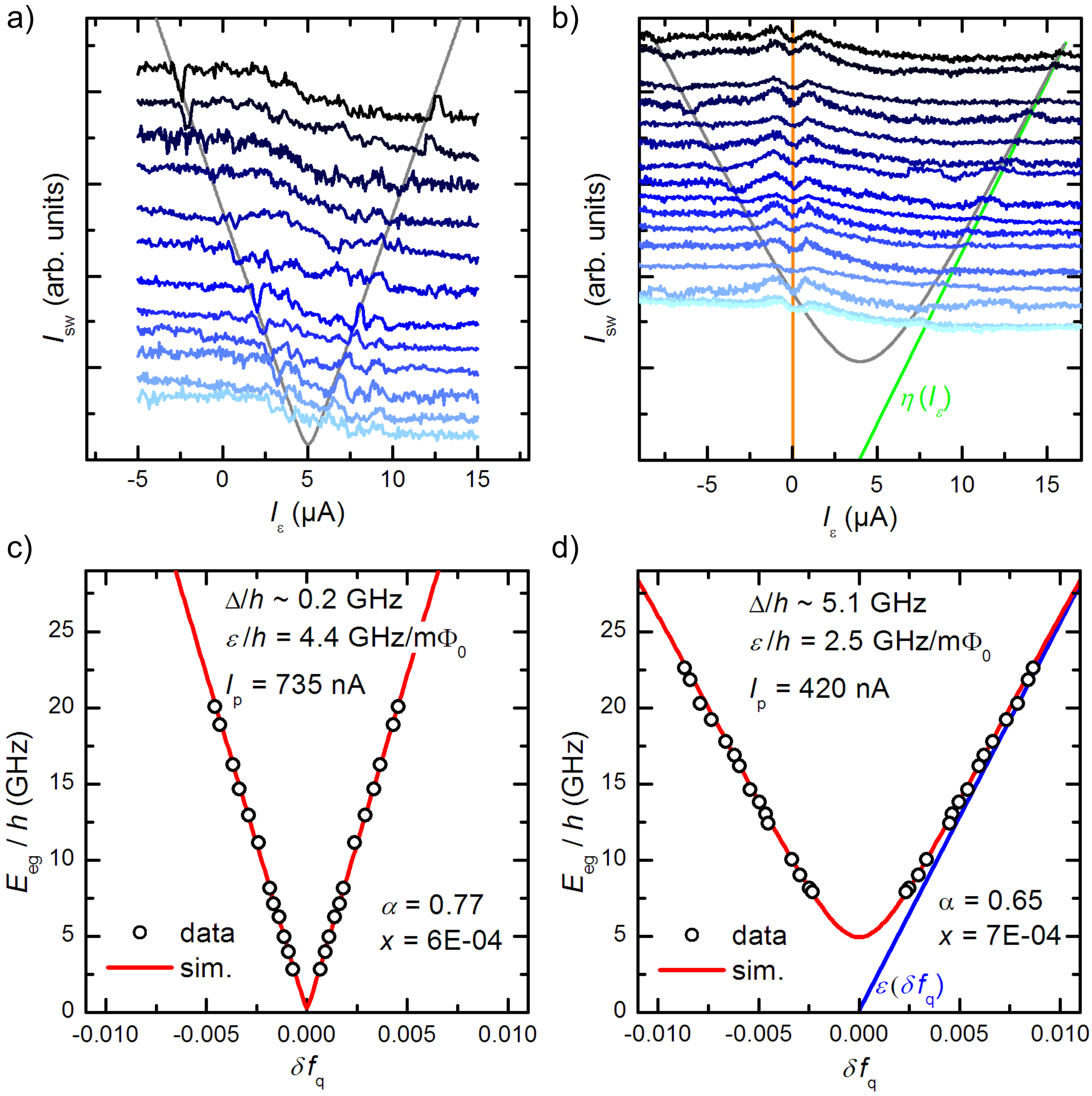

Figure 4.4 – **Top row:** Qubit steps recorded for two gradiometric qubits with $\alpha = 0.77$ (a) and $\alpha = 0.65$ (b), which are shifted for clarity in y-direction proportional to the irradiated microwave frequency ν_{mw}. The peaks and dips result in a qubit hyperbola shown as a gray line which gives Δ/h and $\varepsilon(I_\varepsilon)/h$ as a fit parameter. For a complete description of the qubit behavior this fit has to be adjusted to a δf_{q}-axis as in (c), (d). The qubit signal in (a) is much stronger than in (b) since it is proportional to I_{p} and thus to $\sqrt{1-\frac{1}{2\alpha}^2}$. From these measurements the asymptotic slope is obtained as $\eta(I_\varepsilon)$ (green line in (b)). There is a frequency-independent excitation at $I_\varepsilon \approx 0$ (orange line in b), which is probably due to resonances in the control circuits; **Bottom row:** Recorded peak and dip positions and simulated transition frequency as a function of δf_{q}, which is calibrated with respect to I_ε using the scaling parameter x (cf. text for further details). In this calibrated system the asymptotic slope is obtained as $\varepsilon(\delta f_{\mathrm{q}})$ (blue line in (d)). The qubit in (c) has a negligible tunnel coupling, whereas the qubit in (d) has a finite tunnel coupling $\Delta/h \approx 5.1\,\mathrm{GHz}$.

The result of simulation and measured data with adapted δf_q-axis is shown in Fig. 4.4, bottom row. The simulated values are $\varepsilon/h = 4.4\,\mathrm{GHz/m\Phi_0}$ for $\alpha = 0.77$ and $\varepsilon/h = 2.5\,\mathrm{GHz/m\Phi_0}$ for $\alpha = 0.65$. In both cases the simulated transition frequencies are in very good agreement with the data, showing that a reliable value for $\varepsilon(\delta f_\mathrm{q})$ was extracted. This is confirmed by fact that $\varepsilon(\delta f_\mathrm{q})$ is on the same order as ε-values measured with *standard* qubits in Sec. 4.1 and shows that this technique to calibrate the flux scale is trustworthy. A quantitative test of $\varepsilon(\delta f_\mathrm{q})$ can be performed by using (2.4.4) and (2.4.9) to calculate

$$\varepsilon = 2\Phi_0 I_\mathrm{c}^\mathrm{AB} \cdot \sqrt{1 - \left(\frac{1}{2\alpha}\right)^2}, \tag{4.2.2}$$

which yields $\varepsilon/h = 4.6\,\mathrm{GHz/m\Phi_0}$ for $\alpha = 0.77$ and $\varepsilon/h = 2.9\,\mathrm{GHz/m\Phi_0}$ for $\alpha = 0.65$. These values are slightly higher than the simulated ones, which could be due to the fact that for the calculations I_c^AB and thus a theoretical upper limit for I_c was used. Nevertheless, there is a remarkably good agreement between calculation and simulation considering that E_J0 and E_c were only estimated from the SQUID IVC and considering the assumption that δf_q changes linear with I_ε.
Concerning the value Δ/h, the two gradiometric qubits show qualitatively equal behavior as the *standard* flux qubits characterized in Sec. 4.1, which can be seen by a small Δ for larger α and vice versa. The simulated value for Δ/h is approximately 0.2 GHz for $\alpha = 0.77$ and the actual measured value is negligibly small on a GHz scale. For $\alpha = 0.65$ simulation and experiment are in very good agreement which is $\Delta/h \approx 5\,\mathrm{GHz}$.
Generally, switching-current measurements can also be used to quantify the qubit dynamics, e.g. decay rates and Rabi oscillations [164], by analyzing the resonance peaks and dips in more detail [165]. This requires however a data quality that allows a reproducible recording of the peak width and height, which is not given for the measurements performed with this experimental setup. Nevertheless, a rough estimate of the decay rate τ_q can be made in the regime $|\delta f_\mathrm{q}| \gg 0$, where the decay is dominated by dephasing ($\tau_\mathrm{q} \approx \tau_\phi$) [162]. In this case the qubit lifetime $T_\mathrm{q} = 1/\tau_\mathrm{q} \approx T_\phi$ is determined by the inverse of the resonance width w, which is the **f**ull **w**idth at **h**alf **m**aximum (FWHM) of peak or dip [56]:

$$T_\phi = \frac{2h}{w \cdot \varepsilon}. \tag{4.2.3}$$

Using a Lorentzian fit with linear background gives lifetimes in the order of $T_\phi \approx 1$ - 5 ns for both gradiometric qubits, which is a plausible range [56, 91, 129, 152, 154, 165].

4.2.3 Gradiometer quality

A perfect gradiometer should be insensitive to homogeneous magnetic fields. However, the fact that the $I_\mathrm{sw}(I_\varepsilon)$-curves are not symmetric to $I_\varepsilon = 0$, and that the qubit step is shifted for different n as shown in Fig. 4.5, is an indicator that the gradiometer is not perfectly fabricated. In reality there are unavoidable imperfections, which can result from imprecise fabrication steps or from intrinsic disturbances such as impurities.
Such imperfections obstruct the assumption that each of the two gradiometer loops is frus-

trated equally ($f_1 = f_2$) for applied homogeneous magnetic fields. Strictly, the difference between the frustration of each loop has to be calculated, which yields

$$\delta f_{12} = \frac{\delta\Phi_{12}}{\Phi_0} = \frac{1}{\Phi_0}\iint_{A_1} B_\perp(\mathbf{r})\cdot \mathrm{d}A - \frac{1}{\Phi_0}\iint_{A_2} B_\perp(\mathbf{r})\cdot \mathrm{d}A, \tag{4.2.4}$$

where $B_\perp(\mathbf{r})$ is the space-depending component of the flux density $\mathbf{B}$ perpendicular to the trap-loop area, which is not necessarily homogeneous. On the other hand there can also be a difference in the area of the two half squares $\delta A_{12} = (A_1 - A_2)$, which can be used to approximate (4.2.4) to

$$\delta f_{12} \approx f_{\mathrm{tr}}\left(\frac{\delta A_{12}}{A_{\mathrm{tr}}} + \frac{\delta B_{12}}{B_{\mathrm{tr}}}\right). \tag{4.2.5}$$

Here δB_{12} is the difference between the field density averaged over area A_1 and the field density averaged over area A_2, whereas B_{tr} is the field density averaged over the whole trap-loop. In addition to imperfections in size and magnetic field, there can be also a difference in the overall inductance

$$\delta L = (L_{\mathrm{k},1} - L_{\mathrm{k},2}) + (L_{\mathrm{g},1} - L_{\mathrm{g},2}) = \delta L_{\mathrm{k}} + \delta L_{\mathrm{g}} \tag{4.2.6}$$

of the loop, which could be caused by grains, impurities or deviations in the cross sectional area of the aluminum layers.
Using the circulating current of (3.5.1), the phase difference $\delta\phi_{\mathrm{q,im}}$ between the endpoints of the center line is given as

$$\begin{aligned}\delta\phi_{\mathrm{q,im}} &= 2\pi\delta f_{1,2} + 2\pi(n - f_{\mathrm{tr}})\frac{\delta L_{\mathrm{k}} + \delta L_{\mathrm{g}}}{L_{\mathrm{k}} + L_{\mathrm{g}}}\\ &= 2\pi f_{\mathrm{tr}}\underbrace{\left(\frac{\delta A_{12}}{A_{\mathrm{tr}}} + \frac{\delta\ B_{12}}{B_{\mathrm{tr}}} - \frac{\delta L_{\mathrm{k}} + \delta L_{\mathrm{g}}}{L_{\mathrm{k}} + L_{\mathrm{g}}}\right)}_{\equiv 1/Q_{\mathrm{grad}}(f_{\mathrm{tr}})} + 2\pi n\underbrace{\frac{\delta L_{\mathrm{k}} + \delta L_{\mathrm{g}}}{L_{\mathrm{k}} + L_{\mathrm{g}}}}_{\equiv 1/Q_{\mathrm{grad}}(n)}.\end{aligned} \tag{4.2.7}$$

Analogously to other physical systems [166], a quality factor of a gradiometer $Q_{\mathrm{tot}} = Q_{\mathrm{grad}}(f_{\mathrm{tr}}) + Q_{\mathrm{grad}}(n)$ can be defined, where the f_{tr}- and n-depending parts are defined in (4.2.7). Equation (4.2.7) implies that due to a finite Q_{tot} qubits steps are shifted in I_ε-direction proportional to the applied trap-loop frustration and stepwise for increasing odd values of n.
To analyze the quality of a gradiometer, qubit steps for different amounts of trapped fluxoids n, as well as for different applied frustration f_{tr} are recorded to extract $Q_{\mathrm{grad}}(n)$ and $Q_{\mathrm{grad}}(f_{\mathrm{tr}})$, respectively. The position of each qubit step can be defined as the center coordinate between peak and dip, which will be induced by irradiation with constant frequency. The result of measurements performed in this way is shown in Fig. 4.5, where in (a) the number of trapped fluxoids n is varied and in (b) the frustration f_{tr} is changed and for both the irradiated mw-frequency was $\nu_{\mathrm{mw}} = 19.33\,\mathrm{GHz}$.
The quality factors are calculated to $Q_{\mathrm{grad}}(n) = 943 \pm 19$ and $Q_{\mathrm{grad}}(f_{\mathrm{tr}}) = 1076 \pm 16$. In

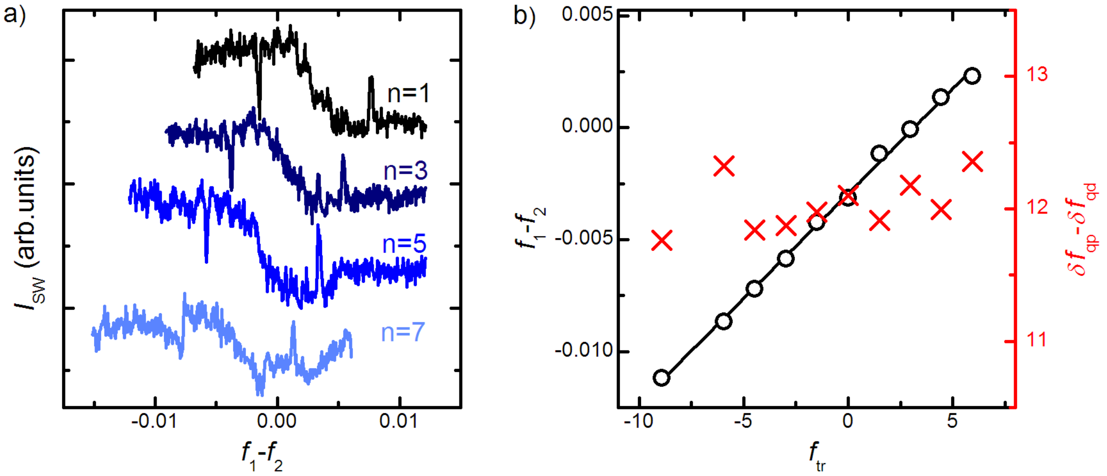

Figure 4.5 – **a)** Displacement of the qubit step for increasing number n of trapped flux quanta. The gradiometer quality using this data is approximately $Q_{\mathrm{grad}}(n) \approx 1000$; **b)** Black circles: Displacement of the qubit step due to increasing frustration which yields $Q_{\mathrm{grad}}(f_{\mathrm{tr}})$) calculated from a linear fit (black line). The red crosses represent the peak-dip distance which is almost constant for all f_{q}-data. This shows that the qubit potential is unaffected by homogeneous external frustrations.

other words the qubit working point is shifted approximately $1\,\mathrm{m}\Phi_0$ per applied Φ_0, or the relative error is approximately $1 \cdot 10^{-3}$.

As all samples are fabricated by electron beam lithography, capable of defining structures with an accuracy of $\delta w = 20\,\mathrm{nm}$ [167], an uncertainty of $0.4\mu\mathrm{m}^2$ is evaluated for $A_1 - A_2$, or $\delta A_{12}/A_{\mathrm{tr}} \approx 5 \cdot 10^{-3}$. The uncertainty of total inductance is hard to estimate since parameters as the actual shape of the two halves or the difference in the cross sectional area of the aluminum layers are hard to determine. However, a rough estimation of the uncertainty of kinetic inductance can be made, using an accuracy of $\delta w = 20\,\mathrm{nm}$ in lateral direction and $\delta h = 2.5\,\mathrm{nm}$ in the layer thickness [168] for a cross section of $(506 \cdot 90)\,\mathrm{nm}^2$. With these estimations the calculated error for the kinetic inductance is approximately $0.2\,\mathrm{pH}$ or $\delta L_{\mathrm{k}}/L_{\mathrm{k}} \approx 6 \cdot 10^{-3}$. As both estimated errors result in lower quality factors than the actual measured, it can be assumed that the quality factor of the gradiometer is already close to its optimum. It should be noted that finite uncertainties in (4.2.7) could either balance each other or sum up so that a quantitative description is in any case difficult to perform.

Nevertheless, it is important that the measured quality factor is higher than quality factors obtained by estimations for δA_{12} and δL_{k} since there is a limiting lower bound. This lower bound is given by the fact that the qubit step must be reachable, i.e. should not be shifted too much using the ε-line, without running into heating problems as described in Sec. 3.6. Since the ε-line can change the qubit working point by approximately $1\,\mathrm{m}\Phi_0/\mu\mathrm{A}$, the quality factor has to be of the order of 1000 to operate the qubit without being limited in the applied external frustration. A second reason requesting even higher quality factors is the time consuming prospection of a shifted qubit steps, which would be easier if the step position stays constant.

An important fact is that the peak to dip distance $\delta f_{\mathrm{qp}} - \delta f_{\mathrm{qd}}$ is not affected by external frustration, even when changing the trap-loop frustration by more than $15\,\Phi_0$ as shown in Fig. 4.5b. This shows that the qubit potential is unaffected by homogeneous magnetic flux. Flux insensitivity is a major advantage of the gradiometric qubit design compared to the *standard* flux qubit design being highly sensitive to external applied flux. The parameter magnetic flux stays therefore free to control other flux-sensitive systems placed on the sample.

The central result of the measurements presented in this section is that a reliably working gradiometric qubit design was succesfully implemented, which can be used to bias a flux qubit at its degeneracy point. The fact that the qubit working point stays unaffected by homogeneous magnetic fields, allows to integrate gradiometric qubits into a large scale system, where several qubits can be operated and read out simultaneously without affecting each other. It was also confirmed that different α-values result in different tunnel couplings, which will be realized in the following section at a single qubit using an α-SQUID instead of a single junction.

4.3 Tuning the tunnel coupling of a gradiometric flux qubit

In this section the main result of this thesis is presented, which is the successful characterization of a gradiometric flux qubit with tunable tunnel coupling. The characterization of a tunable qubit integrated into a gradiometric design is more advanced than the experiments on flux qubits presented in the sections before. This is because two prerequisites have to be fulfilled to observe a qubit step: On the hand the number of trapped flux quanta must be odd, and on the other hand the value of α must be larger than 0.5. Unfortunately, an estimation of the actual value of α is difficult, since α depends on many variables as for example the number of n, the applied frustration to the trap-loop f_{tr}, the inductance ratio β or the background field B_{b} discussed in Sec. 3.5.
After providing some experimental background in Sec. 4.3.1, the characterization of the tunable qubit will be used to extract the characteristic energies E_{J0} and E_{c}, which are crucial for the qubit properties Δ and ε. To determine the characteristic energies, it is first of all necessary to determine the flux dependency of α, which will be discussed in Sec. 4.3.2. This dependency can be used to obtain the characteristic energies E_{J0} and E_{c} in two ways: First, a solenoid is used to tune α, which allows to define the dependency between Δ and α, which can be used to extract E_{J0} and E_{c} from fit parameters (cf. Sec. 4.3.3). A second approach discussed in Sec. 4.3.4 uses an on-chip line placed close to the qubit to tune α, which also yields E_{J0} and E_{c} from fit parameters. Both methods are compared to a simulation in Sec. 4.3.5, which is based on an independent method to determine E_{J0} and E_{c}. This simulation is also used to draw a general comparison between the tunnel gap of various qubits fabricated at the WMI. The chapter finishes with an overview of optimization techniques that can be applied to future qubits in order to improve readout quality, which was a limiting factor during many measurements presented in this section.

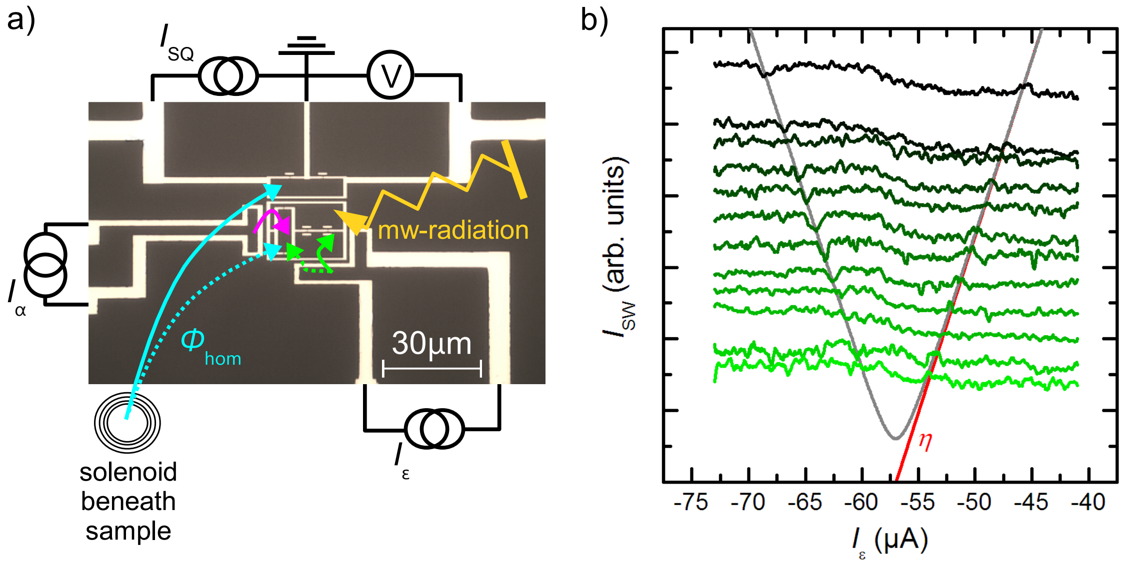

Figure 4.6 – **a)** Microscope image of the experimental setup to readout a gradiometric qubit with tunable tunnel coupling: In principle the system works as the gradiometric design explained in Sec. 4.2 with the difference that the α-junction is replaced by a SQUID. As a consequence, changing the SQUID working point with Φ_{hom} always also induces a change of f_α (light blue). This change of f_α can also be induced by a current I_α through the α-flux line; **b)** Typical set of qubit steps recorded with the tunable qubit, which are shifted for clarity in y-direction proportional to the frequency ν_{mw} of applied irradiation. The spectra are measured in an uncalibrated system resulting in a qubit hyperbola as a function of ε-current. The gray curve is a two-parameter fit to the data, which yields the minimal transition frequency Δ/h and the asymptotic slope η in the uncalibrated system (red line).

4.3.1 Experimental basics

The experimental setup to readout a gradiometric qubit with tunable tunnel coupling is shown in Fig. 4.6a. The readout technique is in principle the same as in Sec. 4.2 with the difference that the α-junction is replaced by a SQUID and one flux line is added to change the frustration of this SQUID.

Even though both gradiometric qubits presented in Sec. 4.2 have been characterized before the tunable qubit presented in this section, there have been many uncertainties concerning the behavior of this design in the beginning of the measurements. In the first place the routine to determine the exact amount of trapped flux quanta and the strength of the background field B_{b} presented in Sec. 3.5 was not derived yet. Therefore it could not be predicted whether a qubit step is expected at a certain n, or not. The tunable qubit presented in this section is designed such that $\alpha_0 = 1.05$, $A_\alpha/A_{\mathrm{tr}} = 0.18$ and $\beta \approx 0.8$ as it was determined in Sec. 3.4. With these parameters the first two α-values that are larger than 0.5, i.e. possible working points of the qubit, are calculated to $\alpha(n = \pm 1) \approx 0.97$ and $\alpha(n = \pm 3) \approx 0.73$ (cf. (3.3.8)).

In the beginning of the measurements the detection of a qubit step was complicated since a possible cross correlation between the actual frustration $f_{\alpha,\mathrm{act}}$ of the α-SQUID and the flux induced by the ε-line necessary for readout was not known. For an undesirable

large mutual inductance between ε-line and α-SQUID (green dashed arrow in Fig. 4.6a) the qubit potential will change during readout so that a qubit step can be suppressed or the transition frequencies will not strictly follow the qubit hyperbola anymore [21]. As it turned out later, this effect is not observed for the design presented here, so that the inductance between ε-line and α-SQUID is neglected in the following.
As explained in detail in Sec. 3.3.2, the tunnel coupling Δ can be tuned either via the on-chip α-line (pink arrow in Fig. 4.6a) or via a homogeneous field Φ_{hom} (light blue arrow in Fig. 4.6a). In the latter case the unavoidable situation is given that the frustration of the readout-SQUID also changes with Φ_{hom} (light blue arrows in Fig. 4.6a). To sustain a sufficient readout quality, possible working points to bias the α-SQUID are restricted to points where the readout-SQUID is close to a minimum (cf. SNR calculations in Sec. 4.2).
A successful tuning of the tunnel coupling Δ can be detected by comparing the minimal transition frequency of qubit hyperbolas recorded for different $f_{\alpha,\text{act}}$. During the eight weeks that the measurements presented in this section have taken, corresponding to approximately 250 million recorded switching events of the readout-SQUID, almost twenty qubit hyperbolas and an uncounted number of calibration measurements have been recorded.

4.3.2 The flux dependent α-value

To obtain a quantitative description of the tunable qubit, the value α must be well defined, or more strictly speaking, the dependency between external applied frustration to the trap-loop and the resulting α-value $\alpha(f_{\text{tr}})$ must be known. Since neither the value $\alpha(f_{\text{tr}} = 0)$ nor the change of α with respect to f_{tr} is ab initio given for a tunable qubit, the varying asymptotic slopes of different qubit hyperbolas will be used in order to determine $\alpha(f_{\text{tr}})$.
In the rest of this section it will be discussed how the value of α as function of applied magnetic field, or rather of applied current through the solenoid, is determined:
The asymptotic slope ε of different qubit hyperbolas depends on I_{p}, which is again a function of α as given in (2.4.4). Since for a tunable qubit α itself is further depending on the frustration $f_{\alpha,\text{act}}$ of the α-SQUID, the asymptotic slope is given as

$$\varepsilon(f_{\alpha,\text{act}}) = 2\Phi_0 I_{\text{p}}(f_{\alpha,\text{act}}) = 2\Phi_0 \cdot I_{\text{c}} \cdot \sqrt{1 - \left(\frac{1}{2\alpha(f_{\alpha,\text{act}})}\right)^2}. \tag{4.3.1}$$

Using (3.3.8) one can rewrite (4.3.1) to

$$\varepsilon(f_{\alpha,\text{act}}) = 2\Phi_0 I_{\text{c}} \cdot \sqrt{1 - \left(2\,\underbrace{\alpha_0 \left|\cos\left(\pi\frac{A_\alpha}{A_{\text{tr}}}\left[\frac{1}{1+\beta}f_{\text{tr}} + \frac{\beta}{1+\beta}n\right]\right)\right|}_{\alpha(f_{\alpha,\text{act}})}\right)^{-2}}. \tag{4.3.2}$$

From this it can be followed that qubit hyperbolas for different values of f_{tr} but constant n have varying ε-values showing a highly non-linear behavior defined by (4.3.2).
The idea to extract α from measured ε-values is to apply a fit of (4.3.2) to the data and

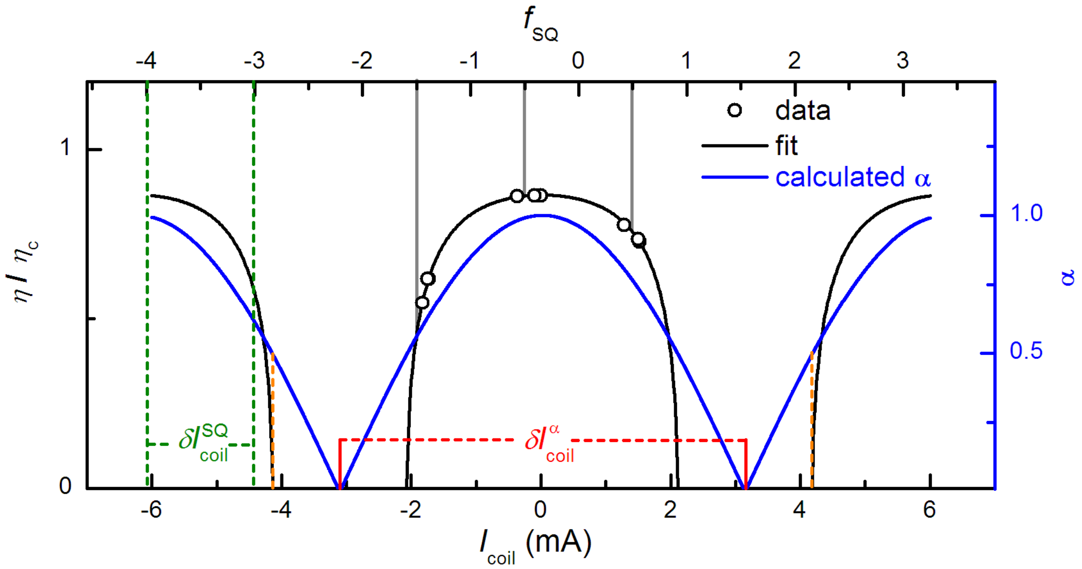

Figure 4.7 – Measured values η (black circles) corresponding to the asymptotic slope of qubit hyperbolas in the uncalibrated system plotted as a function of applied coil-current I_{coil}. The data points are clustered around certain values of I_{coil}, which correspond to a SQUID working point f_{SQ} close to a minimum (gray lines), which were chosen to have a sufficient readout quality. There is a remarkably good agreement between fit (black line) and data, which shows the ability to tune the α-value with a high precision. The blue curve represents the calculated α-value, which is periodic in I_{coil}, resulting in alternating regimes where the qubit is working ($\alpha(I_{\text{coil}}) > 0.5$) intersected by regimes where the qubit is not working ($\alpha(I_{\text{coil}}) < 0.5$). The current values used to calculate β corresponding to $\delta f_\alpha = 1$ and $\delta f_{\text{SQ}} = 1$ are marked in red and green, respectively.

then calculate α using the extracted fit parameters. In principle (4.3.2) can be used for the fit, using values for A_α, A_{tr} and β as well as f_{tr} as a fit parameter. Since A_α and A_{tr} can be only estimated from SEM images and β is only an estimation from phase-biased SQUID measurements in Sec. 3.4, a current to flux transfer function

$$H_{\alpha c} = \frac{\partial f_{\alpha,\text{act}}}{\partial I_{\text{coil}}} = \frac{A_\alpha}{A_{\text{tr}}} \frac{1}{1+\beta} \frac{\partial f_{\text{tr}}}{\partial I_{\text{coil}}}, \tag{4.3.3}$$

which is assumed to be constant, will be used as a fit parameter in (4.3.2). Furthermore $I_0 = \beta n/(1+\beta)$ is used as a fit parameter, since neither n nor β changes in the experiment. This leads to a fit function

$$\eta(I_{\text{coil}}) = \eta_{\text{c}} \cdot \sqrt{1 - \{2\,|\cos(\pi H_{\alpha c} \cdot (I_{\text{coil}} - I_0))|\}^{-2}}, \tag{4.3.4}$$

where $\alpha_0 = 1$ was approximated. It should be noted that in (4.3.4) $\eta(I_{\text{coil}})$ is obtained and not $\varepsilon(f_{\alpha,\text{act}})$ as in (4.3.2). This change is required since the asymptotic slopes are measured in the uncalibrated system, where qubit hyperbolas are recorded as a function of I_ε and not as a function of δf_{q} (cf. Fig. 4.6b). Since $\eta(I_\varepsilon)$ is quantitatively not equal to $\varepsilon(f_{\alpha,\text{act}})$, the factor $2\Phi_0 I_{\text{c}}$ is replaced by the fit parameter η_{c} in (4.3.4).

However, to define a relation $\alpha(f_{\alpha,\mathrm{act}})$ it is not required to know the actual value of $\varepsilon(f_{\alpha,\mathrm{act}})$ but only the change of ε with respect to $f_{\alpha,\mathrm{act}}$. Therefore it is sufficient to know the value of the transfer function $H_{\alpha\mathrm{c}}$ and the initial displacement I_0 for a definition of $\alpha(f_{\alpha,\mathrm{act}})$. The measured values for η and a fit of (4.3.4) to the data is shown in Fig. 4.7 (black dots and black line, respectively). For all calculations of α performed in this section the fit parameters $H_{\alpha\mathrm{c}} = 0.16\,\mathrm{mA}^{-1}$ and $I_0 = 20\,\mu\mathrm{A}$ were used to calculate

$$\alpha = \alpha_0 \left|\cos\left(\pi H_{\alpha\mathrm{c}} \cdot (I_{\mathrm{coil}} - I_0)\right)\right| . \tag{4.3.5}$$

There is a remarkable agreement between data and fit, resulting in an error of 0.6% for $H_{\alpha\mathrm{c}}$ and 0.01% for I_0, which means that the α-value can be tuned with a very high precision. The data points are clustered around certain values of I_{coil}, which correspond to a SQUID working point f_{SQ} close to a minimum of the switching current curve. This working points are chosen to have a sufficient readout quality (gray lines in Fig. 4.7). Thus, possible SQUID working points to read out the qubit are located on both sides of each minimum of the switching current curve (cf. data points near $f_{\mathrm{SQ}} = \pm 0.5$). However, it was not possible to detect a qubit step on both sides of the minimum at $f_{\mathrm{SQ}} = -1.5$ because the α-value, and thus I_{p}, has been too small for $f_{\mathrm{SQ}} < -1.5$ even though α was still larger than 0.5.
Equation (4.3.4) is only well defined for $|\cos(\pi H_{\alpha\mathrm{c}} \cdot (I_{\mathrm{coil}} - I_0))| > 0.5$, i.e. $\alpha(f_{\alpha,\mathrm{act}}) > 0.5$. This results in periodically appearing regimes where $\eta(I_{\mathrm{coil}})$ has finite values and qubit steps occur, intersected by regimes where $\eta(I_{\mathrm{coil}})$ is not well defined and thus no qubit steps occur. For the qubit potential this means that the point where $\eta(I_{\mathrm{coil}})$ vanishes is the point where the potential changes from a double to a single well potential and the persistent current vanishes. In Fig. 4.7 the fit curve for $\eta(I_{\mathrm{coil}})$ is plotted in a way that the periodic behavior can be recognized. For clarity, the calculated value for α is also shown as a blue curve in Fig. 4.7.
Using the solenoid, one can reach the regime where α becomes larger than 0.5 again and a qubit step recurs, cf. dashed orange lines in Fig. 4.7. However, this has not been tried in the experiment since qubit steps were shifted too strongly on the I_ε-axis for large coil currents and thus not detectable anymore. This could be due to a small quality factor Q_{tot} of the tunable qubit, which is a matter of improvement in future designs if that regime wants to be reached.

Nevertheless, the data presented in Fig, 4.7 shows in a formidable way that the α-value of a gradiometric qubit was tuned in a controlled way over a significant range. This will be used in the following sections to extract the crucial parameters E_{J0} and E_{c} from spectroscopy measurements.

4.3.3 Tuning Δ via the solenoid

In this section the successful realization of a qubit with tunable tunnel coupling is presented, which is used to determine the characteristic energies E_{J0} and E_{c}. To evaluate the tunnel coupling for different values of α, two-parameter fits have been performed to extract Δ/h as the minimal transition frequency (cf. Sec. 4.2.2). These values of Δ will

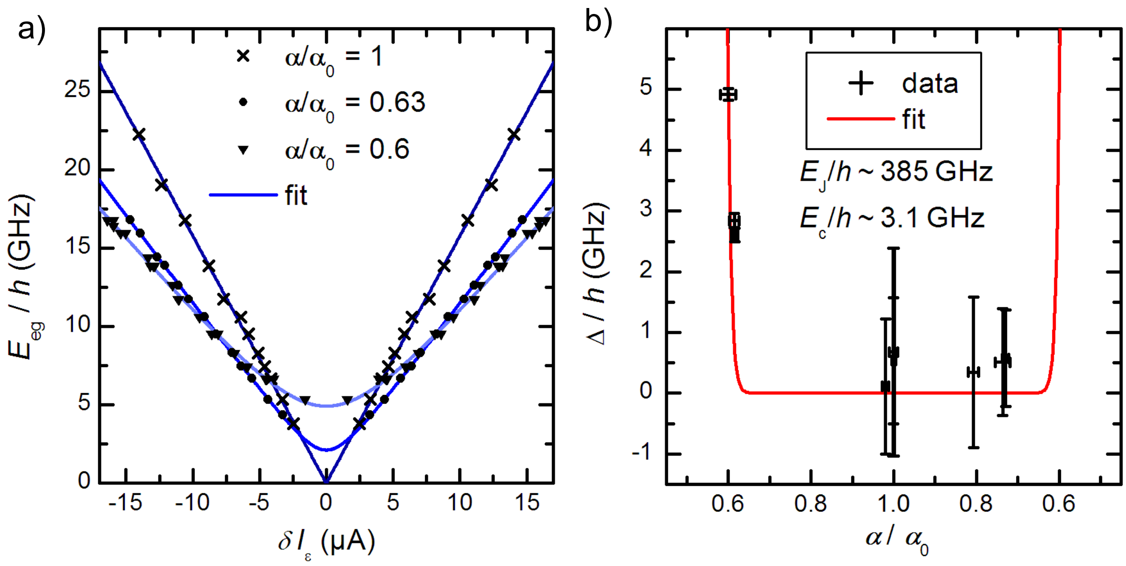

Figure 4.8 – **a)** Peak and dip positions for three exemplary α-values as a function of ε-current. Blue curves correspond to the applied two-parameter fits. The α-value was changed via the solenoid only. The change of the minimal transition frequency Δ/h can be clearly observed as the change of each curve's minimum; **b)** Minimal transition frequency Δ/h plotted as a function of corresponding α-value. Data points to the left of $\alpha/\alpha_0 = 1$ belong to negative coil current values and vice versa. The red curve is a fit of (4.3.6), which is in good agreement with the data and yields plausible values $E_{\mathrm{J0}}/h = (383 \pm 480)$ GHz and $E_{\mathrm{c}}/h = (3.1 \pm 3.4)$ GHz. This fit shows in a formidable way that the tunnel coupling of a gradiometric qubit is tuned in a reliable way.

finally be used to extract the characteristic energies E_{J0} and E_{c} as fit parameters.
In Fig. 4.8a the peak and dip positions for three exemplary α-values are plotted as well as the applied two-parameter fits. The different values of α have been adjusted by different frustrations of the trap-loop induced by the solenoid as described in the previous section. For better comparability, each curve is centered to $\delta I_\varepsilon = (I_{\mathrm{peak}} - I_{\mathrm{dip}})/2 = 0$, where I_{peak} and I_{dip} are the current values at which peak and dip appeared, respectively. This graph shows clearly that the minimal transition frequency of the qubit can be tuned from close to zero to over 5 GHz.
The change of Δ corresponding to different values of α will in the following be quantitatively analyzed with respect to the characteristic energies E_{J0} and E_{c}. These energies can be extracted as fit parameters when fitting the tunnel coupling for various α. In order to obtain reliable values for E_{J0} and E_{c}, the estimation of (2.4.5) has to be derived in more detail, yielding [2]

$$\frac{\Delta}{h} = \sqrt{\frac{4E_{\mathrm{J0}}E_{\mathrm{c}}(4\alpha^2 - 1)}{\alpha(1 + 2\alpha)}} \exp\left(-\sqrt{\frac{E_{\mathrm{J0}}}{E_{\mathrm{c}}}}\alpha\right), \tag{4.3.6}$$

which is used to obtain E_{J0} and E_{c} as fit parameters when plotting Δ vs. α.
In Fig. 4.8b the minimal transition frequency Δ/h is plotted as a function of α for each qubit hyperbola recorded with the tunable qubit. The values for small tunnel couplings

around $\alpha \approx 1$ have large error bars due to missing peak and dip coordinates in the vicinity of $\delta I_\varepsilon = 0$. However, this does not strongly affect a fit of (4.3.6) since the behavior of (4.3.6) is mainly determined by values with large Δ, i.e. $\alpha \approx 0.6$. The red curve is a fit of (4.3.6) to the data, which yields $E_{\mathrm{J0}}/h = (383 \pm 480)\,\mathrm{GHz}$ and $E_{\mathrm{c}}/h = (3.1 \pm 3.4)\,\mathrm{GHz}$. These values of E_{J0} and E_{c} are in formidable agreement with values obtained independently from the readout-SQUID IVC, which are $E_{\mathrm{J0}}/h \approx 365\,\mathrm{GHz}$ and $E_{\mathrm{c}}/h \approx 2.9\,\mathrm{GHz}$.
The values E_{J0} and E_{c} extracted from the fit have a large relative error of the order of 100%, which is mostly due to the small amount of data points used for the fit. Here one was restricted because of limited possible readout positions on the readout-SQUID curve. Nevertheless, the fit shows in a remarkable way that it has been achieved to tune the tunnel coupling in a reliable way. The values obtained for E_{J0} and E_{c} are plausible with respect to values extracted from the readout-SQUID current-voltage characteristic. Thus the technique using the readout-SQUID IVC is confirmed to be a well suited method for reliable determination of qubit parameters.
The calculated ratio $E_{\mathrm{J0}}/E_{\mathrm{c}} \approx 125$ is in perfect agreement with the ratio $E_{\mathrm{J0}}/E_{\mathrm{c}} \approx 126$ taken from the readout-SQUID IVC. Nevertheless, both ratios are relatively high for flux qubits, which results in the fact that the largest Δ achieved by tuning is around 5 GHz. A typical resonator used in circuit-QED experiments is operated at approximately 5-7 GHz, so that for future fabrication of qubits it should be tried to decrease the ratio $E_{\mathrm{J0}}/E_{\mathrm{c}}$ in order to be sure to reach this range with the tunable qubit.
A more precise analysis of the data requires more data points, which can for example be achieved by an optimized readout process. This could be realized via galvanic coupling between SQUID and trap-loop to obtain a larger qubit signal so that qubit hyperbolas can be recorded for operation points located closer to a maximum of the switching current curve. A second method can be to increase the area of the SQUID to have more minima of the SQUID's switching current curve within one oscillation of the switching current characteristic of the α-SQUID. However, a trade-off between the gain in possible readout points and the increase in flux noise due to the larger area of the SQUID has to be made.

Generally, the central result of this section is that a reliably tunable tunnel coupling has been successfully realized, which should give rise to future developments of the tunable design, which can be exploited in various applications. The tuning of Δ has been used to extract trustworthy values of the characteristic energies E_{J0} and E_{c}, which will in the following section be achieved by tuning Δ via an on-chip line.

4.3.4 Tuning Δ via the α-line

A possible way to tune Δ without changing the global frustration of all loops placed on the sample, as it is the case when using the solenoid, is to use an on-chip flux line. This α-flux line couples via a mutual inductance to the α-SQUID as described in detail in Sec. 3.3.2. In this section a change of Δ induced by the α-line is used to determine the characteristic energies E_{J0} and E_{c} analogously to the previous section.

The I_α depending value $\alpha(I_\alpha)$

The mutual inductance between α-line and α-SQUID for the tunable qubit presented in this section is too small to change the α-loop frustration on the required scale, i.e. $\delta f_{\alpha,\mathrm{act}} = \pm 0.25$. The main reason for this is that the heating issue discussed in Sec. 3.6 was not completely resolved for this sample, resulting in an temperature increase for current values larger than $I_\alpha = \pm 200\,\mu\mathrm{A}$.
To detect a change of Δ induced by the α-line, the α-SQUID can be biased at a working point $\alpha(f_{\alpha,\mathrm{act}}) = \alpha_\mathrm{b} \approx 0.6$, where the tuned qubit potential results in $\Delta \gg 0$. At this point the slope of (4.3.6) is steep, i.e. $\partial\Delta/\partial f_{\alpha,\mathrm{act}}$ takes large values, so that the value of Δ changes significantly even for small changes of $f_{\alpha,\mathrm{act}}$. Generally, the frustration $f_{\alpha,\mathrm{act}}$ close to 0.6 can be applied in two ways: On the one hand a certain odd number of flux quanta can be trapped such that

$$\cos\left(\pi\frac{A_\alpha}{A_\mathrm{tr}}\frac{1}{1+\beta}n\right) \overset{!}{\approx} 0.6, \tag{4.3.7}$$

on the other hand the solenoid can be used to frustrate the α-SQUID. Even though the latter has been done for the measurements presented here, the use of trapped flux quanta is probably the solution that creates less flux noise and is also more stable over time due to the strong restriction of fluxoid quantization. However, since no qubit step was detected for other values than $n = 1$, one was constrained to use the solenoid to bias the α-SQUID. The value α_b can be precisely evaluated using the calibration performed in Sec. 4.3.2. For the results presented in this section, the α-SQUID was biased at $\alpha_\mathrm{b} \approx 0.65$ for zero α-current applied. This seemed to be the best choice for α_b considering the restriction to possible working points of the readout-SQUID.
However, the calibration presented in Sec. 4.3.2 cannot be taken to determine $\alpha(I_\alpha)$ since a different transfer function than $H_{\alpha\mathrm{c}}$ has to be used. To extract α from varying asymptotic slopes $\eta(I_\alpha)$ of different qubit hyperbolas, a transfer function

$$H_{\alpha\alpha} = \frac{\partial f_{\alpha,\mathrm{act}}}{\partial I_\alpha} \tag{4.3.8}$$

is introduced. Using (4.3.8) as well as the value of α_b for $I_\alpha = 0$, the values of $\eta(I_\alpha)$ follow

$$\eta(I_\alpha) = \eta_\mathrm{c} \cdot \sqrt{1 - \left[2\left|\cos\left(\arccos(\alpha_\mathrm{b}) + \pi H_{\alpha\alpha}\cdot I_\alpha\right)\right|\right]^{-2}}, \tag{4.3.9}$$

which can be used to determine $\alpha(I_\alpha)$. In (4.3.9) η_c is a constant extracted from the fit of (4.3.4) performed in Sec. 4.3.2.
In Fig. 4.9a the asymptotic slope η is plotted as a function of applied current I_α through the α-line (black circles). There is a significant change of η with respect to I_α, following the expected behavior. The change of η is in this case given as an increase of η for positive α-current and vice versa. However, this increase of η for positive current values is only given by the connection between α-line and output of the current source, which can be easily inverted. A fit of (4.3.9) results in the blue curve in Fig. 4.9a with $H_{\alpha\alpha} = (6.2 \pm 0.3)\cdot 10^{-5}\,\mu\mathrm{A}^{-1}$. Thus, α can be calculated to

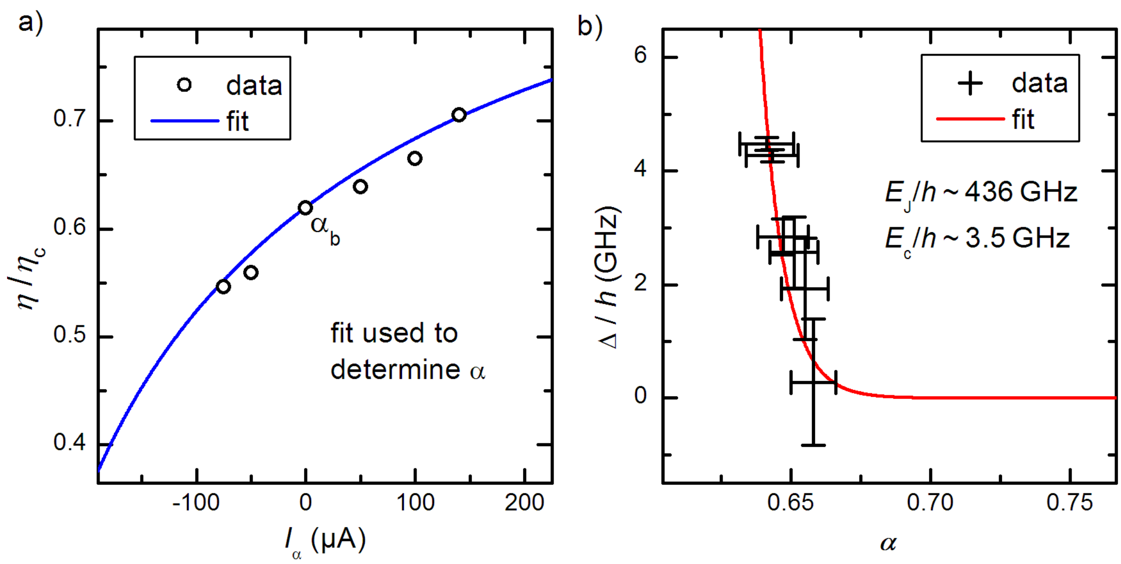

Figure 4.9 – **a)** Asymptotic slope η as a function of applied α-current I_α: The data follows the expected behavior, which is in this case an increase of α for positive α-current and vice versa. The fit (blue line) is used to determine the value α, which is taken for the plot in (b). The value of α_b belonging to $I_\alpha = 0$ is precisely known from a calibration in Sec. 4.3.2; **b)** Minimal transition frequency Δ/h plotted as a function of the corresponding α-value. The red curve is a fit of (4.3.6), which yields plausible values $E_{\mathrm{J}0}/h \approx 436\,\mathrm{GHz}$ and $E_\mathrm{c}/h \approx 3.5\,\mathrm{GHz}$.

$$\alpha = |\cos\left(\pi\left[\arccos(\alpha_\mathrm{b}) + I_\alpha \cdot H_{\alpha\alpha}\right]\right)|, \tag{4.3.10}$$

which is used in the following paragraph to extract the characteristic energies $E_{\mathrm{J}0}$ and E_c from varying tunnel coupling.

Determination of $E_{\mathrm{J}0}$ and E_c

Analogously to the procedure described in Sec. 4.3.3, the characteristic energies $E_{\mathrm{J}0}$ and E_c can be determined from measurements where Δ is tuned via the on-chip α-line. The α-calibration described in the previous paragraph can be used to plot Δ as a function of α, which allows to extract $E_{\mathrm{J}0}$ and E_c from a fit of (4.3.6).

In Fig. 4.9b the measured tunnel coupling Δ is plotted as a function of the corresponding α-value (black crosses). The red curve is a fit of (4.3.6) applied analogously to the description in Sec. 4.3.3, which gives $E_{\mathrm{J}0}/h = (436 \pm 218)\,\mathrm{GHz}$ and $E_\mathrm{c}/h = (3.5 \pm 1.2)\,\mathrm{GHz}$. This is in agreement with the values of $E_{\mathrm{J}0}$ and E_c evaluated in the previous section, as well as to the values extracted from the readout-SQUID IVC. The overall agreement shows in a formidable way that it is possible to tune the tunnel coupling not only via an external device, i.e. a solenoid, but also in a controlled way using an integrated on-chip α-line.

The fit performed in Fig. 4.9b yields smaller relative errors than the fit performed in Sec. 4.3.3, which results in a higher accuracy. This is mainly to the fact that the values of Δ are larger and thus more precise to determine. The fact that for both fits only 6-8 data points were available makes it hard to say which values are more precise. Anyhow, the ratio $E_{J0}/E_c \approx 120$ is in a remarkable good agreement to the ratio $E_{J0}/E_c \approx 125$ determined in Sec. 4.3.3 and $E_{J0}/E_c \approx 125$ taken from the readout-SQUID IVC, which can thus be assumed to be very precise.

The central result of this section is that the here presented design can be used to tune Δ by changing the frustration of the α-SQUID via an on-chip line. This design is a big step towards an integrated circuit since the design can be reproduced with a high accuracy. The advantage of using an on-chip line is that other superconducting loops, e.g. additional qubits or SQUIDs, placed not too close to the α-line will stay unaffected by tuning this qubit. This is in difference to a tuning achieved via the solenoid and can be used for systems with several simultaneously operating devices that are sensitive to flux changes.

4.3.5 Deducing the tunnel coupling from SQUID IVCs

In this section the results of the two previous section are summarized and compared to a simulation using independently determined values for E_{J0} and E_c. In Fig 4.10 the tunnel couplings obtained from tuning via the solenoid as well as from tuning via the α-line are shown (black & blue points in Fig. 4.10). This plot can be taken as a further approval of the parameters E_{J0} and E_c found in the previous sections since there is an overall good agreement between data and simulation. This agreement can however only be qualitatively evaluated since the simulation routine does not allow to fit the simulated transition frequencies. In table 4.1 the central result of this thesis is summarized providing an overview of the important parameters E_{J0} and E_c as well as their ratio E_{J0}/E_c.

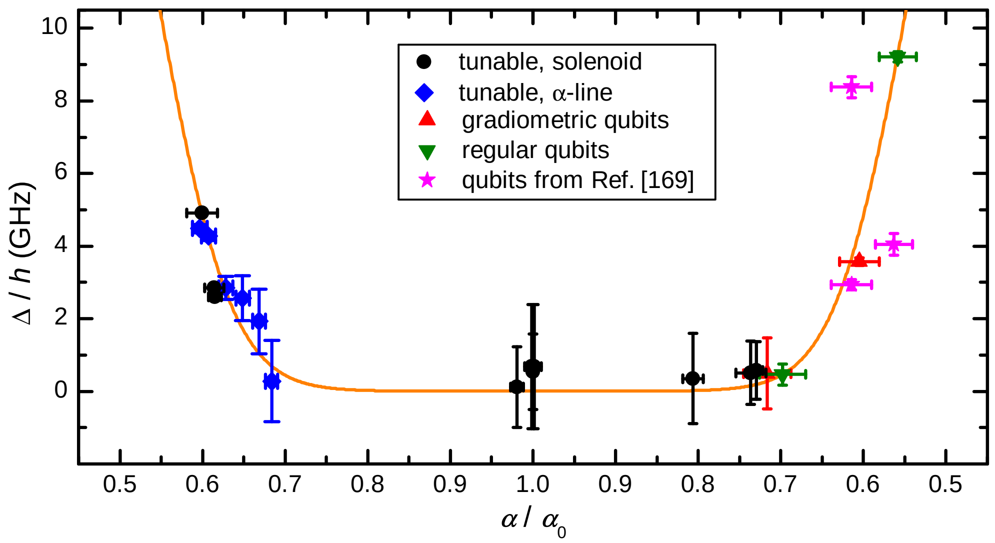

Figure 4.10 – Minimal transition frequency of all qubits that have been measured in this thesis together with qubits from Ref. [169] as a function of α after a transformation of Δ performed with (4.3.11). In this graph the tunable qubit is chosen as reference value for the data points as well as for the simulation (orange curve).

Table 4.1 – Characteristic energies E_{J0} and E_{c} as well as their ratio $E_{\mathrm{J0}}/E_{\mathrm{c}}$ determined by three different methods, which are in good agreement. The techniques using a solenoid are described in detail in Sec. 4.3.3 & Sec. 4.3.4, respectively. The values of E_{J0} and E_{c} used for the simulation are determined as described in Sec. 4.1. In this case it is hard to evaluate an error, which is mostly determined as a systematical error. This table represents the central result of this thesis.

method	E_{J0}/h	E_{c}/h	$E_{\mathrm{J0}}/E_{\mathrm{c}}$
solenoid	(383 ± 480) GHz	(3.1 ± 3.4) GHz	~ 125
alpha-line	(436 ± 218) GHz	(3.5 ± 1.2) GHz	~ 120
simulation	365	2.9	~ 126

The tunnel coupling of qubits fabricated on different wafers cannot be compared directly with each other since there is always some spread in fabrication resulting in different characteristic energies E_{J0} and E_{c}. However, the tunnel coupling Δ will be a directly comparable value, if a normalization is applied to obtain a normalized Δ_{n}, which can for example be done multiplication with a factor inverse proportional to (4.3.6) to calculate

$$N_\Delta = \underbrace{\sqrt{\frac{1}{E_{\mathrm{J0}}E_{\mathrm{c}}}}\exp\left(\sqrt{\frac{E_{\mathrm{J0}}}{E_{\mathrm{c}}}}\right)}_{\propto(4.3.6)^{-1}}, \tag{4.3.11}$$

which is then independent of E_{J0} and E_{c}. Such a normalization can be used to scale the normalized value Δ_{n} of a first qubit with the characteristic energies $\tilde{E}_{\mathrm{J0}}$ and $\tilde{E}_{\mathrm{c}}$ of a second qubit, yielding

$$\tilde{\Delta} = \Delta N_\Delta \sqrt{\tilde{E}_{\mathrm{J0}}\tilde{E}_{\mathrm{c}}}\exp\left(-\sqrt{\frac{\tilde{E}_{\mathrm{J0}}}{\tilde{E}_{\mathrm{c}}}}\right). \tag{4.3.12}$$

These rescaled values $\tilde{\Delta}$ of the first qubit are then following the same curve $\Delta(\alpha)$ as the values Δ of the second qubit, which allows direct comparison.
For a comparison between tunnel couplings of all kind of qubits fabricated in this thesis and qubits characterized previously at the WMI[2] [169], the values of Δ have been normalized with (4.3.11) and then rescaled with $\tilde{E}_{\mathrm{J0}}$ and $\tilde{E}_{\mathrm{c}}$ of the tunable qubit. The result is shown in Fig. 4.11b together with a simulation of the minimal transition frequency (orange line) using $\tilde{E}_{\mathrm{J0}}$ and $\tilde{E}_{\mathrm{c}}$ of the tunable qubit. Considering the fact that Δ itself is only a fit parameter and the assumption (4.3.11), there is a remarkable agreement between data and simulation. Generally, the plot in Fig. 4.10 shows that the qubit fabrication routine at the WMI has come to a point where it can be thought of designing a certain tunnel coupling desired for a special application. This fact, together with the obtained ability to tune the tunnel coupling of a single qubit, is a big step towards the controlled engineering of circuit-QED architectures.

[2] These qubits are standard three Josephson junction flux qubits fabricated and characterized at the the WMI. A detailed description of these qubits can be found in Ref. [150] & [163].

4.3.6 The magnetic energy ε and the inductance ratio β

To obtain a complete quantitative description of the tunable qubit, the magnetic energy ε as well as the inductance ratio β are determined in this section.

The magnetic energy ε

The magnetic energy ε is obtained via a scaling factor x, which is introduced in Sec. 4.2. This factor allows to make the transition from η to ε, i.e. from ε-current as reference value to δf_{q} as reference value. In contrast to the non-tunable gradiometric qubit, where the value of x has to be determined for each qubit and thus for each qubit hyperbola, the scaling factor is constant for the different hyperbolas recorded with the tunable qubit. This allows to use the tunable qubit for a consistent probe of the parameters E_{J0} and E_{c} used for simulations.
Because E_{J0} and E_{c} are fixed by fabrication but α can change, it is necessary to find suitable values for E_{J0} and E_{c} being used as simulation parameters, which reproduce each measured qubit hyperbola. In the following it will be shown that the procedure described in Sec. 4.1 is well suited to find appropriate values for E_{J0} and E_{c}, which can be used in simulations to describe the measured hyperbolas with high accuracy.
As described in Sec. 4.1, the charging energy E_{c} is calculated using the specific capacitance $\tilde{c}$ as well as the junction area A_{J}. The Josephson coupling energy E_{J0} is obtained using the value $I_{\mathrm{c}}^{\mathrm{AB}}$ of the corresponding readout-SQUID. However, for the tunable qubit the value α can obviously not be determined from SEM images so that the calibration described in Sec. 4.3.2 is used to obtain α.
As all simulations performed in Sec. 4.1 & Sec. 4.2 have very precisely reproduced the measured qubit behavior, a first try to simulate the transition frequencies has been made for the case $\alpha = 0.6$, using the values $E_{\mathrm{J0}}/h = 365\,\mathrm{GHz}$ and $E_{\mathrm{c}}/h = 2.9\,\mathrm{GHz}$ extracted from the SQUID IVC. The relatively small α-value was chosen because it corresponds to the highest measured Δ and therefore yields a high comparability between data and simulation. It should be noted that it was purposeful not to use the values of E_{J0} and E_{c} extracted in the sections above, since the goal was to probe whether suitable simulation parameters can be found *before* characterizing the qubit. Therefore it is required to assume values for E_{J0} and E_{c}, which can for example be obtained from a SQUID characterization at 500 mK.
The result is plotted as a red curve in Fig. 4.11a together with measured data, proving a formidable agreement after the I_ε-axis has been scaled with $x = 5 \cdot 10^{-4}$.
As this could be reproduced for all other qubit hyperbolas recorded with the tunable qubit (two are examplarily shown as blue curves in Fig. 4.11a), it can be assumed that the chosen parameters E_{J0} and E_{c} are close to the actual parameters of this qubit. Thus, a further validation of the parameters for E_{J0} and E_{c} evaluated in the previous sections is provided. This result implies that the specific capacitance $\tilde{c}$ determined in Sec. 3.1 as well as the critical current I_{c}^{AB} extracted from the SQUID IVC at $T = 500\,\mathrm{mK}$ are suitable values to simulate the transition frequencies of future fabricated qubits.
To show the impressive agreement between simulation and data/fit, the simulations in Fig. 4.11a correspond to the same data selected for the fitted curves shown in Fig. 4.11b.

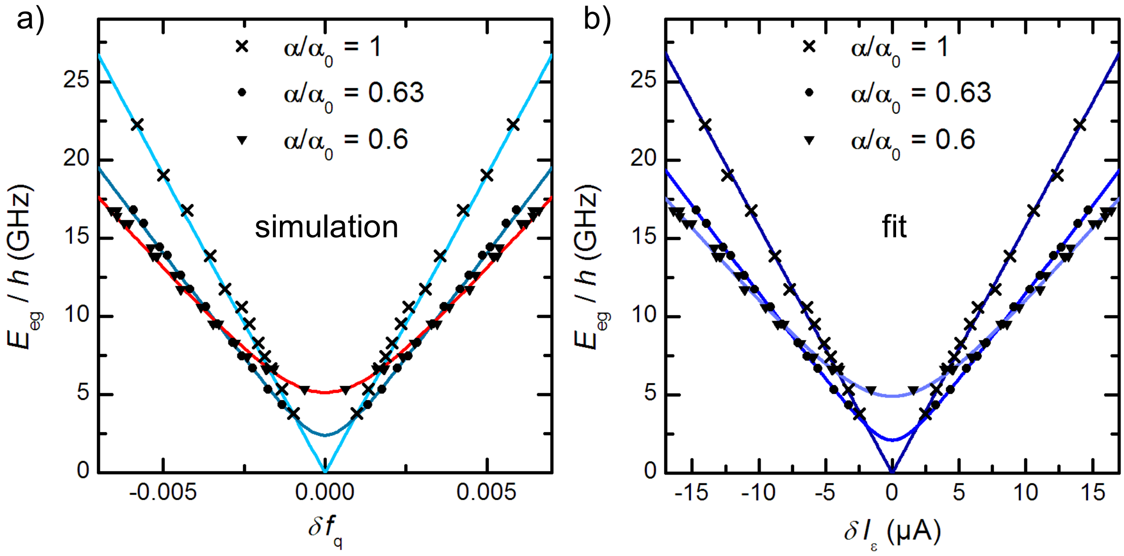

Figure 4.11 – **a)** Red curve: Simulated transition frequency together with measured data using simulation parameters E_{J0}, E_{c} and α, which were extracted from the SQUID IVC. The blue curves are simulated with equal values of E_{J0} and E_{c} but different α-value, which is equal to the α-value of the measured data. There is remarkable agreement between data and simulation for all values of α for which qubit hyperbolas have been recorded; **b)** Graph taken from Fig. 4.8a, showing measured data together with the two-parameter fits, which can be taken as a guide to the eye to recognize the formidable agreement between simulation in (a) and fit in (b).

From the bare eye it is hard to detect any difference between the two graphs.
A consistency check of x can be made by comparing the fit parameter η_{c} in (4.3.4) to the pre-factor $2\Phi_0 I_{\mathrm{c}}$ in (4.3.2),

$$x \cdot \eta_{\mathrm{c}} = 2\Phi_0 I_{\mathrm{c}}, \tag{4.3.13}$$

to calculate the critical current of the qubit junctions. Performing this calculation yields $I_{\mathrm{c}} = 715\,\mathrm{nA}$, which agrees very well to $I_{\mathrm{c}}^{\mathrm{AB}} = 728\,\mathrm{nA}$ extracted from the SQUID's IVC. Thus, a reliable technique to determine $\varepsilon = x \cdot \eta$ is obtained, which results in values $\varepsilon \approx 3.8/h\,\mathrm{GHz/m}\Phi_0$ for $\alpha \approx 1$ and $\varepsilon \approx 2.4/h\,\mathrm{GHz/m}\Phi_0$ for $\alpha \approx 0.6$.

The inductance ratio β

For further developments of the qubit design presented in this section it is essential to know the value of the ratio between geometric and kinetic inductance of the given trap-loop geometry: $\beta = L_{\mathrm{g,tr}}/L_{\mathrm{k,tr}}$ (cf. Sec. 3.3.2). Descriptively, β defines the oscillation period of $\eta(I_{\mathrm{coil}})$ in (4.3.4), i.e. the difference in I_{coil} that changes the frustration of the α-loop by $\delta f_{\alpha,\mathrm{act}} = \pm 1$, which can be evaluated as

$$\delta I_{\mathrm{coil}}^{\alpha} = |I_{\mathrm{coil}}(f_{\alpha,\mathrm{act}} = N) - I_{\mathrm{coil}}(f_{\alpha,\mathrm{act}} = N \pm 1)|. \tag{4.3.14}$$

This can for example be the difference between two adjacent I_{coil}-values where α becomes zero (red in Fig. 4.7). With the knowledge of β, future gradiometric qubits can be designed in a way that the physically interesting regimes, where $\Delta \gg 0$, belong to SQUID working points with sufficient readout quality.
To calculate β, also the difference $\delta I_{\text{coil}}^{\text{SQ}}$ has to be determined, which is in analogy to (4.3.14) the difference in coil-current that changes the SQUID frustration exactly by one flux quantum (cf. Fig. 4.7). With $\delta I_{\text{coil}}^{\text{SQ}}$ the difference in coil-current necessary to change the frustration of an area equally sized as the trap-loop by one flux quantum can be calculated as

$$\delta I_{\text{coil}}^{\text{tr}} = (1 + \delta\nu)\frac{A_{\text{SQ}}}{A_{\text{tr}}}\delta I_{\text{coil}}^{\text{SQ}}. \tag{4.3.15}$$

Here the factor $(1 + \delta\nu)$ is the correction factor, that has to be taken into account due to the induced field in the readout-SQUID generated by the circulating current of the trap-loop. This factor $(1 + \delta\nu)$ can be determined as described in detail in Sec. 3.5. Assuming that the solenoid generates a homogeneous magnetic field, one can equate the ratios

$$\frac{\delta I_{\text{coil}}^{\alpha}}{\delta I_{\text{coil}}^{\text{tr}}} \stackrel{!}{=} \frac{f_{\text{tr}}}{f_{\alpha}}. \tag{4.3.16}$$

With the assumption (4.3.16) and the use of (3.3.7), where the factor $n\beta/(1+\beta)$ can be neglected since n does not change during the experiment, β can be determined by

$$\begin{aligned}\beta &= \frac{A_{\alpha}}{A_{\text{tr}}}\frac{f_{\text{tr}}}{f_{\alpha}} - 1 \\ &= \frac{1}{1+\delta\nu}\frac{A_{\alpha}}{A_{\text{SQ}}}\frac{\delta I_{\text{coil}}^{\alpha}}{\delta I_{\text{coil}}^{\text{SQ}}} - 1,\end{aligned} \tag{4.3.17}$$

which is $\beta = 0.79$ for the actual trap-loop geometry. This is in very good agreement with $\beta = 0.81$ obtained from Sec. 3.4 and shows that the technique to determine β described in that section is reliable.
Knowing β, all possible values of n resulting in α larger than 0.5 for $I_{\text{coil}} = 0$, where and so qubit steps are expected to be observable, can be calculated. Unfortunately, it was not possible to detect a qubit step for values different than $n = 1$ even though the system is expected to work for the neighboured values $n = -1$, and $n = \pm 3$, too ($\alpha = 0.97$ and $\alpha = 0.73$, respectively). Even after careful examination to detect qubit steps for these values of n, there was no reproducible measurement that affirmed a possible step. At this point it is hard to say, why no qubit steps were detected for additional values of n, which was has been demonstrated for the non-tunable gradiometric qubit. One possible explanation could be the fact that the actual frustration of the α-SQUID may have changed in an uncontrolled way with n, which could be due to a small quality factor $Q_{\text{grad}}(n)$. However, it is not possible to determine $Q_{\text{grad}}(n)$ for the tunable qubit since at least two n are required for that.

4.3.7 Optimizing the tunable qubit

Since the tunable qubit presented in this section is the first successful realization of such a system at the WMI, there is much space for further improvements and developments. However, the actual size and shape of the trap-loop should not be changed too much, to not render all characterization performed in this work useless.

One important first step is to increase the readout quality since measurements were mainly obstructed because of too small qubit signals. To achieve this, the readout-SQUID can be coupled galvanically to the trap-loop to increase the mutual inductance between SQUID and qubit, which also increases the signal strength. As the actual readout-SQUID was not shunted by an additional capacitance, this can be changed in future designs to be less sensitive to rf-noise and to increase qubit coherence times [132, 150, 163, 170]. Furthermore, the area of the readout-SQUID junctions can be increased to be more sensitive to flux changes. In this point one is however limited by the screening factor β_{L} given in (2.3.2), which should not exceed $\beta_{\mathrm{L}} = 1$. The screening parameter of a typical readout-SQUID fabricated in this work is approximately $2 \cdot 10^{-3}$, so that the junction area could be increased to cover the whole width of the aluminum layers ($w = 506\,\mathrm{nm}$) without running into problems concerning β_{L}.

One main goal must be to control the qubit potential only by the α-flux line, which is important for systems that contain several qubits. In such a system single qubits must be selectively controlled while other qubits placed on the same sample stay unaffected. Since the maximal current through the α-line is limited, the qubit must be designed such that

$$H_{\Delta\alpha} = \left|\frac{\partial\Delta}{\partial\alpha}\right|_{\alpha_{\mathrm{b}}\approx\frac{2}{3}} = \left|\frac{\partial\Delta}{\partial\left[\alpha_0|\cos(\pi f_{\alpha,\mathrm{act}})|\right]}\right|_{f_{\alpha,\mathrm{act}}\approx\arccos\left(\frac{2}{3\alpha_0}\right)} \stackrel{!}{=} \max, \tag{4.3.18}$$

where $\alpha_{\mathrm{b}} \approx \frac{2}{3}$ is the working point at which the qubit is biased to have a tunnel coupling in the GHz regime. Equation (4.3.18) implies on the one hand that parameters for E_{J0} and E_{c} have been selected, which result in a large slope of (4.3.6) at a certain point α_{b}. On the other hand significant changes of $f_{\alpha,\mathrm{act}}$ must be possible using only the on-chip line.

One idea to be more sensitive to external flux induced by the on-chip line is to decrease the ratio $\beta = L_{\mathrm{g,tr}}/L_{\mathrm{k,tr}}$ of the trap-loop. Since $L_{\mathrm{g,tr}}$ can only be changed by varying the trap-loop size, an advisable solution can be to decrease the cross-section of the aluminum layers to increase $L_{\mathrm{k,tr}}$, cf. (2.1.6). During the fabrication process the layer thickness is more ore less fixed so that the layer width w has to be decreased in order to increase $L_{\mathrm{k,tr}}$. The layer width can be decreased to a value limited by the SEM writing accuracy[3], which is around 50 nm. This means that β can be decreased by a factor $50/506 \approx 0.1$ resulting in $\beta \approx 0.08$ compared to $\beta \approx 0.8$ in the actual layout.

However, for possible applications where the gradiometric qubit is coupled galvanically to a transmission line resonator it is advantageous to design the α-SQUID in a way that

[3] It should be noted that at the points where the Josephson junctions are located the layer width must be adjusted to the width of the Josephson junctions, which is approximately $w_{\mathrm{J}} = 200\,\mathrm{nm}$ for typical junctions in this work.

it shares one of its edges with the trap-loop. In such a design the value α is mainly determined by the kinetic phase difference across this edge (cf. Ref. [18]). In this case individual parameters for the layer width have to be determined, which can be chosen as in this thesis to keep the kinetic inductance small, which is a precondition in the deviation of the qubit potential given by (2.4.2).
Another way to increase the sensitivity $H_{\Delta\alpha}$ is to increase α_0, i.e. increase the junction area of the α-SQUID junctions, cf. inset of Fig. 4.12b. Larger α-SQUID junctions result in a larger sensitivity of $f_{\alpha,\mathrm{act}}$ to external flux, which is given as

$$H_{\alpha f}(f_{\alpha,\mathrm{act}}) = \frac{\partial\left[\alpha_0|\cos(\pi f_{\alpha,\mathrm{act}})|\right]}{\partial f_{\alpha,\mathrm{act}}} = -\frac{\alpha_0}{2}\frac{\sin(2\pi f_{\alpha,\mathrm{act}})}{\sqrt{\cos^2(\pi f_{\alpha,\mathrm{act}})}}, \tag{4.3.19}$$

and plotted for clarity in Fig. 4.12a. To evaluate the sensitivity of α with respect to the junction area of the α-SQUID it has to be taken into account that the α-SQUID frustration resulting in $\alpha = \alpha_\mathrm{b} = 2/3$ is further depending on α_0. Therefore (4.3.19) can be rewritten for $\alpha_0, \alpha_\mathrm{b} > 0$ to

$$\begin{aligned} H_{\alpha f}\left(\alpha_0, \alpha_\mathrm{b}\right) &= -\frac{\alpha_0\pi}{2}\sin\left(1 - 2\arccos\left(-\frac{\alpha_\mathrm{b}}{\alpha_0}\right)\pi^{-1}\right)\sec\left(1 - \arccos\left(-\frac{\alpha_\mathrm{b}}{\alpha_0}\right)\pi^{-1}\right) \\ &\overset{\alpha_\mathrm{b}=\frac{2}{3}}{=} -\alpha_0\pi\sin\left(1 - \arccos\left(-\frac{2}{3\alpha_0}\right)\pi^{-1}\right), \end{aligned} \tag{4.3.20}$$

where the case for $\alpha_\mathrm{b} = 2/3$ is plotted in Fig. 4.12b. Equation (4.3.20) implies that in the limiting case $\alpha_0 = \alpha_\mathrm{b}$ the α-SQUID frustration must not be changed at all, i.e. $f_{\alpha,\mathrm{act}} = 0$, to result in $\alpha = \alpha_\mathrm{b}$ (gray line in Fig. 4.12b). For increasing α_0 the sensitivity increases, so that large α-SQUID junctions can be used for a higher sensitivity and thus for fast changes of Δ. However, increasing the area of the α-SQUID junctions decreases the charging energy of these junctions significantly while the charging energy of the other qubit junctions is unaffected. This modifies the qubit potential in an undetermined way, which could be obstructing the double well potential. However, values for $\alpha_0 > 1$ could also be used to study the crossover from inter-cellular tunneling to intra-cellular tunneling.
To maximize (4.3.18) one has the freedom to set up the characteristic energies $E_{\mathrm{J}0}$ and E_c during fabrication with the constraint that the ratio $E_{\mathrm{J}0}/E_\mathrm{c}$ stays of the order of 20 to 100. For all qubits characterized in this thesis this ratio was approximately 130, i.e. relatively high, so that for example Δ/h could not be tuned higher than 5 GHz with the tunable qubit. In future applications higher values for Δ/h can be required so that the ratio $E_{\mathrm{J}0}/E_\mathrm{c}$ must be decreased. To decrease this ratio either $E_{\mathrm{J}0}$ can be decreased, which can be achieved by longer oxidation times, or E_c can be increased, which can be achieved by smaller areas of the qubit junctions. Unfortunately, current densities are hard to control during the oxidation process, which can be seen by the fact that during this thesis the oxidation time had to be increased from 21 to almost 26 minutes to sustain equal current densities. This fact shows that current densities are hard to predict and implies that is probably the more sophisticated solution to decrease the junction area than to decrease the current densities. It should also be noted that smaller junction areas A_J unavoidably

result in smaller values of E_{J0}, which therefore further decreases the ratio E_{J0}/E_c.
In Fig. 4.12c the minimal transition frequency is plotted as a function of E_{J0}/E_c for either constant E_{J0} or constant E_c. The point at which both curves intersect belongs to $E_{J0}/E_c \approx 135$, which is roughly the value of qubits fabricated in this thesis. For the black curve the Josephson energy was swept and the charging energy was kept constant at $E_c/h = 3\,\mathrm{GHz}$, which is a typical value for qubits in this thesis. This results in a relative small increase of Δ/h for decreasing E_{J0}/E_c. For the red curve the Josephson energy was kept constant at $E_{J0}/h = 400\,\mathrm{GHz}$ and E_c was swept, which results in a strong increase of Δ for decreasing E_{J0}/E_c. Unfortunately the simulation program is not able to take account of the effect that smaller values for E_c, i.e. smaller junction areas, simultaneously effect E_{J0}. However, it can be seen from these simulations that changing E_c has a much stronger effect on Δ than changing E_{J0}, which emphasizes the increase of E_c for future qubits to reach higher tunnel couplings.
Finally, the slope of (4.3.18) can be increased by adjusting α, E_{J0} and E_c, respectively A_J. In Fig. 4.12d the minimal transition frequency Δ/h is plotted as a function of α for various areas A of the two larger qubit junctions. The case $A/A_J = 1$ represents the case of a typical qubit with parameters E_{J0} and E_c found during this thesis. For the other curves it was assumed that $E_{J0} \propto A$ and $E_c \propto 1/A$, so that the values of E_{J0} and E_c were adjusted in this way for the simulations. Unfortunately, the slope at a typical working point $\Delta/h = 6\,\mathrm{GHz}$ is decreased for smaller junction areas, i.e. smaller E_{J0}/E_c (cf. dashed lines in Fig. 4.12d), which is counterproductive if E_{J0}/E_c is decreased to reach higher tunnel couplings. Therefore a trade-off between a large tunnel coupling and a high sensitivity $\partial\Delta/\partial\alpha$ has to be found, which is around $A/A_J \approx 0.7$.

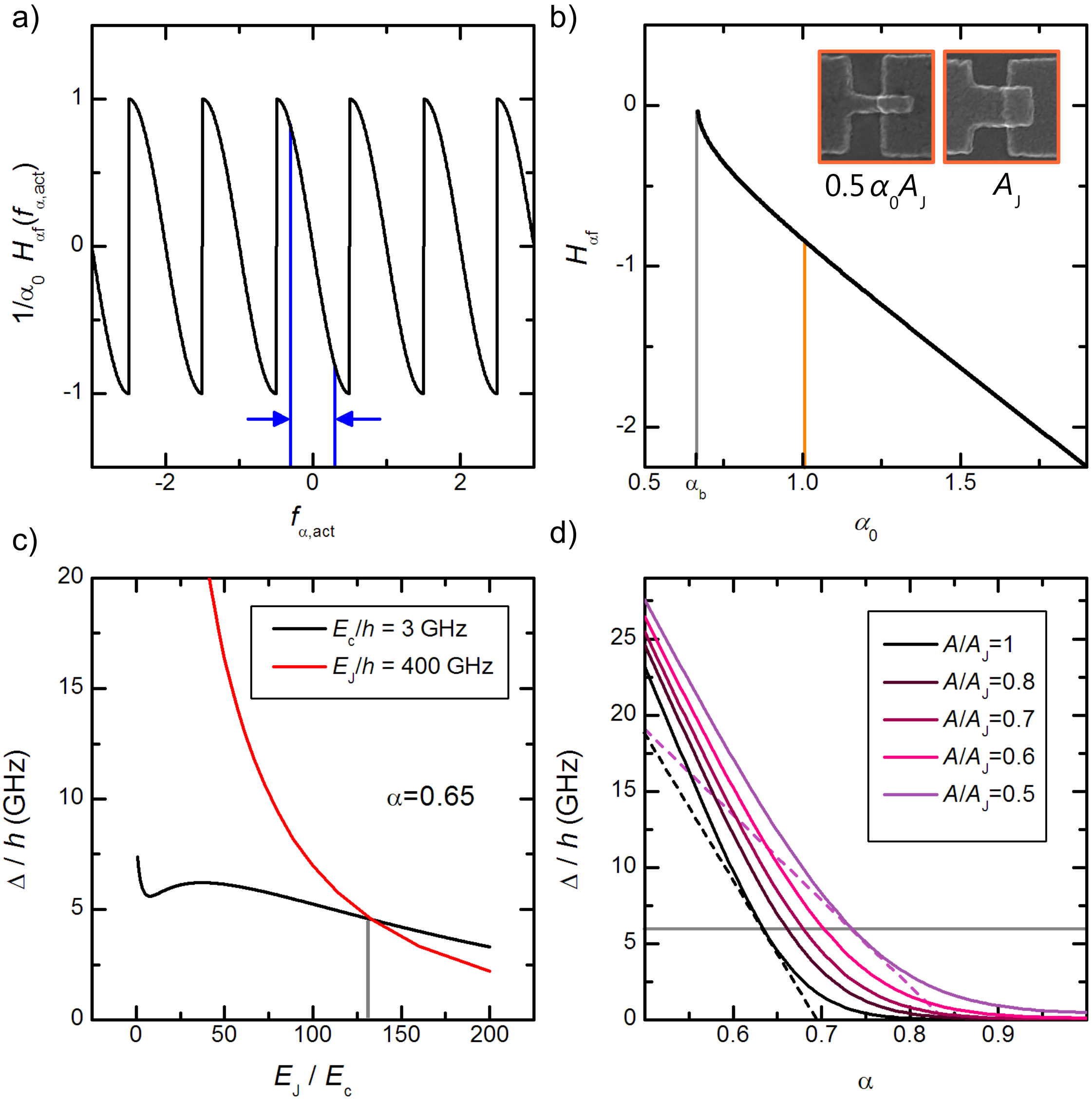

Figure 4.12 – **a)** Normalized sensitivity $H_{\alpha f}(f_{\alpha,\mathrm{act}})$ as a function of external frustration. The qubit measurements presented in this chapter have been performed in the range between the blue lines; **b)** Sensitivity to external frustration $H_{\alpha f}$ as a function of α_0, which is given as twice the ratio of the junction area $A_{\mathrm{J,s}}$ of a SQUID junction to the area $A_{\mathrm{J,q}}$ of one of the larger qubit junctions, cf. SEM images of the qubit junctions in the insets. The value for the qubit characterized in this section is shown as an orange line. The gray line represents the minimal value $\alpha_0 = \alpha_{\mathrm{b}}$; **c)** Simulated minimal transition frequency Δ/h as a function of the ratio $E_{\mathrm{J0}}/E_{\mathrm{c}}$ for $\alpha = 0.65$. For the black curve $E_{\mathrm{J0}}/h = 400\,\mathrm{GHz}$ is kept constant and for the red curve $E_{\mathrm{c}}/h = 3\,\mathrm{GHz}$ is kept constant. The point where both curves intersect belongs to $E_{\mathrm{J0}}/E_{\mathrm{c}} \approx 135$, which is roughly the value of qubits fabricated in this thesis. To reach higher tunnel couplings it is meaningful to rather increase E_{c} than to decrease E_{J0}; **d)** Simulated minimal transition frequency Δ/h as a function of α for qubits with different junction areas A. In these simulations it has been taken into account that a change of A effects both, the charging and the coupling energy. Smaller junction areas result in higher values for Δ but the derivative $\partial\Delta/\partial\alpha$ is decreased for a given working point (dashed lines).

5 Chapter
Summary and outlook

Superconducting qubits and artificial atoms are essential elements in circuit-QED architectures, which are very attractive to perform quantum computations as well as various experiments comparable to optical systems leading even beyond the well known physics in quantum optics [4, 24, 25, 57, 58, 63, 64, 67].
Most circuit-QED experiments are based on the interaction between the quantized modes of a superconducting resonator and an artificial atom. Therefore it is necessary to analyze the physics of artificial atoms in detail and to obtain the ability to control certain properties as for example the tunnel coupling. The commonly used qubit at the WMI is the flux qubit, which has the disadvantage compared to other superconducting qubit types [75, 153] that its minimal transition frequency is fixed during fabrication. To overcome this issue, this thesis focuses on the implementation of a qubit with tunable tunnel coupling.

Two major prerequisites are required in order to realize a gradiometric flux qubit with tunable tunnel coupling, which are operative qubits with finite tunnel coupling in addition to a reliable technique of phase-biasing. Flux qubits are based on superconducting loops intersected by submicron Josephson junctions, which require high current densities and are therefore very demanding to fabricate. At the WMI superconducting systems made of aluminum thin films are used in an well established fabrication process for flux qubits [92, 150]. In the beginnig of this thesis it was important to fabricate and characterize *regular* flux qubits with suitable tunnel coupling before focusing on tuning this coupling. For the integration of a flux qubit into a gradiometer, several phase-biased SQUIDs have been investigated, which gives the basis of the gradiometric layout used in this thesis. Furthermore it was important to prevent on-chip heating, which is highly obstructive when performing measurements at milli-Kelvin temperatures. Along the way to a gap-tunable gradiometric qubit it was a large breakthrough to succesfully fabricate and characterize two gradiometric qubits, even though they were not designed to be tunable. The measurements performed on these qubits were also used to establish a simulation routine which is necessary to extract crucial values as the magnetic energy of a qubit, as well as to simulate the behavior of future fabricated qubits.
As a central result, it was achieved to fabricate and characterize a gradiometric flux qu-

bit with tunable tunnel coupling, which is analyzed in detail concerning tunability. The tunnel coupling of this qubit could be tuned in the range of several GHz using either an external solenoid or an on-chip flux line. Crucial qubit parameters are determined using independent techniques yielding plausible and most notably consistent results. It is demonstrated that the production process at the WMI has reached a reasonable degree of reproducibility.

For future applications of the gradiometric and tunable qubit design it is important to perform time domain measurements and determine the qubit coherence times. Using the readout scheme presented in this thesis, this can be achieved by a detailed analysis of the characteristic peak and dip structures [165] induced by irradiation in the GHz regime. Further, the gradiometric qubit can be coupled to a lumped element resonator and use a pulsed readout technique [11, 162] to observe Rabi oscillations in the time domain [86, 144, 171–173], which can be used to study the qubit coherence properties. The tunable qubit design can be used to increase the coupling strength between qubit and an oscillator to observe exciting phenomena such as vacuum Rabi splitting [20, 22] or Bloch-Siegert shifts [58].
In contrast to SQUID readout techniques, the qubit can also be coupled galvanically to a transmission line resonator in order to perform quantum non demolition measurements [174, 175]. This circuit-QED architecture enables strong coupling between qubit and resonator resulting in phenomena as Rabi oscillations or the ac-Stark shift [70, 78]. Recently the ultrastrong coupling regime, where the Jaynes-Cummings model collapses, has been reached by coupling a flux qubit galvanically via a large area Josephson junction to the transmission line resonator [57]. The tunable qubit can also be used to optimize the coupling strength between qubit and resonator by tuning the qubit in resonance with the tranmission line resonator, which enables tunable ultrastrong coupling.
For flux qubits it is common to be coupled via magnetic energy, i.e. via σ_z rotations in the Bloch-sphere to other systems, which means that qubit-qubit coupling is performed as $\sigma_z\sigma_z$ coupling [76, 77, 80–84]. This coupling scheme in combination with the gradiometric qubit design is a promising candidate for quantum computation as it can be used to perform controlled-NOT quantum gates [91]. The tunable design presented in this thesis allows not only the coupling via σ_z but also a coupling via the energy splitting Δ [84, 86], which allows to demonstrate squeezed cooling [87] as well as simulation of Dirac equations as in trapped ions [88].
As pointed out in the motivation of this thesis, superconducting flux quantum systems can be used in combination with other quantum mechanical ensembles, e.g. optical or semiconductor systems to exploit the advantageous of each system [62, 63]. Recently a tunable flux qubit has been used together with an ensemble of identical, highly 'coherent' quantum spins [25, 64], which is a big step towards systems where superconducting qubits process quantum information and systems with longer coherence times are used to preserve or transfer the information. In this architecture the superconducting qubit is therefore used as the quantum processor whereas the spin ensemble has the role of the quantum memory. This solution is already close to the concept of a classical computer, which clarifies the enormous progress in the prospering field of circuit-QED.

Appendix

A Sample design and fabrication technology

Fabricating and characterizing superconducting flux quantum systems requires a lot of sophisticated technique and much experience to find parameters that result in working systems [92]. Many years of effort have been put into this business in the past at the WMI.

Over the years a well established infrastructure of fabrication techniques such as electron beam lithography (EBL) or aluminum evaporation and measurement skills such as microwave technology or SQUID readout systems have been built up.

All qubits characterized in this work were fabricated with the commonly used production techniques at the WMI, which are described in detail in Ref's. [135, 150, 163, 168, 170, 176]. This section gives a short overview of the fabrication steps and the used fabrication parameters.

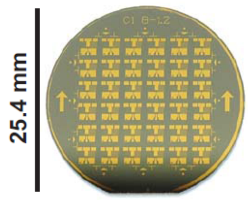

Figure A.1 – 1" silicon wafer with 36 equal gold structures used as contact pads and feed lines for qubit and readout-SQUID[1].

All qubits presented in this thesis are fabricated using an EBL process to define the submicron structures, e.g. Josephson-junctions, and aluminum evaporation to place these structures as aluminum thin films on a silicon wafer. This one inch thermally oxidized silicon wafer with an oxide thickness of 50 nm is a commonly used substrate material for qubit-SQUID systems. Each wafer holds place for 36 qubit-SQUID systems, which are integrated into bias lines and contact pads necessary for a four-point readout of the dc-SQUID (cf. Fig. A.1). These structures are fabricated in a process using optical lithography and sputter deposition of gold. For the wafers in this thesis 5 nm chromium is used as an adhesive layer prior to the deposition of 20 nm gold. The design of contact pads and feed lines is a derivative of the design presented in Ref. [150] & Ref. [163], which can be used in combination with a shunt capacitance of the SQUID as effective RC low-pass filter.

In the scope of finding a solution to the heating issue presented in Sec. 3.6, the contact pads used for ε-line and α-line are covered with aluminum (cf. Fig. A.2c). This is achieved in one fabrication step together with the Josephson-junction devices so that the aluminum cover has a thickness of 90 nm.

[1] This photograph was gratefully taken from Ref. [150]

The qubit design

A first step before fabricating a qubit is to design qubit, readout-SQUID and flux-lines, which can be done with a CAD software[2]. This software can be used to define structures, which are in the end realized as aluminum layers integrated into the feed-line structures fabricated of sputtered gold using optical lithography.
Designing flux qubits, especially gradiometric qubits with tunable tunnel gap allows a lot of engineering freedom. The gradiometric qubits characterized in this work belong to the first qubits of this kind built at the WMI. Therefore one had the freedom of choice how to design qubit, SQUID and flux lines. The qubit layout is inspired by a design used in Ref. [18], whereas the α-SQUID used in this thesis shares no part of its loop with the trap-loop.
The trap-loop area of the design used in this thesis was chosen such that each half has roughly the same area as qubits which are succesfully characterized in Ref. [163]. Flux lines and readout-SQUID are inductively coupled to the qubit and therefore placed as close to the trap-loop as the EBL writing-accuracy allows (cf. Fig. A.2d). Therefore a sufficient mutual inductance between trap-loop on the one hand and flux-lines and SQUID on the other hand is obtained. The inductive coupling is mainly determined by the length of the close-by segment of trap-loop and SQUID/flux-line. As a consequence, it is on the one hand required to increase this length in order to increase the mutual inductance, but on the other hand an increase of this length also enlarges the sensitivity to flux noise. This is due to the fact that increasing the length of close-by segments results in larger areas of SQUID and trap-loop, i.e. in larger sensitivity to flux noise. Another reason to keep the SQUID-are small is to obtain smaller screening factors β_{L}, which is $\beta_{\mathrm{L}} = 2 \cdot 10^{-3}$ for SQUIDs used in this thesis.
For dimensioning α-line and ε-line one has to trade off desirable high couplings against the undesired increase of cross correlations. This is why the ε-line in the design of the tunable qubit is not placed symmetrically beneath the trap-loop but relocated away from the α-loop. Actual areas of trap-loop, SQUID, qubit and α-loop are presented in table A.1.
A further important degree of freedom is the nominal α-value α_0, which is discussed in detail in Sec. 4.3.7. Furthermore, one has the choice to design width and thickness of the aluminum layers which mainly define the kinetic inductance of the loop, cf. (2.1.6), and thus the factor β. The cross-sectional area of the aluminum layers was adapted from the commonly used values at the WMI which are a width of 506 nm and a thickness of (40+50) nm[3]. However, as discussed in Sec. 4.3.7, it can be useful to change these values in order to increase the kinetic inductance of the aluminum layers.

[2] In this thesis the built-in editor of the EBL software is used, which is capable of writing GDS or GDSII files used by the EBL software

[3] Since the aluminum is evaporated in two steps in order to fabricate Josephson-junctions, the total thickness is composed of a 40 nm thick lower layer and a 50 nm thick upper layer.

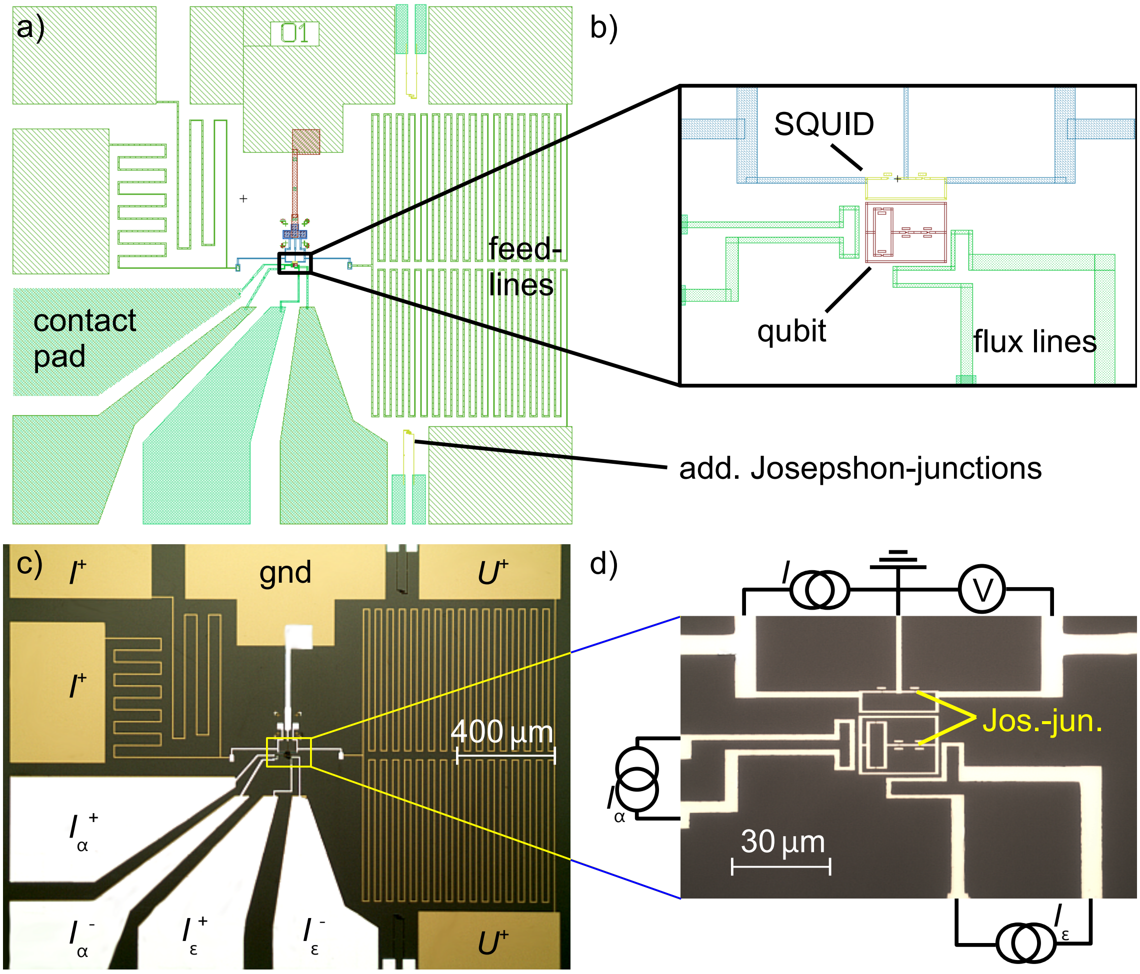

Figure A.2 – **a)** Layout of one sample created with a CAD software, consisting of contact pads, feed lines, readout-SQUID and gradiometric qubit, which is designed to have a tunable tunnel coupling. Additionally, there are structures containing Josephson-junctions for room temperature characterization. Each wafer holds place for 36 of these samples; **b)** Enlarged view of the section in (a) containing qubit, readout-SQUID and flux lines; **c)** Microscope image of a fabricated sample containing contact pads (gold & aluminum), feed- and flux lines as well as readout SQUID and qubit realized as thin aluminum layers on a silicon wafer. The contact pads for α- and ε-line are additionally covered with aluminum to avoid heating effects due to currents in the mA-regime; **d)** Zoom into the aluminum structures of (c). The qubit in the middle is read out inductively by a dc-SQUID which can be contacted for four-point measurements. The flux lines are connected to a dc-current source.

Fabrication steps

All samples used in this thesis have been fabricated in the nano-technology and clean-room facilities of the WMI. Sample fabrication is divided into several steps, which are particularized in Ref. [150]. Each sample presented in this thesis was fabricated with the commonly used techniques at the WMI, which have not been changed with respect to the detailed guidance in Ref. [150]. In the following a short overview of these techniques as well as crucial parameters used for fabrication are given.
With a scanning electron microscope[4] (SEM) patterns of nanometer size can be written in electron beam (EBEAM) resist because of the electrons small de-Broglie wavelength [177]. Two layers of EBEAM resist[5] are deposited on a silicon wafer using a wafer coater, depicted as red and orange structures in Fig. A.4a. The chemical structure of the top layer can be broken by high energy electrons of approximately 30 keV whereas the lower layer is also sensitive to scattered electrons. This allows to write a predetermined pattern very precisely into the top layer whereas the bottom layer is activated in a wide region underneath (cf. Fig. A.4a). In a next step the resist is developed[6], which removes the chemically broken structures while the resist that was not activated by the EBEAM stays on the chip. In this way a free area is caved under a well defined structure.

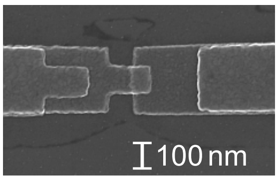

Figure A.3 – Typical Josephson-junction realized in this work.

Having fabricated an on-chip mask of the design created by the CAD software, Josephson-junctions are realized by two steps of aluminum evaporation and an oxidation process in between, cf. Fig. A.4c,d. Under UHV conditions[7] aluminum is evaporated at a certain angle θ through the mask onto the silicon wafer as shown in Fig. A.4b. This procedure maps the designed structure as a thin film of aluminum on the wafer, which is for samples in this thesis 40 nm thick. After this process step, the surface of the aluminum film is oxidized with pure oxygen at a pressure of approximately $2 \cdot 10^{-4}$ mbar for about 25 minutes, yielding an L-product of approximately 0.3 (cf. A.1 for details). Oxidation is a crucial part of qubit fabrication since the junction's current density depends exponentially on the oxide thickness, which cannot be changed afterwards. It takes extensive preliminary investigations to find suitable oxidation parameters[8]. After oxidation is finished, the second aluminum layer is evaporated at an angle $-\theta$ on top of the first oxidized aluminum layer as shown in Fig. A.4c. In this way a well defined overlap of both aluminum layers is accomplished and a Josephson-junctions is realized as shown

4 At the WMI a XL30-SFEG Scanning Electron Microscope from FEI that is equipped with a Raith laser-stage and a Raith Elphy Plus pattern generator for lithography applications is used.

5 The bottom layer consists of a 680 nm thick PMMA/MA 33% copolymer layer and the top layer of an only 70 nm thin PMMA/950k layer.

6 An AllResist AR-P 600-56 developer was used in this thesis.

7 The used aluminum evaporation apparatus is self-made and described in detail in Ref. [168].

8 Unfortunately, leaving oxidation parameters constant for different fabricated wafers produced junctions with strongly different current densities. It turned out that due to an unknown reason the oxidation time had to be increased from 21 minutes in the beginning of this thesis to almost 26 minutes in the end to provide equal current densities

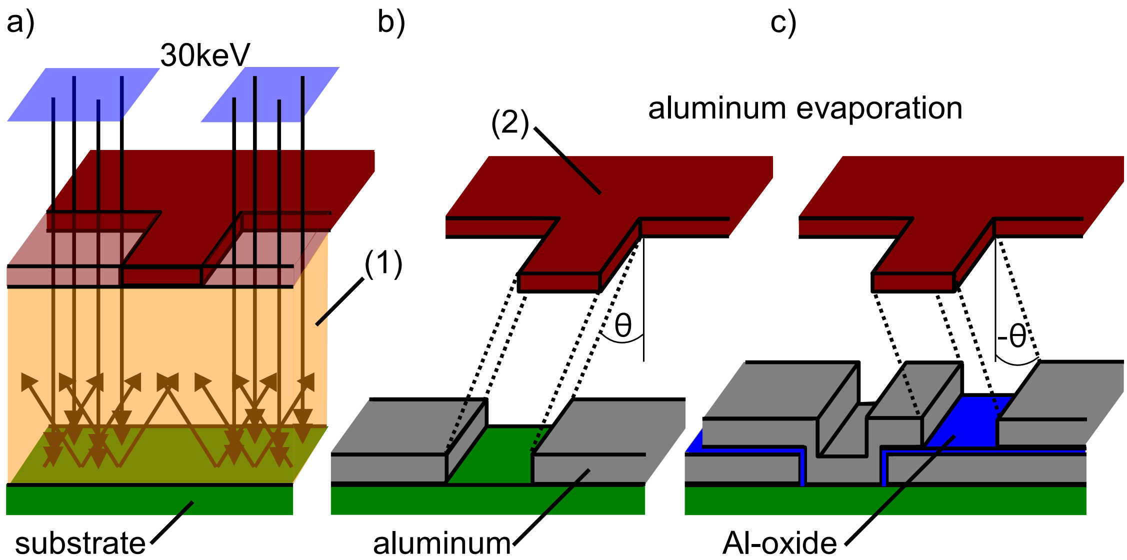

Figure A.4 – Three important steps during sample fabrication: **a)** On top of the silicon substrate (green) a double layer of EBEAM resist is placed (orange & red). The chemical structure of the top layer (1) can be broken by high energy electrons (30 keV), whereas the chemical structure of the lower layer (2) is broken by backscattered electrons, too. Thus, a prior defined structure (blue) can be written in the top layer while there is an undercut in the bottom layer leaving space for the aluminum thin films; **b)** The prior defined structure is mapped in an angle θ onto the wafer as a 40 nm thin film using an aluminum evaporation technique; **c)** After the surface of the first aluminum layer is oxidized, a second layer is evaporated at an angle $-\theta$. Thus, a well defined overlap of both layers can be realized building a Josephson-junction.

in Fig. A.3.
Finally, a lift-off process using acetone at 70 °C is performed to clear away the redundant aluminum. A complete structure of qubit, readout-SQUID and feed-lines is shown in Fig. A.2c, and an enlarged view of qubit, readout-SQUID and flux-lines is shown in Fig. A.2d.
After the fabrication process is finished, all 36 samples are still on one single wafer, which has to be divided up since there is space for only three to four samples in the cryostat. Therefore the chip is broken into 36 pieces of approximately 2.5 mm x 2.5 mm using a wafer cutter[9] to predetermine a breaking point. After a careful optical examination whether the samples are suitable for qubit measurements, promising speciman can be glued to a sample holder. Afterwards SQUID and flux-lines can be contacted using thin aluminum wires[10], cf. Fig. A.5c. At this point samples are fully prepared to be used in experiments, which were either performed in a ^{3}He evaporation cryostat or in a ^{3}He/^{4}He dilution refrigerator.

[9] At the WMI a UNTEMP, Model: RV-129 wafer cutter is used.
[10] At the WMI a manual thin-wire wedge bonder (F & K Delvotec) is used.

Table A.1 – Fabrication parameters as well as sample geometries and qubit properties of the different samples characterized in this thesis.

qubit type	*regular* qubit	*regular* qubit	gradiometric qubit	gradiometric qubit	tunable qubit
label	JG06B32	JG08B09	JG08B20	JGB09B16	JG09B30
specification	$\alpha = 0.75$	$\alpha = 0.60$	$\alpha = 0.77$	$\alpha = 0.65$	
area Jos.-jun [μm^2]	0.031 0.023(α)	0.020 0.012(α)	0.026 0.020(α)	0.027 0.018(α)	0.028 0.014(α)
width Al-layer [nm]	506	506	506	506	506
thickness Al-layer [nm]	(40+50)	(40+50)	(40+50)	(40+50)	(40+50)
trap-loop area [μm^2]	-	-	20 x 15	20 x 15	20 x 15
qubit size [μm^2]	9.5 x 8.5	9.5 x 8.5	20 x 7.5	20 x 7.5	20 x 7.5
SQUID size [μm^2]	12 x 11.8	12 x 11.8	20 x 5	20 x 5	20 x 5
α-SQUID size [μm^2]	-	-	-	-	4.5 x 12
L-product [10^5Pa $\cdot$ s]	0.300	0.305	0.305	0.305	0.305
ox. time [min]	25:45	25:00	25:00	25:40	25:40
j_c [kA/cm^2]	2.73	3.46	3.91	2.91	2.60
R_n [Ω]	175	207	141	183	197
I_c^AB [μA]	0.82	0.69	1.01	0.78	0.73
E_j/h [GHz]	407	344	505	389	362
E_c/h [GHz]	2.70	2.60	3.00	2.92	2.89
Δ/h [GHz]	0 - 1.39	10.76	0 - 0.37	5.1	-

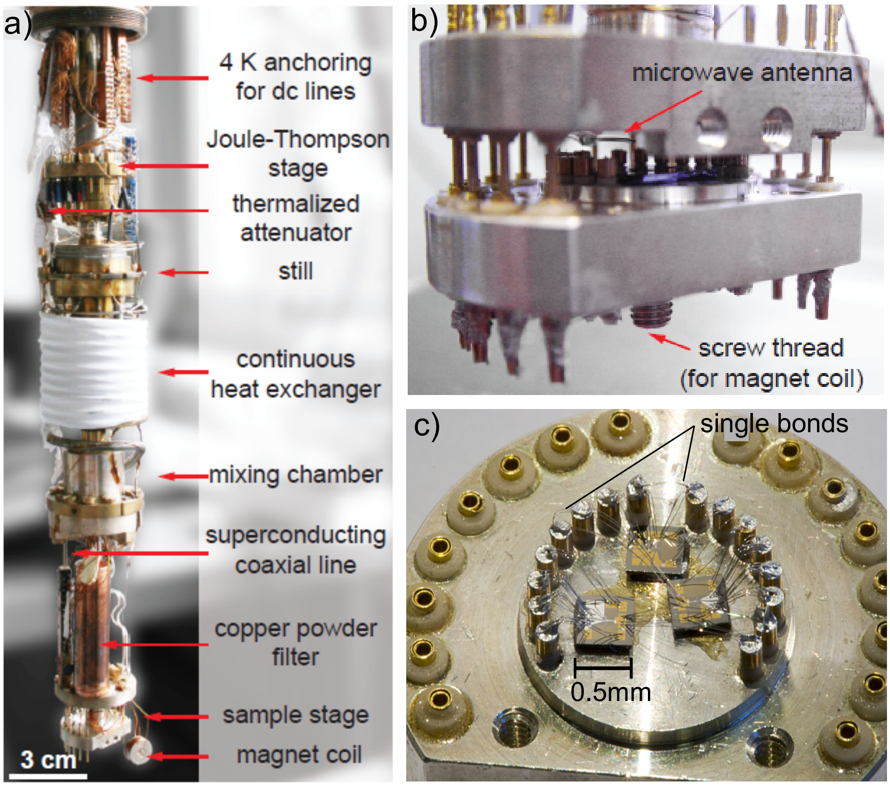

Figure A.5 – ^{3}He/^{4}He-fridge and sample mounting[11]: **a)** Image of the ^{3}He/^{4}He dilution unit used for qubit microwave spectroscopy. Important components of the setup are indicated. A more detailed description of the cryogenic hardware is found in Ref. [151]; **b)** Mounted sample holder. The dismantled end of the superconducting coaxial cable roughly 2mm above the samples serves as microwave antenna; **c)** Three samples prepared for characterization at 35 mK. The samples are bonded by thin aluminum wires and the contact pads are further covered with silver glue for mechanical stability and higher electrical conductivity. Some bronze pins are contacted via a single bond to investigate heating issues described in Sec. 3.6.

B Flux trapping technique

As mentioned before, qubit measurements must be performed at sufficiently low temperatures, i.e. in the milli-Kelvin regime, which is achieved by using a ^{3}He/^{4}He dilution refrigerator. This fridge as well as the ^{3}He evaporation cryostat used for pre-characterization is described in detail in Ref. [150] & Ref. [151] and a general description of cryo-techniques is given in Ref. [178].
In this section a description of the flux trapping technique in the ^{3}He evaporation cryostat, which was used for the phase-biased SQUID measurements at 500 mK, as well as in the ^{3}He/^{4}He dilution refrigerator used for each characterization of the gradiometric qubits is given. To trap an amount of n flux quanta, the aluminum loop has to be heated above

[11] The photographs in Fig. A.5(a) and (b) were gratefully taken from Ref. [150]

its critical temperature $T_c \approx 1.2\,\mathrm{K}$ while it is frustrated by n flux quanta. The magnetic field is in both cryostat induced by the superconducting solenoid that is used to frustrate SQUIDs and qubit during the measurements. The trap-loop frustration is estimated using the frustration of the readout SQUID and the ratio between areas of trap-loop and SQUID.

Flux trapping in the ^{3}He/^{4}He dilution refrigerator

In the dilution refrigerator heating of a sample is achieved by applying a dc-current to the SQUID of a second sample located nearby on the same metallic sample holder, cf. Fig. A.5c. This leaves the SQUID next to the actual trap-loop usable as an indicator whether the aluminum is still superconducting or not. Due to the low thermal conductivity between sample stage and surroundings, this heats up the sample stage stronger than the mixing chamber so that temperatures on the sample stage higher than 1 K can be realized while the mixing chamber is nearly unaffected.
Usually a heating current of about hundred times the SQUIDs critical current is sufficient to reach the normal conducting regime within a few seconds. After switching the heating current off, the temperature will decrease below T_c within seconds and will be back to 35 mK within approx 5-10 minutes.
Using this flux trapping technique, it is not necessary to activate any valves, pumps or heaters, which makes it an elegant way to change the amount of trapped fluxoids in a given geometry. If an additional current source is taken to apply the current through the heating SQUID, it is not even necessary to plug or unplug any measurement or control lines. It should be noted that heating via a second readout-SQUID does not damage the junctions of this SQUID. It was without any problems possible to detect qubit steps with a readout-SQUID that was used several times for the heating process.

Flux trapping in the ^{3}He evaporation refrigerator

In the ^{3}He evaporation fridge the samples have direct contact to the liquid helium bath, so that most heat generated on the sample is absorbed. Therefore heating does not work by applying a dc-current through SQUID junctions. In the ^{3}He fridge samples were heated by recirculating *warm*[12] ^{3}He from a reservoir back to condensed ^{3}He.
In this case the helium pump has to be disconnected so that the pumping line can be used to lead *warm* ^{3}He back to the bath. Already a small amount of *warm* ^{3}He is sufficient to reach a temperature $T > T_c$. In some cases it was already sufficient to use only the ^{3}He stored in the cold trap to reach a temperature above T_c. The transition to the normal conducting state can be directly observed when using a SQUID in the detection mode. After the temperature has increased above T_c, it can be continued pumping on the ^{3}He bath, so that the temperature will be back to 500 mK within about 30 minutes.

[12] At this point *warm* means that the ^{3}He is taken from the reservoir tank, which is located at room temperature.

C Additional measurements

This section contains a detailed description of room temperature measurements on Josephson-junctions and aluminum structures as well as a presentation of further measurements performed on phase-biased SQUIDs as discussed in detail in Sec. 3.4.

Normal resistance of Josephson-junctions

As reaching low temperatures of only some mK is achieved by several steps of pumping, precooling and liquid helium consumption, which takes in most cases more than one day, it is useful to know whether new fabricated samples will be working or not. Unfortunately, there are many steps that can influence the physical properties of Josephson-junctions in an obstructive way so that most importantly these junctions have to probed concerning their physical properties. One crucial value is the junction's current density, which can be estimated via the junctions room temperature resistance R_{rt}. Therefore, a technique to determine the room temperature resistance of Josephson-junction was implemented on every fabricated wafer in this thesis. This was achieved by integrating test structures with Josephson-junctions equally designed as the readout-SQUID junctions on each sample (cf. Fig. A.6a). Even though this method allows a qualitative measurement of the resistance, due to a large spread in the junction's area and difficulties to contact the additional junctions, it turned out to be advantageous to rather make a four-point measurement at the actual readout SQUID. This is mainly because the test structures had to be placed "far" away from the actual SQUIDs on the wafer (cf. Fig. A.2) so that stronger defocusing or stitching errors occured during the SEM writing process. Another reason to rather perform test measurements directly on the readout-SQUID is that these junctions could be short-circuited during fabrication, which cannot be detected by measuring only the test junctions.
To determine the room temperature resistance of a single Josephson-junction, each test structure was fabricated twice: One structure containing Josephson-junctions and one not. This allows to subtract the resistance value of the aluminum layers without junctions from the resistance value with junctions included leaving the value of a pure Josephson-junction: $R_{\mathrm{rt}} = R_{\mathrm{total}} - R_{\mathrm{layer}}$. For the resistance measurements a wafer prober PM5 from Karl Süss was used which has a normal resistance between two needles connected over an aluminum pad of $R_{\mathrm{needle}} \approx 10\,\Omega$. Figure A.6 shows the resistance for several samples which were all fabricated on one wafer. The spreading is within 10%, which gives a reliable resistance value. However, such measurements can only show that additional Josephson-junctions have a suitable resistance but make no statement about the actual readout-SQUID, so that one should more rely on four point measurements on the readout-SQUID.
These four point measurements of the readout-SQUID are performed with the sample holder of the ^{3}He evaporation fridge, which means that the samples have to be prepared equally as for a cool-down. Even though this procedure is more time consuming than resistance measurement of the test structures, the advantage is the direct information on the SQUID junctions. If the resistance values of readout-SQUIDs seem sufficient, i.e. approximately $200\,\Omega$, it is even advantageous since one can directly begin with the

cool-down. The actual measurement was done with a dc-current source, a voltage amplifier and an oscilloscope. Applying a dc-current of less than 1μA is sufficient to read out the voltage drop on the oscilloscope. A normal resistance of approximately $200\,\Omega$ is a suitable value for current densities between 1-2 $\mathrm{kA/cm^2}$ if the junction area is in the order of $0.03\,\mu\mathrm{m}^2$.
One important message, which can be extracted from the four point measurements at readout-SQUIDs is that a SQUID should show at least a resistance of $120\,\Omega$ to work in the superconducting state. All SQUIDs with less than $120\,\Omega$ did not show the typical IVC at 500 mK as in Fig. 3.1 but were short circuited.

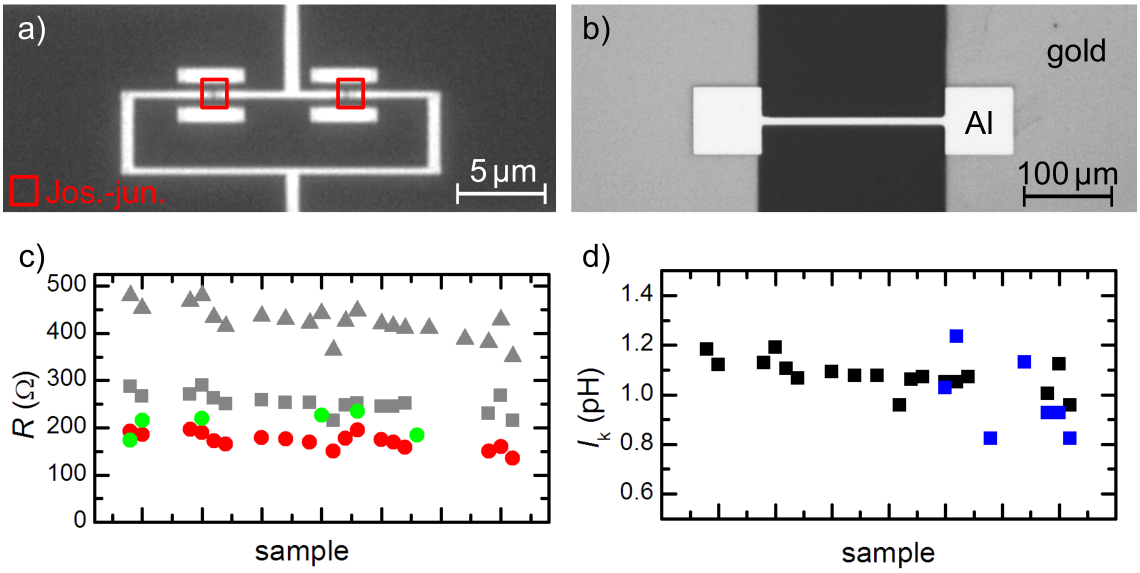

Figure A.6 – **a)** Microscope image of test structures placed on a silicon wafer. Josephson-junctions are surrounded by red squares; **b)** Aluminum strip to determine the specific resistance of the aluminum thin films. The strip is placed between two gold contact pads; **c)** Room temperature resistance of additional structures placed on one exemplary wafer: Gray triangles belong to the resistance of structures containing Josephson-junctions and gray squares belong to identically designed structures with no Josephson.junctions included. Red dots belong to the difference of gray triangles and squares, which can be assumed as the actual room temperature resistance of the Josephson-junctions. Green dots are resistance values of four point measurements at the actual readout-SQUID; **d)** Specific kinetic inductance determined by the room temperature resistance of thin aluminum films like the one shown in (b). Black squares belong to values determined by the structure shown in (b), whereas blue squares belong to the structures taken to determine the gray squares in (c).

Specific kinetic inductance

The specific kinetic inductance l_k used to estimate the ratio β in Sec. 3.4 was determined by room temperature resistance measurements on aluminum thin films like the one shown in Fig. A.6b. Such structures have been placed on several wafers used for qubit fabrication in this thesis. In Fig. A.6d the specific kinetic inductance for different samples placed on one wafer is shown. For the values shown in Fig. A.6c, equation (3.4.5) has been used to calculate the specific inductance. There is a good agreement within the values of different samples, which was reproducible for different wafers. Summarizing all measurements the kinetic inductance was determined to be $l_{\mathrm{k}} = (1.02 \pm 0.14)\,\mathrm{pH}$.

Additional phase-biased SQUID measurements

This section provides additional measurements performed on phase-biased SQUIDs as described in detail in Sec. 3.4. In order to obtain more information about the kinetic and geometric inductance of geometries used in this thesis three phase-biased SQUIDs additional to the ones in Sec. 3.4 have been fabricated and characterized. These samples were designed to have different trap-loop areas and different ratios between shared segment a and total loop circumference s (cf. Fig. A.7 top row). The switching current of these samples is shown in Fig. A.7d together with the switching current of a reference SQUID. In this plot one can clearly recognize the difference in oscillation *frequency* (cf. Sec. 3.4.2). Furthermore, one can observe that the modulation depth is strongly changing with the corresponding size of the trap-loop area. This due to different screening parameters β_{L}, which are proportional to the total inductance of a SQUID. From this plot it can be seen the phase-biased SQUID with the largest trap-loop shows the smallest modulation (red curve), whereas the phase-biased SQUID with smaller trap-loop area modulate stronger (green and blue curve). The reference SQUID shows the typical behavior and modulates down to $I_{\mathrm{sw}} = 0$. In table A.2 the values of all characterized phase-biased SQUIDs in this thesis are summarized.

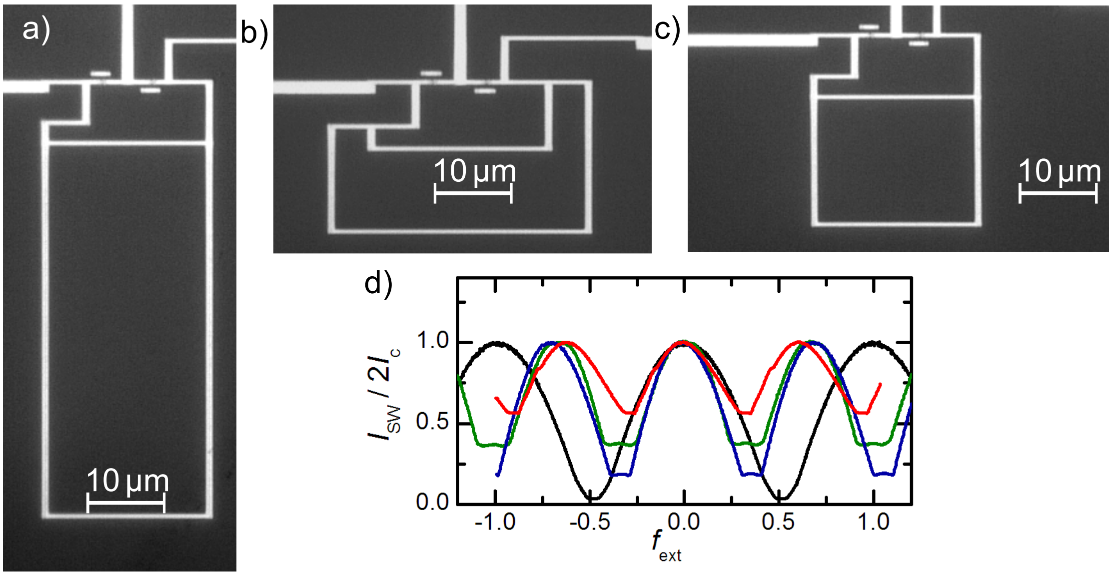

Figure A.7 – **Top row (a-c)** Three designs of phase-biased SQUIDs that have been characterized as described in detail in Sec. 3.4. Trap-loop area and shared segment between trap-loop and SQUID are varied; **d)** Switching current curve of the three phase-biased SQUIDs shown in (a-c) compared to a reference SQUID. Colour code is (a)=red, (b)=green, (c)=blue and the curve of the reference SQUID is plotted in black. Due to the larger loop areas the phase-biased SQUIDs have larger screening factors β_{L} which can be seen by the decreasing modulation depth.

Table A.2 – Measured and calculated values for the different phase-biased SQUIDs. The ratio a/s representing the shared segment a of the total trap-loop circumference is set during fabrication. The values for L_g are calculated and the values for L_k estimated from normal resistance measurements. κ is measured from the phase shift and from the *frequency* change compared to a reference SQUID. For the π and the $\pi/2$-SQUID no such reference SQUID was cooled down so that these values for κ(frequency) are missing. Using the κ-values one can make a consistency-check of the resulting values for M_g.

sample	$\frac{a}{s}$	L_g [pH]	L_k [pH]	β	κ (phase)	κ(frequency)	M_g [pH]
π-SQUID	0.500	11	20	0.550	0.409	-	2.68
$\pi/2$-SQUID	0.250	11	20	0.550	0.230	-	2.13
Fig. A.7a	0.167	170	130	1.308	0.082	0.076	4.61
Fig. A.7b	0.343	79	91	0.868	0.205	0.205	3.64
Fig. A.7c	0.286	57	70	0.814	0.182	0.179	3.37

Bibliography

[1] J. E. Mooij, T. P. Orlando, L. Levitov, L. Tian, C. H. van der Wal, and S. Lloyd. Josephson Persistent-Current Qubit, *Science* **285**, 1036–1039 (1999).

[2] T. P. Orlando, J. E. Mooij, L. Tian, C. H. van der Wal, L. S. Levitov, S. Lloyd, and J. J. Mazo. Superconducting persistent-current qubit, *Phys. Rev. B* **60**, 15398–15413 (1999).

[3] J. Clarke and F. K. Wilhelm. Superconducting quantum bits, *Nature* **453**, 1031–1042 (2008).

[4] F. Nori. Superconducting qubits: Atomic physics with a circuit, *Nat Phys* **4**, 589–590 (2008).

[5] M. H. Devoret, A. Wallraff, and J. M. Martinis. *Superconducting Qubits: A Short Review*, 2004.

[6] G. Wendin and V. S. Shumeiko. Quantum bits with Josephson junctions (Review Article), *Low Temperature Physics* **33**, 724–744 (2007).

[7] C. Cohen-Tannoudji, B. Diu, and F. Laloe. Quantum Mechanics. Quantum Mechanics. John Wiley & Sons, 2006.

[8] M. A. Nielsen and I. L. Chuang. Quantum Computation and Quantum Information (Cambridge Series on Information and the Natural Sciences). 1st ed. Cambridge University Press, 2004.

[9] A. Zagoskin and A. Blais. Superconducting qubits, *Science* **296**, 215–227 (2008).

[10] F. Yoshihara, K. Harrabi, A. O. Niskanen, Y. Nakamura, and J. S. Tsai. Decoherence of Flux Qubits due to $1/f$ Flux Noise, *Phys. Rev. Lett.* **97**, 167001 (2006).

[11] K. Kakuyanagi, T. Meno, S. Saito, H. Nakano, K. Semba, H. Takayanagi, F. Deppe, and A. Shnirman. Dephasing of a Superconducting Flux Qubit, *Phys. Rev. Lett.* **98**, 047004 (2007).

[12] R. H. Koch, D. P. DiVincenzo, and J. Clarke. Model for $1/f$ Flux Noise in SQUIDs and Qubits, *Phys. Rev. Lett.* **98**, 267003 (2007).

[13] R. Harris, M. W. Johnson, S. Han, A. J. Berkley, J. Johansson, P. Bunyk, E. Ladizinsky, S. Govorkov, M. C. Thom, S. Uchaikin, B. Bumble, A. Fung, A. Kaul, A. Kleinsasser, M. H. S. Amin, and D. V. Averin. Probing Noise in Flux Qubits via Macroscopic Resonant Tunneling, *Phys. Rev. Lett.* **101**, 117003 (2008).

[14] A. Ferrón and D. Domínguez. Intrinsic leakage of the Josephson flux qubit and breakdown of the two-level approximation for strong driving, *Phys. Rev. B* **81**, 104505 (2010).

[15] F. Chiarello, P. Carelli, M. G. Castellano, C. Cosmelli, L. Gangemi, R. Leoni, S. Poletto, D. Simeone, and G. Torrioli. Superconducting tunable flux qubit with direct readout scheme, *Superconductor Science and Technology* **18**, 1370 (2005).

[16] A. O. Niskanen, Y. Nakamura, and J.-S. Tsai. Tunable coupling scheme for flux qubits at the optimal point, *Phys. Rev. B* **73**, 094506 (2006).

[17] S Poletto, F Chiarello, M. G. Castellano, J Lisenfeld, A Lukashenko, C Cosmelli, G Torrioli, P Carelli, and A. V. Ustinov. Coherent oscillations in a superconducting tunable flux qubit manipulated without microwaves, *New Journal of Physics* **11**, 013009 (2009).

[18] F. Paauw. „Superconducting flux qubits: Quantum chains and tunable qubits“. PhD thesis. TU Delft, 2009.

[19] X. Zhu, A. Kemp, S. Saito, and K. Semba. Coherent operation of a gap-tunable flux qubit, *APL* **97**, 102503 (2010).

[20] A. Fedorov, A. K. Feofanov, P. Macha, P. Forn-D´, C. J. P. M. Harmans, and J. E. Mooij. Strong Coupling of a Quantum Oscillator to a Flux Qubit at Its Symmetry Point, *Phys. Rev. Lett.* **105**, 060503 (2010).

[21] Y. Shimazu. Tunability of Excited-State Energy Levels of Four-Josephson-Junction Circuit in Crossover from Double-Well to Single-Well Potential, *Journal of the Physical Society of Japan* **80**, 054701 (2011).

[22] A. Fedorov, P. Macha, A. K. Feofanov, C. J. P. M. Harmans, and J. E. Mooij. Tuned Transition from Quantum to Classical for Macroscopic Quantum States, *Phys. Rev. Lett.* **106**, 170404 (2011).

[23] B. Peropadre, P. Forn-D´, E. Solano, and J. J. Garc´-Ripoll. Switchable Ultrastrong Coupling in Circuit QED, *Phys. Rev. Lett.* **105**, 023601 (2010).

[24] X. Zhu, S. Saito, A. Kemp, K. Kakuyanagi, S.-i. Karimoto, H. Nakano, W. J. Munro, Y. Tokura, M. S. Everitt, K. Nemoto, M. Kasu, N. Mizuochi, and K. Semba. Coherent coupling of a superconducting flux qubit to an electron spin ensemble in diamond, *Nature* **478**, 221–224 (2011).

[25] X. Zhu, S. Saito, A. Kemp, K. Kakuyanagi, S.-i. Karimoto, H. Nakano, W. J. Munro, Y. Tokura, M. S. Everitt, K. Nemoto, M. Kasu, N. Mizuochi, and K. Semba. Coherent coupling of a superconducting flux qubit to an electron spin ensemble in diamond, *Nature* **478**, 221–224 (2011).

[26] D. Deutsch. Quantum Theory, the Church-Turing Principle and the Universal Quantum Computer, *Proceedings of the Royal Society of London. A. Mathematical and Physical Sciences* **400**, 97–117 (1985).

[27] L. K. Grover. Quantum Mechanics Helps in Searching for a Needle in a Haystack, *Phys. Rev. Lett.* **79**, 325–328 (1997).

[28] P. Shor. Polynomial-Time Algorithms for Prime Factorization and Discrete Logarithms on a Quantum Computer, *SIAM J. Comp.* **26**, 1484 (1997).

[29] R. Beals, H. Buhrmann, R. Cleve, M. Mosca, and R. de Wolf. Quantum lower bounds by polynomials, *IEEE, Proc. of the 39th Annual Symposium on the Foundations of Computer Science* . 352 (1998).

[30] Y Ozhigov. „Quantum Computer cannot speed up iterated applications of a black box“. PhD thesis. University of Amsterdam, 1999.

[31] R. Feynman. Simulating physics with computers, *International Journal of Theoretical Physics* **21**, 467–488 (1982).

[32] C. H. Bennett and G. Brassard. Quantum cryptography: Public key distribution and coin tossing. In: *Proceedings of IEEE International Conference on Computers Systems and Signal Processing.* Vol. 175. Bangalore, India, 1984, 175–179.

[33] A. K. Ekert. Quantum cryptography based on Bell's theorem, *Phys. Rev. Lett.* **67**, 661–663 (1991).

[34] P. W. Shor. Scheme for reducing decoherence in quantum computer memory, *Phys. Rev. A* **52**, R2493–R2496 (1995).

[35] A. M. Steane. Error Correcting Codes in Quantum Theory, *Phys. Rev. Lett.* **77**, 793–797 (1996).

[36] T. Beth and G. Leuchs. Quantum information processing. Wiley-VCH, 2005.

[37] D. P. DiVincenzo. *The Physical Implementation of Quantum Computation*, 2000.

[38] J. I. Cirac and P. Zoller. Quantum Computations with Cold Trapped Ions, *Phys. Rev. Lett.* **74**, 4091–4094 (1995).

[39] C. Monroe, D. M. Meekhof, B. E. King, W. M. Itano, and D. J. Wineland. Demonstration of a Fundamental Quantum Logic Gate, *Phys. Rev. Lett.* **75**, 4714–4717 (1995).

[40] H. Haeffner, W. Haensel, C. F. Roos, J. Benhelm, D. C. al kar, M. Chwalla, T. Koerber, U. D. Rapol, M. Riebe, P. O. Schmidt, C. Becher, O. Guhne, W. Dur, and R. Blatt. Scalable multi-particle entanglement of trapped ions, *NATURE* **438**, 643 (2005).

[41] H. Haeffner, C. F. Roos, and R. Blatt. Quantum computing with trapped ions, *Physics Reports* **469**, 155 (2008).

[42] Q. A. Turchette, C. J. Hood, W. Lange, H. Mabuchi, and H. J. Kimble. Measurement of Conditional Phase Shifts for Quantum Logic, *Phys. Rev. Lett.* **75**, 4710–4713 (1995).

[43] D. Bouwmeester, J.-W. Pan, K. Mattle, M. Eibl, W. Harald, and Z. Anton. Experimental quantum teleportation, *Nature* **390**, 575–579 (1997).

[44] L. M. K. Vandersypen, M. Steffen, B. Gregory, C. S. Yannoni, M. H. Sherwood, and I. L. Chuang. Experimental realization of Shor's quantum factoring algorithm using nuclear magnetic resonance, *Nature* **414**, 883–887 (2001).

[45] I. L. Chuang, L. M. K. Vandersypen, X. Zhou, D. W. Leung, and S. Lloyd. Experimental realization of a quantum algorithm, *Nature* **393**, 143–146 (1998).

[46] R. Vrijen, E. Yablonovitch, K. Wang, H. W. Jiang, A. Balandin, V. Roychowdhury, T. Mor, and D. DiVincenzo. Electron-spin-resonance transistors for quantum computing in silicon-germanium heterostructures, *Phys. Rev. A* **62**, 012306 (2000).

[47] M. S. Sherwin, A. Imamoglu, and T. Montroy. Quantum computation with quantum dots and terahertz cavity quantum electrodynamics, *Phys. Rev. A* **60**, 3508+ (1999).

[48] C. J. Hood, T. W. Lynn, A. C. Doherty, A. S. Parkins, and H. J. Kimble. The Atom-Cavity Microscope: Single Atoms Bound in Orbit by Single Photons, *Science* **287**, 1447–1453 (2000).

[49] J. M. Raimond, M. Brune, and S. Haroche. Manipulating quantum entanglement with atoms and photons in a cavity, *Rev. Mod. Phys.* **73**, 565–582 (2001).

[50] A. Shnirman, G. Schön, and Z. Hermon. Quantum Manipulations of Small Josephson Junctions, *Phys. Rev. Lett.* **79**, 2371–2374 (1997).

[51] D. V. Averin. Adiabatic quantum computation with Cooper pairs, *Solid State Communications* **105**, 659 –664 (1998).

[52] J. M. Martinis, S. Nam, J. Aumentado, and C. Urbina. Rabi Oscillations in a Large Josephson-Junction Qubit, *Phys. Rev. Lett.* **89**, 117901 (2002).

[53] Y. Yu, S. Han, X. Chu, S.-I. Chu, and Z. Wang. Coherent Temporal Oscillations of Macroscopic Quantum States in a Josephson Junction, *Science* **296**, 889–892 (2002).

[54] V. Bouchiat, D. Vion, P. Joyez, D. Esteve, and M. H. Devoret. Quantum coherence with a single Cooper pair, *Physica Scripta* **1998**, 165 (1998).

[55] Y. Nakamura, Y. Pashkin, and J. S. Tsai. Coherent control of macroscopic quantum states in a single-Cooper-pair box, *Nature* **398**, 786–788 (1999).

[56] C. H. van der Wal, A. C. J. ter Haar, F. K. Wilhelm, R. N. Schouten, C. J. P. M. Harmans, T. P. Orlando, S. Lloyd, and J. E. Mooij. Quantum Superposition of Macroscopic Persistent-Current States, *Science* **290**, 773–777 (2000).

[57] T. Niemczyk, F. Deppe, H. Huebl, E. P. Menzel, F. Hocke, M. J. Schwarz, J. J. Garcia-Ripoll, D. Zueco, T. Hummer, E. Solano, A. Marx, and R. Gross. Circuit quantum electrodynamics in the ultrastrong-coupling regime, *Nat Phys* **6**, 772–776 (2010).

[58] P. Forn-Diaz, J. Lisenfeld, D. Marcos, J. J. Garcia-Ripoll, E. Solano, C. J. P. M. Harmans, and J. E. Mooij. Observation of the Bloch-Siegert Shift in a Qubit-Oscillator System in the Ultrastrong Coupling Regime, *Phys. Rev. Lett.* **105**, 237001 (2010).

[59] M. Hofheinz, H. Wang, M. Ansmann, R. C. Bialczak, E. Lucero, M. Neeley, A. D. O'Connell, D. Sank, J. Wenner, J. M. Martinis, and A. N. Cleland. Synthesizing arbitrary quantum states in a superconducting resonator, *Nature* **459**, 546–549 (2009).

[60] M. Hofheinz, E. M. Weig, M. Ansmann, R. C. Bialczak, E. Lucero, M. Neeley, A. D. O/'Connell, H. Wang, J. M. Martinis, and A. N. Cleland. Generation of Fock states in a superconducting quantum circuit, *Nature* **454**, 310–314 (2008).

[61] Y. Nakamura. Quantum physics: Tailor-made quantum states, *Nature* **459**, 516–517 (2009).

[62] M Wallquist, K Hammerer, P Rabl, M Lukin, and P Zoller. Hybrid quantum devices and quantum engineering, *Physica Scripta* **2009**, 014001 (2009).

[63] M. Blencowe. Quantum computing: Quantum RAM, *Nature* **468**, 44–45 (2010).

[64] I. Chiorescu. Quantum engineering: Spins coupled to a persistent current, *Nature* **478**, 195–196 (2011).

[65] T. Inoshita, S. Ohnishi, and A. Oshiyama. Electronic Structure of the Superatom: A Quasiatomic System Based on a Semiconductor Heterostructure, *Phys. Rev. Lett.* **57**, 2560–2563 (1986).

[66] V. N. Golovach and D. Loss. Electron spins in artificial atoms and molecules for quantum computing, *Semiconductor Science and Technology* **17**, 355 (2002).

[67] A Wallraff, D. I. Schuster, A Blais, L Frunzio, J Majer, S Kumar, S. M. Girvin, and R. J. Schoelkopf. Strong coupling of a single photon to a superconducting qubit using circuit quantum electrodynamics, *Nature* **431**, 0–5 (2004).

[68] A. Blais, R.-S. Huang, A. Wallraff, S. M. Girvin, and R. J. Schoelkopf. Cavity quantum electrodynamics for superconducting electrical circuits: An architecture for quantum computation, *Phys. Rev. A* **69**, 062320 (2004).

[69] M. Grajcar, S. H. W. van der Ploeg, A. Izmalkov, E. Il/'ichev, H.-G. Meyer, A. Fedorov, A. Shnirman, and G. Schon. Sisyphus cooling and amplification by a superconducting qubit, *Nat Phys* **4**, 612–616 (2008).

[70] A. A. Abdumalikov, O. Astafiev, Y. Nakamura, Y. A. Pashkin, and J. Tsai. Vacuum Rabi splitting due to strong coupling of a flux qubit and a coplanar-waveguide resonator, *Phys. Rev. B* **78**, 180502 (2008).

[71] A. A. Abdumalikov, O. Astafiev, A. M. Zagoskin, Y. A. Pashkin, Y. Nakamura, and J. S. Tsai. Electromagnetically Induced Transparency on a Single Artificial Atom, *Phys. Rev. Lett.* **104**, 193601 (2010).

[72] O. Astafiev, K. Inomata, A. O. Niskanen, T. Yamamoto, Y. A. Pashkin, Y. Nakamura, and J. S. Tsai. Single artificial-atom lasing, *Nature* **449**, 588–590 (2007).

[73] J. M. Chow, A. D. Córcoles, J. M. Gambetta, C. Rigetti, B. R. Johnson, J. A. Smolin, J. R. Rozen, G. A. Keefe, M. B. Rothwell, M. B. Ketchen, and M. Steffen. Simple All-Microwave Entangling Gate for Fixed-Frequency Superconducting Qubits, *Phys. Rev. Lett.* **107**, 080502 (2011).

[74] F. Deppe, M. Mariantoni, E. P. Menzel, A. Marx, S. Saito, K. Kakuyanagi, H. Tanaka, T. Meno, K. Semba, H. Takayanagi, E. Solano, and R. Gross. Two-photon probe of the Jaynes-Cummings model and symmetry breaking in circuit QED, *NATURE PHYSICS* **4**, 686 (2008).

[75] A. A. Houck, J. A. Schreier, B. R. Johnson, J. M. Chow, J. Koch, J. M. Gambetta, D. I. Schuster, L. Frunzio, M. H. Devoret, S. M. Girvin, and R. J. Schoelkopf. Controlling the Spontaneous Emission of a Superconducting Transmon Qubit, *Phys. Rev. Lett.* **101**, 080502 (2008).

[76] J. Majer, J. M. Chow, J. M. Gambetta, J. Koch, B. R. Johnson, J. A. Schreier, L. Frunzio, D. I. Schuster, A. A. Houck, A. Wallraff, A. Blais, M. H. Devoret, S. M. Girvin, and R. J. Schoelkopf. Coupling superconducting qubits via a cavity bus, *Nature* **449**, 443–447 (2007).

[77] A. O. Niskanen, K. Harrabi, F. Yoshihara, Y. Nakamura, S. Lloyd, and J. S. Tsai. Quantum Coherent Tunable Coupling of Superconducting Qubits, *Science* **316**, 723–726 (2007).

[78] D. I. Schuster, A. Wallraff, A. Blais, L. Frunzio, R.-S. Huang, J. Majer, S. M. Girvin, and R. J. Schoelkopf. ac Stark Shift and Dephasing of a Superconducting Qubit Strongly Coupled to a Cavity Field, *Phys. Rev. Lett.* **94**, 123602 (2005).

[79] J. Q. You, Y.-x. Liu, and F. Nori. Simultaneous Cooling of an Artificial Atom and Its Neighboring Quantum System, *Phys. Rev. Lett.* **100**, 047001 (2008).

[80] A. Blais, A. M. van den Brink, and A. M. Zagoskin. Tunable Coupling of Superconducting Qubits, *Phys. Rev. Lett.* **90**, 127901 (2003).

[81] J. B. Majer, F. G. Paauw, A. C. J. ter Haar, C. J. P. M. Harmans, and J. E. Mooij. Spectroscopy on Two Coupled Superconducting Flux Qubits, *Phys. Rev. Lett.* **94**, 090501 (2005).

[82] T. Hime, P. A. Reichardt, B. L. T. Plourde, T. L. Robertson, C.-E. Wu, A. V. Ustinov, and J. Clarke. Solid-State Qubits with Current-Controlled Coupling, *Science* **314**, 1427–1429 (2006).

[83] S. H. W. van der Ploeg, A. Izmalkov, A. M. van den Brink, U. Hübner, M. Grajcar, E. Il'ichev, H.-G. Meyer, and A. M. Zagoskin. Controllable Coupling of Superconducting Flux Qubits, *Phys. Rev. Lett.* **98**, 057004 (2007).

[84] A. J. Kerman and W. D. Oliver. High-Fidelity Quantum Operations on Superconducting Qubits in the Presence of Noise, *Phys. Rev. Lett.* **101**, 070501 (2008).

[85] S. J. Srinivasan, A. J. Hoffman, J. M. Gambetta, and A. A. Houck. Tunable Coupling in Circuit Quantum Electrodynamics Using a Superconducting Charge Qubit with a V-Shaped Energy Level Diagram, *Phys. Rev. Lett.* **106**, 083601 (2011).

[86] F. G. Paauw, A. Fedorov, C. J. P. M Harmans, and J. E. Mooij. Tuning the Gap of a Superconducting Flux Qubit, *Phys. Rev. Lett.* **102**, 090501 (2009).

[87] F Deppe. private communication,

[88] R. Gerritsma, G. Kirchmair, F. Zahringer, E. Solano, R. Blatt, and C. F. Roos. Quantum simulation of the Dirac equation, *Nature* **463**, 68–71 (2010).

[89] C. E. Wu, Y Liu, and C. C. Chi. The gradiometer flux qubit without an external flux bias, *Superconductor Science and Technology* **19**, 280 (2006).

[90] J. Plantenberg. „Coupled superconducting flux qubits“. PhD thesis. TU Delft, 2007.

[91] J. H. Plantenberg, P. C. de Groot, C. J. P. M. Harmans, and J. E. Mooij. Demonstration of controlled-NOT quantum gates on a pair of superconducting quantum bits, *Nature* **447**, 836–839 (2007).

[92] T Niemczyk, F Deppe, M Mariantoni, E. P. Menzel, E Hoffmann, G Wild, L Eggenstein, A Marx, and R Gross. Fabrication technology of and symmetry breaking in superconducting quantum circuits, *Superconductor Science and Technology* **22**, 034009 (2009).

[93] J. F. Cochran and D. E. Mapother. Superconducting Transition in Aluminum, *Phys. Rev.* **111**, 132–142 (1958).

[94] J. Bardeen, L. Cooper, and S. J.R. Theory of superconductivity, *Phys. Rev.* **108**, 1157–1204 (1957).

[95] L. N. Cooper. Bound Electron Pairs in a Degenerate Fermi Gas, *Phys. Rev.* **104**, 1189–1190 (1956).

[96] A. Taylor. WAVE EQUATION FOR THE MACROSCOPIC WAVE FUNCTION IN SUPERCONDUCTORS, *J. Phys., C (London)* **L52**, 5 (1970).

[97] W. Buckel and R. Kleiner. Supraleitung. Ed. by Berlin. Wiley-VCH, 2004.

[98] D. Einzel. 50 Years of Fluxoid Quantization: 2e or Not 2e, *Journal of Low Temperature Physics* **163**, 215–237 (2011).

[99] F. London. Superfluids. Ed. by N. York. John Wiley & Sons, 1950.

[100] R. Doll and M. Näbauer. Experimental proof of magnetic flux quantization in a superconducting ring, *Phys. Rev. Lett.* **7**, 51–52 (1961).

[101] B. S. Deaver and W. M. Fairbank. Experimental Evidence for quantized flux in superconducting cylinders, *Phys. Rev. Lett.* **7**, 43–46 (1961).

[102] M. Tinkham. Introduction to superconductivity. McGraw-Hill, 1975.

[103] R Gross. Lecture Notes of Prof. Gross and Dr. Marx to the Lecture on "Applied Superconductivity". 2010.

[104] Y. Shimanzu and T. Yokoyama. Measurement of kinetic inductance of superconducting wires and application for measuring flux state of Josephson-junction loops, *Physica C* **412-414**, 1451–1454 (2003).

[105] T. Orlando. Foundations of Applied Suprconductivity. Addison-Wesley, 1991.

[106] J. Majer, J. Butcher, and J. Mooij. Simple phase bias for superconducting circuits, *App. Phys. Lett.* **80**, 3638 –3640 (2002).

[107] C. N. Lau, N. Markovic, M. Bockrath, A. Bezryadin, and M. Tinkham. Quantum Phase Slips in Superconducting Nanowires, *Phys. Rev. Lett.* **87**, 217003 (2001).

[108] J. E. Mooij and C. J. P. M. Harmans. Phase-slip flux qubits, *New Journal of Physics* **7**, 219 (2005).

[109] D. E. McCumber and B. I. Halperin. Time Scale of Intrinsic Resistive Fluctuations in Thin Superconducting Wires, *Phys. Rev. B* **1**, 1054–1070 (1970).

[110] B. Josephson. Possible new effects in superconductive tunnelling, *Phys. Rev. Lett.* **1**, 251–253 (1962).

[111] W. Anderson and J. Rowell. Probable Observation of the Josephson Superconducting Tunneling Effect, *Phys. Rev. Lett.* **10**, 230–232 (1963).

[112] S. L. C. U. Goeteborg. *B. D. Josephson - for his theoretical predictions of the properties of a supercurrent through a tunnel barrier, in particular those phenomena which are generally known as the Josephson effects*, Nobel Lecture Series. 1992. URL: `nobelprize.org/nobel_organizations/nobelfoundation/publications/lectures/WSC/phy-71-80.html`.

[113] J. M. Martinis, M. H. Devoret, and J. Clarke. Energy-Level Quantization in the Zero-Voltage State of a Current-Biased Josephson Junction, *Phys. Rev. Lett.* **55**, 1543–1546 (1985).

[114] M. H. Devoret, J. M. Martinis, and J. Clarke. Measurements of Macroscopic Quantum Tunneling out of the Zero-Voltage State of a Current-Biased Josephson Junction, *Phys. Rev. Lett.* **55**, 1908–1911 (1985).

[115] H. Michael, R. Gil, F. M. P. A., and G. P. M. Fate of the Josephson effect in thin-film superconductors, *Nat Phys* **1**, 117–121 (2005).

[116] C. W. J. Beenakker. Universal limit of critical-current fluctuations in mesoscopic Josephson junctions, *Phys. Rev. Lett.* **67**, 3836–3839 (1991).

[117] I. Giaever. Energy Gap in Superconductors Measured by Electron Tunneling, *Phys. Rev. Lett.* **5**, 147–148 (1960).

[118] C. Stewart. Current-Voltage Characteristics of Josephson-Junctions, *App. Phys. Lett.* **12**, 277 (1968).

[119] W. C. Stewart. CURRENT-VOLTAGE CHARACTERISTICS OF JOSEPHSON JUNCTIONS, *Jou* **12**, 277–280 (1968).

[120] V. Ambegaokar and A. Baratoff. Tunneling between superconductors, *Phys. Rev. Lett.* **10**, 486–489 (1963).

[121] R. Eck, D. Scalapino, and B. Taylor. Self-Detection of the ac Josephson Current, *Phys. Rev. L* **13**, 15–18 (1964).

[122] M. Fiske. Temperature and Magnetic Field Dependences of the Josephson Tunneling Current, *Rev. Mod. Phys.* **36**, 221–222 (1964).

[123] S. Shapiro and A. D. Little. Josephson Currents in Superconducting Tunneling: The Effect of Microwaves and Other Observations, *Phys. Rev. Lett.* **11**, 80–82 (1963).

[124] D. E. McCumber. Effect of ac Impedance on dc Voltage?Current Characteristics of Superconductor Weak?Link Junctions,**39**, 3113–3118 (1968).

[125] D. Mc Cumber. Effect of ac Impedance on dc Voltage-Current Characteristics of Superconductor Weak-Link Junctions, *J. App. Phys.* **39**, 3113 (1968).

[126] J Clarke and A. I. Braginski. The SQUID Handbook. Vol. 1, Fundamentals and Technology of SQUIDS and SQUID Systems. Vol. 1. Wiley-VCH, 2004, 653.

[127] V. J. Waal, P. Schrijner, and R. Llurba. Simulation and optimization of a dc SQUID with finite capacitance, *Journal of Low Temperature Physics* **54**, 215–232 (1984).

[128] D. Drung, C. Assmann, J. Beyer, A. Kirste, M. Peters, F. Ruede, and T. Schurig. Highly Sensitive and Easy-to-Use SQUID Sensors, *Applied Superconductivity, IEEE Transactions on* **17**, 699 –704 (2007).

[129] B. L. T. Plourde, T. L. Robertson, P. A. Reichardt, T. Hime, S. Linzen, C.-E. Wu, and J. Clarke. Flux qubits and readout device with two independent flux lines, *Phys. Rev. B* **72**, 060506 (2005).

[130] J. Clarke, W. M. Goubau, and M. B. Ketchen. Tunnel junction dc SQUID: Fabrication, operation, and performance, *Journal of Low Temperature Physics* **25**, 99–144 (1976).

[131] F. Deppe. „Superconducting flux quantum circuits: characterization, quantum coherence and controlled symmetrie breaking“. PhD thesis. Technische Universität München, 2009.

[132] C. H. van derWal. „Quantum Superpositions of Persistent Josephson Currents“. PhD thesis. TU Delft, 2001.

[133] G. Schön and A. Zaikin. Distinguishing Phases in Josephson Junctions and the Choice of States, *Physica B* **152**, 203–206 (1988).

[134] X. Tan, S. Cong, C. Pan, Y. Yu, G. Sun, J. Chen, and P. Wu. Phase-Diffusion in Switching Process of Underdamped Josephson Junctions, *Applied Superconductivity, IEEE Transactions on* **21**, 436 –439 (2011).

[135] M. Goeppl. „Quantenelektronik mit supraleitenden Bauelementen - Herstellung und Charakterisierung von Fluss-Qubits“. MA thesis. TU München, 2006.

[136] C. M. Falco, W. H. Parker, S. E. Trullinger, and P. K. Hansma. Effect of thermal noise on current-voltage characteristics of Josephson junctions, *Phys. Rev. B* **10**, 1865–1873 (1974).

[137] W. C. Scott. HYSTERESIS IN THE dc SWITCHING CHARACTERISTICS OF JOSEPHSON JUNCTIONS, *Applied Physics Letters* **17**, 166–169 (1970).

[138] M. Odyniec and L. Chua. Josephson-junction circuit analysis via integral manifolds, *Circuits and Systems, IEEE Transactions on* **30**, 308 –320 (1983).

[139] M. Odyniec and L. Chua. Josephson-junction circuit analysis via integral manifolds-Part II, *Circuits and Systems, IEEE Transactions on* **32**, 34 –45 (1985).

[140] H. H. Zappe. Minimum current and related topics in Josephson tunnel junction devices, *Journal of Applied Physics* **44**, 1371 –1377 (1973).

[141] F. Deppe, S. Saito, H. Tanaka, and H. Takayanagi. Determination of the capacitance of nm scale Josephson junctions, *Journal of Applied Physics* **95**, 2607–2613 (2004).

[142] R. W. Simmonds, K. M. Lang, D. A. Hite, S. Nam, D. P. Pappas, and J. M. Martinis. Decoherence in Josephson Phase Qubits from Junction Resonators, *Phys. Rev. Lett.* **93**, 077003 (2004).

[143] J. M. Martinis, S. Nam, J. Aumentado, K. M. Lang, and C. Urbina. Decoherence of a superconducting qubit due to bias noise, *Phys. Rev. B* **67**, 094510 (2003).

[144] I. Chiorescu, Y. Nakamura, C. J. P. M. Harmans, and J. E. Mooij. Coherent Quantum Dynamics of a Superconducting Flux Qubit, *Science* **299**, 1869–1871 (2003).

[145] H. S. J. van der Zant, F. C. Fritschy, T. P. Orlando, and J. E. Mooij. Dynamics of vortices in underdamped Josephson-junction arrays, *Phys. Rev. Lett.* **66**, 2531–2534 (1991).

[146] D. B. Tuckerman and J. H. Magerlein. Resonances in symmetric Josephson interferometers, *Jou* **37**, 241–243 (1980).

[147] J. Magerlein. Specific capacitance of Josephson tunnel junctions, *Magnetics, IEEE Transactions on* **17**, 286 –289 (1981).

[148] M. Maezawa, M. Aoyagi, H. Nakagawa, I. Kurosawa, and S. Takada. Specific capacitance of Nb/AlOx/Nb Josephson junctions with critical current densities in the range of 0.1?18 kA/cm2,**66**, 2134–2136 (1995).

[149] W. H. Parker, B. N. Taylor, and D. N. Langenberg. Measurement of $\frac{2e}{h}$ Using the ac Josephson Effect and its Implications for Quantum Electrodynamics, *Phys. Rev. Lett.* **18**, 287–291 (1967).

[150] T. Niemczyk. „From strong to ultrastrong coupling in circuit QED architectures“. PhD thesis. TU München, 2011.

[151] G. Wild. „Macroscopic quantum tunneling in Josephson junctions - a method to characterise a well-shielded low temperature setup“. MA thesis. TU München, 2004.

[152] H. Tanaka, S. Saito, H. Nakano, K. Semba, M. Ueda, and H. Takayanagi. Single-Shot Readout of Macroscopic Quantum Superposition State in a Superconducting Flux Qubit, *Science And Technology* **1**, 5 (2004).

[153] J. Koch, T. M. Yu, J. Gambetta, A. A. Houck, D. I. Schuster, J. Majer, A. Blais, M. H. Devoret, S. M. Girvin, and R. J. Schoelkopf. Charge-insensitive qubit design derived from the Cooper pair box, *Phys. Rev. A* **76**, 042319 (2007).

[154] D. J. Van Harlingen, T. L. Robertson, B. L. T. Plourde, P. A. Reichardt, T. A. Crane, and J. Clarke. Decoherence in Josephson-junction qubits due to critical-current fluctuations, *Phys. Rev. B* **70**, 064517 (2004).

[155] F Zwanenburg. „Superconducting electronics with phase biased SQUIDs“. MA thesis. TU Delft, 2003.

[156] Butcher. „Advances in persistent-current qubit research: Inductively coupled qubits and novel biasing methods“. MA thesis. TU Delft, 2002.

[157] F. Terman. Radio Engineers’ Handbook. Ed. by London. Mc Graw-Hill, 1950.

[158] D. Belitz. Theory for dirty superconductors. I. Strong-coupling equations, *Phys. Rev. B* **35**, 1636–1650 (1987).

[159] A. J. Annunziata, D. F. Santavicca, L. Frunzio, G. Catelani, M. J. Rooks, A. Frydman, and D. E. Prober. Tunable superconducting nanoinductors, *Nanotechnology* **21**, 445202 (2010).

[160] T. Kato, A. A. Golubov, and Y. Nakamura. Decoherence in a superconducting flux qubit with a π-junction, *Phys. Rev. B* **76**, 172502 (2007).

[161] P. Forn Diaz. „Superconducting qubits and quantum resonators“. PhD thesis. TU Delft, 2010.

[162] F. Deppe, M. Mariantoni, E. P. Menzel, S. Saito, K. Kakuyanagi, H. Tanaka, T. Meno, K. Semba, H. Takayanagi, and R. Gross. Phase coherent dynamics of a superconducting flux qubit with capacitive bias readout, *Phys. Rev. B* **76**, 214503 (2007).

[163] L. Eggenstein. „Optimierung und Charakterisierung von supraleitenden Quantenschaltkreisen auf Basis von Fluss Quantenbits“. MA thesis. TU München, 2009.

[164] M. Frasca. Rabi oscillations and macroscopic quantum superposition states, *Phys. Rev. A* **66**, 023810 (2002).

[165] S. Saito, M. Thorwart, H. Tanaka, M. Ueda, H. Nakano, K. Semba, and H. Takayanagi. Multiphoton Transitions in a Macroscopic Quantum Two-State System, *Phys. Rev. Lett.* **93**, 037001 (2004).

[166] P. J. Petersan and S. M. Anlage. Measurement of resonant frequency and quality factor of microwave resonators: Comparison of methods, *Journal of Applied Physics* **84**, 3392–3402 (1998).

[167] A. Broers, A. Hoole, and J. Ryan. Electron beam lithographyResolution limits, *Microelectronic Engineering* **32**, 131 –142 (1996).

[168] T. Brenninger. „A new thin thin film deposition system for the preparation of persistent current qubits“. MA thesis. TU München, 2007.

[169] These qubits are standard three Josephson-junction flux qubits fabricated and characterized at the the WMI. A detailed description of these qubits can be found in Ref. [147] and Ref. [148],

[170] S. Dandl. „Herstellung und Charakterisierung einer definierten elektromagnetischen Umgebung für supraleitende Fluss-Qubits“. MA thesis. TU München, 2006.

[171] E. Il'ichev, N. Oukhanski, A. Izmalkov, T. Wagner, M. Grajcar, H.-G. Meyer, A. Y. Smirnov, A. Maassen van den Brink, M. H. S. Amin, and A. M. Zagoskin. Continuous Monitoring of Rabi Oscillations in a Josephson Flux Qubit, *Phys. Rev. Lett.* **91**, 097906 (2003).

[172] I. Chiorescu, P. Bertet, K. Semba, Y. Nakamura, C. J. P. M. Harmans, and J. E. Mooij. Coherent dynamics of a flux qubit coupled to a harmonic oscillator, *NATURE* **431**, 159 (2004).

[173] J. Johansson, S. Saito, T. Meno, H. Nakano, M. Ueda, K. Semba, and H. Takayanagi. Vacuum Rabi Oscillations in a Macroscopic Superconducting Qubit *LC* Oscillator System, *Phys. Rev. Lett.* **96**, 127006 (2006).

[174] S. Gleyzes, S. Kuhr, C. Guerlin, J. Bernu, S. Deléglise, U. B. Hoff, M. Brune, J.-M. Raimond, and S. Haroche. Quantum jumps of light recording the birth and death of a photon in a cavity., *Nature* **446**, 297–300 (2006).

[175] B. R. Johnson, M. D. Reed, A. A. Houck, D. I. Schuster, L. S. Bishop, E. Ginossar, J. M. Gambetta, L. DiCarlo, L. Frunzio, S. M. Girvin, and R. J. Schoelkopf. *Quantum Non-demolition Detection of Single Microwave Photons in a Circuit*, 2010.

[176] H. Knoglinger. „Herstellung und Charakterisierung von supraleitenden Phasen-Qubits“. MA thesis. TU München, 2004.

[177] P. D. U. Hartmann. *Elektronenstrahllithographie, Versuch zum Fortgeschrittenenpraktikum*, Institut f¨ur Experimentalphysik, Universit¨at des Saarlandes.

[178] T. Flynn. Cryogenic engineering. Marcel Dekker, 2005.

Danksagung

Der Grundstein für die Anfertigung dieser Diplomarbeit wurde durch die Teilnahme eines Proseminars über *Makroskopische Quantenphänomene* unter Betreuung von Professor Gross gelegt, welches meinen ersten Berührungspunkt mit dem WMI darstellt. Motiviert durch die positiven Eindrücke während dieses Seminars und nach dem Hören mehrerer interessanter Vorlesungen von Herrn Professor Gross während des Hauptstudiums, habe ich mich um eine Diplomarbeit am WMI bemüht. Ich möchte Herrn Professor Gross herzlich dafür danken, dass er die Durchführung dieser Arbeit ermöglicht hat.

Der Wunsch München als Standort für mein Studium zu wählen, wurde maßgeblich durch meine Freundin **Linda** bestärkt, die mich seit über sechs Jahren begleitet und mich in jeder Situation während dieser Zeit unterstützt hat. Es ist sicherlich kaum abzuschätzen, wie stark dies zum Gelingen dieser Diplomarbeit beigetragen hat und wie die teilweise stressige Zeit während des Studiums ohne Lindas liebherzige Unterstützung auszuhalten gewesen wäre.
Es ist eine Sache sich für ein Studium in München zu entscheiden, es ist jedoch eine ganz andere, dieses Studium auch zu ermöglichen. An dieser Stelle möchte ich meiner **Familie**, insbesondere meinen **Eltern**, dafür danken, dass sie mir ein tolles Studium ermöglicht und mir währenddessen stets unter die Arme gegriffen haben.

Diese Arbeit wäre so sicherlich nicht entstanden, gäbe es da nicht den einen Menschen, der mir seit einem Jahr fast täglich mit Rat und Tat zur Seite gestanden hat.
Meinem betreuenden Doktoranden **Manuel** ist die schwierige Aufgabe gelungen, während der gesamten Diplomarbeit den schmalen Grat zwischen intensiver und fördernder Betreuung zu gehen, einem dabei aber auch den Freiraum einer stets fordernden Eigenständigkeit und Kreativität zu lassen. Die professionelle Sicherheit seiner Handlungen und der logische Schluss seiner Gedankengänge waren für einen zunächst unerfahrenen Diplomanden immer ein zuverlässiger Wegweiser. Auch wenn der Weg zum Ziel dieser Arbeit wie üblich so manchen Schlenker nahm, führte er letztendlich zum Ziel. Es war sicherlich eine durchweg positive Erfahrung mit Manuel zusammen arbeiten zu dürfen.

Des Weiteren möchte ich mich bei **Achim Marx** und **Frank Deppe** für die umfassende Betreuung dieser Arbeit, sowie die Aufnahme in die Qubit-Gruppe am WMI bedanken. Auch gilt mein Dank allen weiteren Mitgliedern der Qubit-Gruppe, die mir stets mit Rat und Tat zur Seite standen. An dieser Stelle ist mit Sicherheit **Thomasz** zu nennen, der nicht nur meinen bisherigen Aufenthalt am WMI stets mit seiner Kreativität bereichert, sondern auch das Gelingen dieser Arbeit durch unzählige Ratschläge und Tipps erleichtert hat. Düdelidüdelidüdeliduuu, Düdelidüdelidüdelidu.

Mein Arbeitsalltag am WMI, sowie die ein oder andere nächtliche Veranstaltung, wurden maßgeblich durch **Peter**, **Felix**, **Eva**, **Marta**, **Friedrich**, **Max** und **Matthias** erhellt. Glücklicherweise gibt es neben den genannten Personen noch eine ganze Reihe Anderer, die einem am WMI den Alltag bereichern.
Weiterhin geht mein Dank an **Thomas Brenninger**, die **Heliumversorgung**, die **Werkstatt** und an allen anderen Menschen, die den reibungslosen Ablauf am WMI ermöglichen.

Bei Ihnen und all jenen, die mich während der Entstehung dieser Arbeit, sowie in den letzten Jahren unterstützt haben, möchte ich mich ganz herzlich für eine tolle Zeit bedanken.

Erklärung

des Diplomanden

Name:

Vorname:

Mit der Abgabe der Diplomarbeit versichere ich, dass ich die Arbeit selbständig verfasst und keine anderen als die angegebenen Quellen und Hilfsmittel benutzt habe.

....

(Ort, Datum) (Unterschrift)